Title
van der Waals Corrected Density Functional Theory Calculations on Zeolitic Imidazolate Frameworks

Author
Ray, Keith G.

Publication Date
2013

Peer reviewed|Thesis/dissertation

van der Waals Corrected Density Functional Theory Calculations on Zeolitic Imidazolate Frameworks

by

Keith George Ray

A dissertation submitted in partial satisfaction of the

requirements for the degree of

Doctor of Philosophy

in

Physics

in the

Graduate Division

of the

University of California, Berkeley

Committee in charge:

Professor Mark Asta, Co-Chair

Professor Steven Louie, Co-Chair

Professor Alex Zettl

Professor Omar Yaghi

Spring 2013

van der Waals Corrected Density Functional Theory Calculations on Zeolitic Imidazolate Frameworks

Abstract

van der Waals Corrected Density Functional Theory Calculations on Zeolitic Imidazolate Frameworks

by

Keith George Ray

Doctor of Philosophy in Physics

University of California, Berkeley

Professor Mark Asta, Co-Chair

Professor Steven Louie, Co-Chair

The van der Waals force is ubiquitous in nature, however, first principles calculations of this interaction for large systems, i.e., around 1000 atoms, have been performed only recently. In the following are presented results on the application of the van der Waals density functional (vdW-DF) to gas adsorption and transport in zeolitic imidazolate frameworks (ZIFs).

Carbon dioxide and methane binding energies and positions are calculated with the vdW-DF in three distinct binding sites in a series of five **rho** topology ZIFs. The isostructural set of ZIFs was selected in order to isolate the effect of framework functionalization. Gas molecules are found to bind in locations with high coordination to framework atoms at distances of around 3 Å. Contributions to the binding energy from induced polarization and dispersion are quantified in order to elucidate the origins of strong CO_2 adsorption and selectivity over CH_4. The dispersion energy is found to dominate the interactions, however, CO_2 adsorption is also enhanced by electrostatic interactions with asymmetrically functionalized linkers. Steric constraints for methane molecules, that do not impede carbon dioxide binding, further contribute to selectivity.

Binding energy landscapes for CO_2 and CH_4 are calculated using classical force fields for the same set of **rho** ZIFs and several other ZIFs that differ in functionalization and topology. Quantities extracted from these landscapes are used to explain the effect of framework topology on gas adsorption at low and high pressure as well as how the positions of adsorbed gas molecules evolve as a function of pressure. Materials with large surface areas have greater gas uptake at high pressure, while smaller pores, which are associated with stronger binding, adsorb more gas at low pressure.

Finally, the effect of framework flexibility on CO_2 transport through the double 8-ring channel of ZIF-97 is investigated with computationally intensive climbing-nudged elastic band calculations utilizing two versions of the vdW-DF. The results are largely consistent between the two versions and show a small decrease (12-33 meV) in the transport barrier with flexibility.

In addition, several versions of the vdW-DF are applied to the Kr dimer, graphite, and H_2, Al, and Li on graphene. For these systems experimental binding energies and

separations are available, such that they provide useful benchmarks for the accuracy of the vdW-DF type methods. The vdW-DF2 and vdW-optB88 methods are found to both produce accurate results for dispersion dominated binding. Analyses of mixed ionic-dispersion binding highlight the importance of further study of these functionals at short-range.

To my teachers.

Contents

List of Figures

List of Tables

Acknowledgments

First and foremost, I would like to thank my advisor, Mark Asta, for guiding the research that would become my dissertation. Mark has been a constant source of inspiration, insight, and good advice: resources clearly forged from experience and alloyed with patience.

I would also like to thank my co-advisor, Steven G. Louie, for looking after me during my time as a theory graduate student in condensed matter physics. Before that, I took the graduate solid state physics courses, 240A and 240B, from him and benefited from his clear and detailed explanations.

I would like to thank my former advisor, Alex Zettl, for all that he taught me about experiment. His critiques of papers presented at group meeting and the intuition he shared during sub-group meetings provided much to learn from. He taught the first physics course I took as an undergraduate at Berkeley and I have been interested in solid state physics ever since.

Ivo Souza taught the undergraduate solid state physics courses, 141A and 141B, which I took while in college. I am grateful to him for illuminating discussions on solid state physics that continued into graduate school.

I would like to thank Omar M. Yaghi for collaboration on the ZIF work and Joel E. Moore for discussions on topology in class and office hours. I'd also like to thank them both for serving on my qualifying exam. I am also grateful to Vincent Bouchiat for demonstrating how fun a helium-3 refrigerator can be and to Willi Michaelson for showing me how to do arc-synthesis of nanotubes.

I want to give thanks to Anne Takizawa, who has always been helpful and knowledgeable with regard to all the official hurdles of graduate school (as well as some of the unofficial ones).

I am incredibly grateful for all the support, good times, and collaboration provided by my colleagues and fellow graduate students at Berkeley. Gavi Begtrup made for a rocking mentor upon entering graduate school and it was an honor to work alongside him, as well as Will Gannett, Tom Yuzvinsky, Brian Kessler, Henry Garcia, and all the others in Zettl group. I would like to thank Emmanouil Kioupakis and Sangkook Choi for advice about ab-initio condensed matter theory. Colin Ophus, Nicole Adelstein, and David Olmsted have been valued colleagues to compare notes with, whether on DFT, data analysis, LAMMPS, or otherwise. William Morris at UCLA was great to work with as an experimental collaborator on the ZIF project. And thanks to my colleague Hong Ding for giving me another vdW system to think about. I would also like to thank Cinna Wu, Romain Barnard, Will Regan, Anna Zaniewski, Kris Erickson, Kwanpyo Kim, Michael Rousseas, Kenneth Jensen, Steven Kusalo, and Elizabeth Mattiuzzi for their friendship and support.

Finally, I would like to thank my sister, for her encouragement, and my mom and dad, for always looking up the answer to any question I ever had growing up (often from *The Flying Circus of Physics*[216]).

This work was supported as part of the Molecularly Engineered Energy Materials (MEEM), an Energy Frontier Research Center funded by the U.S. Department of Energy, Office of Science, Office of Basic Energy Sciences under Award Number DE-SC0001342. This work made use of resources of the National Energy Research Scientific Computing

Center, supported by the Office of Science of the U. S. Department of Energy under Contract No. DE-AC02-05CH11231.

Part I

Introduction and Background

Chapter 1

Introduction

Complex materials can now be fabricated with unprecedented control over the composition and structure, producing interesting and technologically useful physical properties. Carbon nanomaterials with different dimensionalities, such as buckyballs[71, 109, 40, 42], nanotubes[88, 48, 87, 153], and graphene[161, 53], for instance, continue to be the subject of intense study. In these materials have been found strong exciton binding energies[218, 148, 171, 202], exceptionally high Young's moduli[211], relativistic Dirac quasiparticles[161], high thermal stabilities[19], unique field emission properties[39], and an anomalous quantum hall effect[233, 161], among other phenomena, demonstrating the variety that can come from a single atomic building block.

The combinatorics arising from a more liberal use of the periodic table are staggering. Zeolitic imidazolate frameworks (ZIFs)[84, 167] are nanoporous materials that can be engineered in terms of both their network topology and composition by the use of different chemical reactants and growth conditions[13]. This control over structure and chemical functionality in a nanoporous material provides the opportunity to study interesting interactions with gas molecules that may be optimized for adsorption and separation applications. Such applications include hydrogen storage and the separation of CO_2 from CH_4 for the purification of biogas and upgrading of natural gas.

ZIFs are a metal organic framework (MOF)[131] subset in which transition metal atoms, such as zinc or cobalt, are tetrahedrally coordinated by organic imidazolate linkers and connected in such a way that the metal-imidazole-metal angle is similar to the Si-O-Si bond angle in a zeolite[84, 167]. Thus ZIFs form in network topologies which are homeomorphic to those found in zeolites. Figure 1.1 explicitly illustrates the connection between the topology of the zeolite **rho** material[43] and the **rho** topology of ZIF-93. The imidazolate linkers, which bridge the transition metal atoms, are five-membered heterocycles made of 3 carbon atoms and 2 nitrogen atoms. The members of the ring, which also correspond to sites available to bond other atoms and molecules, can be numerically labeled 1–5, as in Figure 1.1. Sites 1 and 3 are occupied by nitrogen atoms, which are bonded to transition metal atoms in ZIFs. These bridging bonds form the backbone of the material. Sites 2, 4, and 5 can be decorated with chemical functional groups such as amines, methyl groups, and nitriles.

The interior structure of these materials may be considered as a network of pores

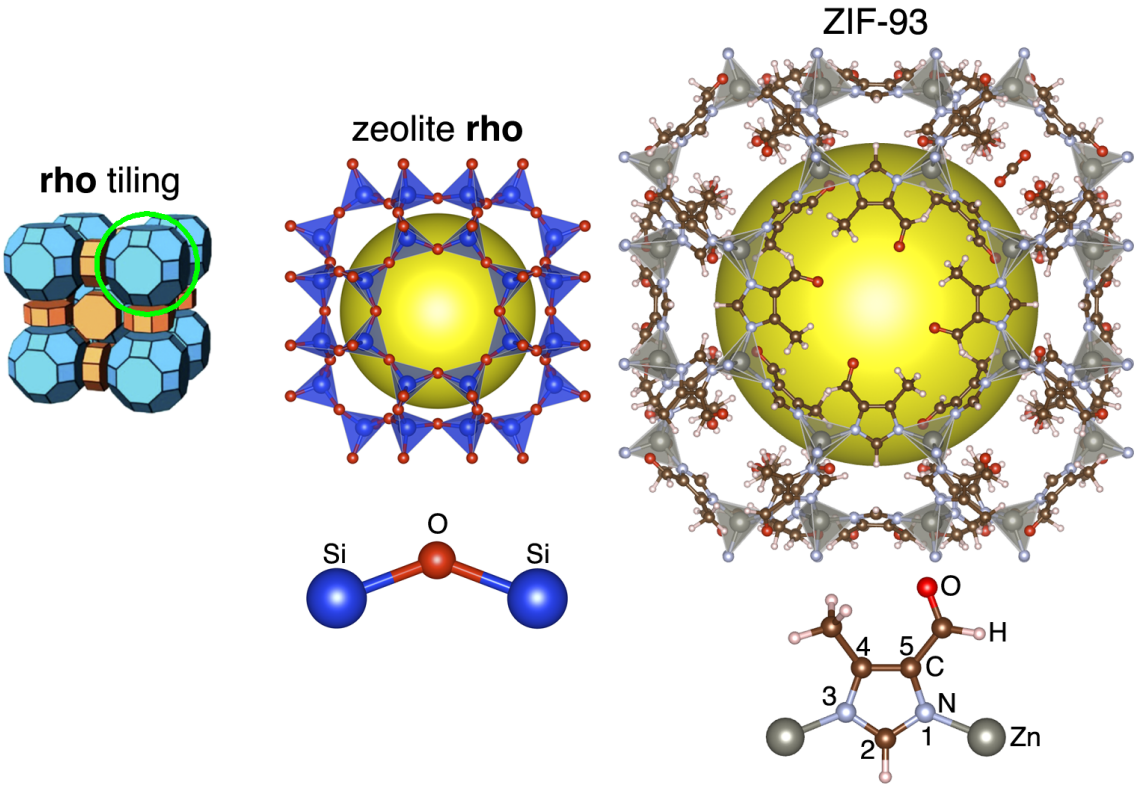

Figure 1.1: The tiling of the zeolite **rho** topology and two instances of this topology, zeolite **rho** and ZIF-93, are shown. The cage (polyhedron) highlighted in green in the **rho** tiling corresponds to the groups of atoms given for zeolite **rho** and ZIF-93. The vertices of this cage are given by Si in zeolite **rho** and Zn in ZIF-93. The yellow spheres represent empty space in the frameworks. The Si-O-Si bond angle and the similar Zn-imidazole-Zn bond angle are depicted for comparison.

connected by channels. Pores are the empty regions represented by yellow spheres in Figure 1.1. In ZIF-93, channels run through the rings of eight zinc atoms and rings of six zinc atoms, which correspond to the octagonal and hexagonal faces in the **rho** tiling, all shown in Figure 1.1. ZIFs contain all the topological variety of zeolites (as well as forming some unique topologies not observed in zeolites[13, 217]), with larger pores and channels due to the organic linkers, which increase the metal to metal distance compared to the equivalent vertex to vertex distance in zeolites. Furthermore, ZIFs add another dimension of variation coming from the possible functionalizations of the linker.

ZIFs can possess surface areas as high as 1947 m^2/g[167]. They are also thermally stable, with some structures being able to withstand temperatures as high as 550° C, as well as being chemically robust[167]. For example, ZIF-8 retains crystallinity after being subjected to the reflux of benzene, methanol, and water at temperatures between 65° and 100° C for up to 7 days, and the reflux of aqueous NaOH for up to a day[167]. Due to the zeolite structural variety and the catalog of possible imidazole functionalizations, there

is a large number of possible ZIF materials[173]. These characteristics make ZIFs ideal candidate materials to be engineered on the molecular level for gas adsorption and separation applications as well as fundamental studies of gas-framework interactions. Example gas adsorption applications include the storage of hydrogen to be burned or used in a fuel cell for energy[222] and CO_2 capture technologies to reduce the emission of greenhouse gases[13]. ZIFs may also be ideal for a host of gas separations, such as: H_2 from CO_2, for pre-combustion coal gasification, CO_2 from N_2, for flue gas carbon capture from the post-combustion of coal, CO_2 from CH_4, for natural gas upgrading, and O_2 from N_2, for the oxy-combustion of coal[208].

Different ZIF topologies have been synthesized with the same chemical composition [155] and ZIFs with the same topology can be synthesized with different chemical functional groups attached to the imidazole ring[156, 5]. This freedom in synthesis can allow for somewhat independent control over chemical functionalization from structural properties like surface area, channel morphology, and pore size, shape, and connectivity. Structural characteristics can enhance gas membrane selectivity (the capacity to separate gases by the selective transport of gas through the material), gas adsorption selectivity, gas transport, and overall uptake through changing steric constraints and varying binding site geometries[208, 17, 70, 155]. Imidazolate linker functionalization can also influence structural properties, for example, functional groups can protrude into pores and channels (the resultant constriction in a channel is known as a gate[2, 62]) or block entrance to specific binding sites. However, at least of equal significance, ZIF functionalizations affect ZIF-gas electrostatic, hydrogen bonding, and van der Waals interactions through the type and size of the chemical group, as well as the use of multiple groups to break symmetries in the ZIF crystal and its internal electrostatic potential[185, 156, 129, 172, 10].

Monte Carlo or molecular dynamics simulations[101] based on classical force fields are often used to model the adsorption and transport of gas molecules in ZIFs. Adsorption isotherms and diffusion coefficients can be calculated for several gases individually, or in mixtures, in systems that contain thousands of atoms. The force fields can include Coulomb and van der Waals interactions, and polarization, depending on the level of detail relevant to the problem and the desired complexity of the simulation. However, there are inaccuracies associated with using these potentials. A functional form for a particular potential may not be exact for all distances. For example, charge overlap would modify a pairwise atomic Coulomb interaction model for atoms in close proximity. Also, the parameterization of the potentials for a pair of atoms may not be valid for a particular system because the electronic structure of an atom changes based on its local environment. For these reasons and others, first principles quantum mechanical calculations are necessary to obtain accurate interaction energies between the ZIF and gas molecule, without parameterization and including all relevant contributions.

Density functional theory (DFT)[78, 105] is a first principles quantum mechanical method, useful for its combination of accuracy for many materials properties and ability to handle systems with up to around a thousand atoms. It is based on a construction of the electron Hamiltonian as an operator on the electron density instead of the full many-body electron wavefunction. While this substitution is formally exact with the correct density functional, only approximate functionals are known. The primary approximation is that

the energy associated with electron correlation, divided into portions called correlation and exchange (the latter simply being the correlation associated with satisfying the symmetry of fermion exchange), is often made a function of the local electron density and its gradient only. This is sufficient for determining many quantities for systems that are covalently, metallically, and ionically bound. However, for systems in which the so-called van der Waals interaction is important, this approximation will fail.

The van der Waals interaction, specifically London dispersion, is an attractive force arising from non-local electron correlation. In a simple case, it can be considered as an instantaneous dipole-induced dipole interaction. As such, it will be neglected in any local or semilocal correlation energy. However, recent theoretical developments[195, 194, 46, 207, 188] on the incorporation of a non-local correlation energy into density functional theory have produced a van der Waals density functional (vdW-DF) capable of accurately including these interactions for a variety of materials and geometries. Thus the usefulness of DFT has been extended to a new class of materials, from sparse matter and layered materials to liquids, gases, and their interfaces with each other and solids.

In the following we apply the vdW-DF to study gas binding and transport in ZIFs. Chapter 2 is dedicated mostly to our primary theoretical tool, DFT, and the approximations and implementations that make it practical. These include common forms of the exchange-correlation functional and generalized pseudopotential schemes. Chapter 3 introduces the London dispersion force, several methods of its calculation, and the vdW-DF. We present a derivation of the vdW-DF and discuss popular variations.

Section II begins with chapter 4 on vdW-DF calculations on relatively simple dispersion bound systems, such as noble gas dimers and graphite, as a prelude to the larger ZIF calculations in later chapters. Different vdW-DF variants are compared to each other, as well as to results from the literature. Chapter 5 is an in depth vdW-DF study of CO_2 binding in a set of ZIFs which share the same topology and differ only in the functionalization of the imidazole ring. This unique set of materials allows us to isolate the effect of these chemical groups on CO_2 adsorption. Gas binding energy landscapes, calculated with classical force fields, are used in Chapter 6 to elucidate the effect, at different pressures, of ZIF topology on CO_2 uptake and ZIF functionalization on CH_4 uptake. Chapter 7 expands the results in Chapter 5 using the vdW-DF to explain how CO_2/CH_4 adsorption selectivity is affected by ZIF functionalization through a variety of mechanisms. Steric constraints, electrostatic interactions, dispersion energy, and induced polarizations are considered and quantified. Finally, Chapter 8 uses the vdW-DF method in a climbing nudged elastic band (climbing-NEB) calculation to examine the role of framework flexibility in CO_2 inter-pore transport through constrained channels.

Section III ends the dissertation with a summary of results, conclusions, and possible future work. The vdW-DF2 and vdW-optB88 methods have been used to carefully examine non-bonded interactions between gas molecules and ZIFs. CO_2 adsorption strength and selectivity over CH_4 was determined to originate from both geometric and electrostatic effects, which depend on linker functionalization. ZIF topology affects low and high pressure gas uptake differently due to the competition between surface area and strong dispersion binding. And finally, framework flexibility can affect the transport of CO_2 through the channels between pores. General trends found in this body of research are presented. Open

questions and possible future lines of research are discussed.

Chapter 2

Theoretical Framework

2.1 Introduction to the Many-Body Schrödinger Equation

A central problem in the theory of condensed matter physics is the calculation of the physical properties of a solid or liquid system knowing only the atomic positions and species[236, 146, 147]. Such a system in the steady state is described by the many-body Schrödinger equation

$$\hat{H}\Psi(\mathbf{r}_1, ..., \mathbf{r}_N, \mathbf{R}_1, ..., \mathbf{R}_S) = E\Psi(\mathbf{r}_1, ..., \mathbf{r}_N, \mathbf{R}_1, ..., \mathbf{R}_S), \tag{2.1}$$

where the Hamiltonian is given by

$$\begin{aligned}\hat{H} = \sum_{i=1}^{N} \frac{-\hbar^2 \nabla_i^2}{2m_e} + \sum_{I=1}^{S} \frac{-\hbar^2 \nabla_I^2}{2M_I} + \sum_{i=1}^{N} \sum_{j>i}^{N} \frac{e^2}{|\mathbf{r}_i - \mathbf{r}_j|} + \sum_{I=1}^{S} \sum_{J>I}^{S} \frac{e^2 Z_I Z_J}{|\mathbf{R}_I - \mathbf{R}_J|} \\ + \sum_{i=1}^{N} \sum_{J=1}^{S} \frac{e^2 Z_J}{|\mathbf{r}_i - \mathbf{R}_J|} + V(\mathbf{r}_1, ..., \mathbf{r}_N, \mathbf{R}_1, ..., \mathbf{R}_S).\end{aligned} \tag{2.2}$$

In the above, the first and second terms are the kinetic energies of the electrons and nuclei; the third, fourth, and fifth terms are the Coulomb interaction energies between the electrons only, between the nuclei only, and between the electrons and nuclei; and finally the sixth term is energy due to an external potential. This form already makes many assumptions: we are not interested in anything but the electromagnetic force, the system is non-relativistic, the nuclei have no internal structure, quantum field fluctuations are unimportant, and spin orbit interactions are not explicitly included. However, this will do for our purposes and more terms can be added later if necessary.

Equations (2.1,2.2) are unfortunately far too complicated to solve for all but the smallest systems, let alone macroscopic ones where the wavefunction has $3(N + S) \approx 10^{23}$ variables, where N is the number of electrons and S is the number of nuclei. Further approximations must be made. The first will be the Born-Oppenheimer or adiabatic approximation which makes use of the large discrepancy in the masses of the electrons and that of the nuclei, which differ by a factor of around 10^4. This allows the electronic and nuclear degrees of freedom to be decoupled and as a result we can solve for the wave function

of the electrons alone with a Hamiltonian parameterized by the nuclear positions,

$$\hat{H}_{B-O}(\mathbf{R}_1, ..., \mathbf{R}_S) = \sum_{i=1}^{N} \frac{-\hbar^2 \nabla_i^2}{2m_e} + \sum_{i=1}^{N} \sum_{j>i}^{N} \frac{e^2}{|\mathbf{r}_i - \mathbf{r}_j|} + \sum_{i=1}^{N} \sum_{J=1}^{S} \frac{e^2 Z_J}{|\mathbf{r}_i - \mathbf{R}_J|} + V(\mathbf{r}_1, ..., \mathbf{r}_N). \quad (2.3)$$

Thus, the ground state energy of the electronic system, $E_0(\mathbf{R}_1, ..., \mathbf{R}_S)$, corresponds to the solution of the equation

$$\hat{H}_{B-O}(\mathbf{R}_1, ..., \mathbf{R}_S)\Psi(\mathbf{r}_1, ..., \mathbf{r}_N) = E_0(\mathbf{R}_1, ..., \mathbf{R}_S)\Psi(\mathbf{r}_1, ..., \mathbf{r}_N). \quad (2.4)$$

As the direct consequence of the Born-Oppenheimer approximation the electronic system is assumed to be in its ground state for each instantaneous position of the nuclei. This approximation has a very wide domain of applicability, but can break down at very high temperatures or with very light nuclei, such as the proton in a hydrogen bond.

One of the first attempts at solving the many-body Schrödinger equation, the Hartree-Fock method, involved simplifying the many-body wavefunction by using a Slater determinant of single particle orbitals, i.e., the simplest antisymmetric sum of products of single particle orbitals[49]. This scheme, however, does not include any electron correlation besides that required by exchange antisymmetry. There are several "post-Hartree-Fock" methods that include correlation in various ways, such as coupled cluster[37, 38, 120, 36, 165, 16, 181] and Møller-Plesset perturbation theory[154]; however, currently the number of operations needed with these techniques scales much too quickly with the number of electrons to be applicable to large systems.

2.2 Density Functional Theory

In 1964, Hohenberg and Kohn showed that the external potential, $v(\mathbf{r})$, can be expressed as a unique functional of the ground state electron density, $n(\mathbf{r})$[78]. Here, and in the rest of this section, the nuclear potential is considered part of the external potential. The external potential defines the system Hamiltonian, H_{B-O} above, so the wavefunction itself and related quantities, such as kinetic energy and the electron-electron potential energy, are functionals of the density. From that and the variational principle, one can define (Note: in this section we use Hartree atomic units, while the rest of the dissertation utilizes mostly CGS)

$$E[n] = \min_{\Psi} \langle \Psi | H[n] | \Psi \rangle = \min_{n' \to n} \left[\int d\mathbf{r} v[n](\mathbf{r}) n'(\mathbf{r}) + F[n'] \right] \quad (2.5)$$

where on the left we have energy as a functional of the ground state electron density, in the middle we have the ground state energy as the minimum over the possible many-body wavefunctions and the Hamiltonian is a functional of the ground state electron density, and on the right we have split the energy functional into a system dependent term with $v[n]$ being the external potential creating the ground state density, n, and a system independent term, $F[n']$, allowing the energy to be realized as a minimum over electron densities, $n'(\mathbf{r})$, such that

$$\int d\mathbf{r} n'(\mathbf{r}) = N, \quad (2.6)$$

where N is the number of electrons in the system. Also,

$$F[n] = E[n] - \int d\mathbf{r} v[n](\mathbf{r}) n(\mathbf{r}) \tag{2.7}$$

where we note the use of $v[n]$, the external potential as a functional of the density. Technically, it was only shown by Kohn and Hohenberg that $E[n]$, and therefore $F[n]$, was defined on the space of ground state densities. However, it was proved by Chayes, Chayes, and Ruskai that in quantum lattice models every strictly positive, properly normalized, and Pauli principle consistent n, is a ground state density for some external potential[32].

Conceptually, this theorem simplified the problem tremendously since the electron density is a function of 3 variables instead of the $3(N+S)$ variables in the full many-body wavefunction. Practically, the true form of the functional is unknown and it has been shown that the computational complexity of solving it exactly is still prohibitive[198]. However, this scheme has allowed for the use of approximate functionals that have offered excellent accuracy for many properties, such as lattice constants, elastic constants, magnetic structure, phase transitions, and others, combined with the computational efficiency necessary to allow application to systems of over one thousand atoms[63].

In 1965 Kohn and Sham showed that the variational problem of solving for the electron density that minimizes the energy functional in equation 2.5 could be mapped onto a system of non-interacting orbitals and solved iteratively[105]. First, the energy functional in brackets on the right hand side of 2.5 can be further partitioned,

$$\begin{aligned} E[v, n(\mathbf{r})] &= \int d\mathbf{r} v(\mathbf{r}) n(\mathbf{r}) + F[n(\mathbf{r})] \\ = \int d\mathbf{r} v(\mathbf{r}) n(\mathbf{r}) &+ \int d\mathbf{r} d\mathbf{r}' \frac{n(\mathbf{r}) n(\mathbf{r}')}{2|\mathbf{r} - \mathbf{r}'|} + T[n(\mathbf{r})] + E_{xc}[n(\mathbf{r})], \end{aligned} \tag{2.8}$$

where the electron-electron Coulomb energy, the kinetic energy functional ($T[n(\mathbf{r})]$), and the exchange-correlation functional have been introduced. E is now a functional of v because we will solve for the ground state density of a particular external potential. Finding the ground state electron density for the above equation is equivalent to solving the one particle Schrödinger equations[105],

$$\left[-\frac{1}{2}\nabla^2 + v(\mathbf{r}) + \int d\mathbf{r}' \frac{n(\mathbf{r}')}{|\mathbf{r} - \mathbf{r}'|} + \mu_{xc}(\mathbf{r}) \right] \phi_i(\mathbf{r}) = \epsilon_i \phi_i(\mathbf{r}), \tag{2.9}$$

where

$$\mu_{xc}(\mathbf{r}) = \frac{\delta E_{xc}[n]}{\delta n(\mathbf{r})} \tag{2.10}$$

and

$$n(\mathbf{r}) = \sum_{i}^{occupied} |\phi_i(\mathbf{r})|^2. \tag{2.11}$$

Equation 2.11 says that the sum of the probability densities of the orbitals of the auxiliary system up to the highest energy occupied orbital corresponds to the electron density, $n(\mathbf{r})$. This system of equations are the Kohn-Sham equations, which may be solved self-consistently to find the ground state density.

2.3 The Exchange-Correlation Energy Functional

The exact form of $E_{xc}[n]$, a functional of the electron density over all space defined by Equation 2.8, is unknown. A reasonable first approximation is to express this energy functional as a local potential

$$E_{xc} = \int d\mathbf{r} n(\mathbf{r}) \epsilon_{xc}(n_\uparrow(\mathbf{r}), n_\downarrow(\mathbf{r})) \tag{2.12}$$

where $\epsilon_{xc}(n_\uparrow(\mathbf{r}), n_\downarrow(\mathbf{r}))$ now takes the value of the exchange and correlation energy per particle of a homogeneous electron gas at the density $(n_\uparrow(\mathbf{r}), n_\downarrow(\mathbf{r}))$ with spin up and spin down densities represented. This approximation, known as the local spin density approximation (LSDA), is often used and one can reasonably expect it to produce good results when the system in question is close to the homogeneous electron gas. Hence solids are in general better represented than molecules or atoms. However, even in inhomogeneous cases, the method often still produces accurate results, aided by the fact that the exchange-correlation hole satisfies the related sum rule, creating a cancellation of errors. In more detail, due to the effects of exchange and electron correlation, an electron at a particular position, $\mathbf{r}$, affects the density of electrons around it, at positions $\mathbf{r}'$. This can be given as a modification to the joint probability function,

$$P(\mathbf{r}, \mathbf{r}') = n(\mathbf{r}) n(\mathbf{r}') + n(\mathbf{r}) n_{xc}(\mathbf{r}, \mathbf{r}'). \tag{2.13}$$

where $n_{xc}(\mathbf{r}, \mathbf{r}')$ is the exchange-correlation hole density, surrounding each electron at position $\mathbf{r}$. The sum rule

$$\int d\mathbf{r}' n_{xc}(\mathbf{r}, \mathbf{r}') = -1 \tag{2.14}$$

is obeyed because the integral over the exchange hole is -1 and the correlation hole integrates to zero.

An improvement on the LSDA is the generalized-gradient approximation (GGA) where $\epsilon_{xc}(n_\uparrow(\mathbf{r}), n_\downarrow(\mathbf{r}), |\nabla n_\uparrow(\mathbf{r})|, |\nabla n_\downarrow(\mathbf{r})|)$ is now a function of the density and the magnitude of its gradient[169]. The exchange-correlation energy is now best expressed as

$$E_{xc} = \int d\mathbf{r} n(\mathbf{r}) \epsilon_x(n(\mathbf{r})) f_{xc}(n_\uparrow(\mathbf{r}), n_\downarrow(\mathbf{r}), |\nabla n_\uparrow(\mathbf{r})|, |\nabla n_\downarrow(\mathbf{r})|) \tag{2.15}$$

where $\epsilon_x(n(\mathbf{r}))$ is the exchange energy per particle of the homogeneous gas and f_{xc}, the enhancement factor, is dimensionless[169]. There are different forms used for f_{xc} in the literature and they are often carefully constructed[170, 169] since a naive expansion of the exchange correlation energy in the gradient breaks sum rules and does not improve the LDA systematically[76]. Including a gradient dependence can lead to more accurate atomization energies, total energies, and reaction barriers than the LDA, which in turn made DFT more appealing to the chemistry community[169]. In addition, properties such as the lattice constants and bulk moduli of solids are improved from already accurate LDA predictions[169].

It will be useful in later sections to know about a few of the different exchange energy functionals currently available. When working with various GGAs, the reduced

gradient

$$s = \frac{|\nabla n|}{(2k_F)n}, \tag{2.16}$$

is often used, where k_F is the fermi wave vector. There are many formulations of the exchange energy enhancement factor, $f_x(n, s)$. This quantity is the exchange only and spinless version of f_{xc}, defined above. For example, the Becke 88 exchange functional[18] (B88) is given by

$$f_x = 1 + \frac{\mu s^2}{1 + \beta s \sinh^{-1}(cs)}, \tag{2.17}$$

where $c = 2^{4/3}(3\pi^2)^{1/3}$, $\mu \approx 0.2743$, and $\beta = 9\mu(6/\pi)^{1/3}/(2c)$, while the optB88 exchange functional[102] uses $\mu/\beta = 1.2$ and $\mu = 0.22$, the Perdew Burke Ernzerhof exchange functional[170] (PBE) is given by

$$f_x = 1 + \kappa - \frac{\kappa}{1 + \mu s^2/\kappa}, \tag{2.18}$$

where $\mu = \beta(\pi^2/3)$, $\beta = 0.066725$, and $\kappa = 0.804$, while the revPBE exchange functional[232] uses $\kappa = 1.245$, and finally the Perdew Wang 86 functional[168] (PW86) is given by

$$f_x = (1 + 1.296s^2 + 14s^4 + 0.2s^6)^{1/15}. \tag{2.19}$$

The enhancement factors for these five exchange functionals are plotted in Fig. 2.1. We can relate the shape of these factors with how repulsive each functional will be. Since the exchange energy will be negative, a larger exchange enhancement factor means lower energy. Therefore larger exchange enhancement factors mean that regions of charge inhomogeneity are made to have relatively less energy when compared with smaller exchange enhancement factors. Charge inhomogeneity is more associated with separated atoms than bound atoms, thus larger exchange enhancement factors correspond to more repulsive exchange functionals. B88 will be more repulsive than optB88 and revPBE will be more repulsive than PBE or PW86.

2.4 Pseudopotentials and the Projector Augmented Wave Method

Not all electronic states in a general condensed matter system are created equal. Valence states contribute the most to bonding and are also most influenced by their environment. Core states do not contribute to binding, are relatively insensitive to their environment, and are tightly bound to a nucleus. Semi-core states are less tightly bound to the nuclei than core states and can polarize under the influence of local potentials, but do not greatly contribute to binding. This distinction allows for these states to be treated differently in practical DFT calculations. For example, in some all-electron methods (methods that explicitly solve for electronic states corresponding to all the electrons in the system), space is divided between regions near the nuclei and the region outside corresponding to valence electrons, then boundary conditions are enforced between the two. Other methods use different basis sets for core and valence states[104].

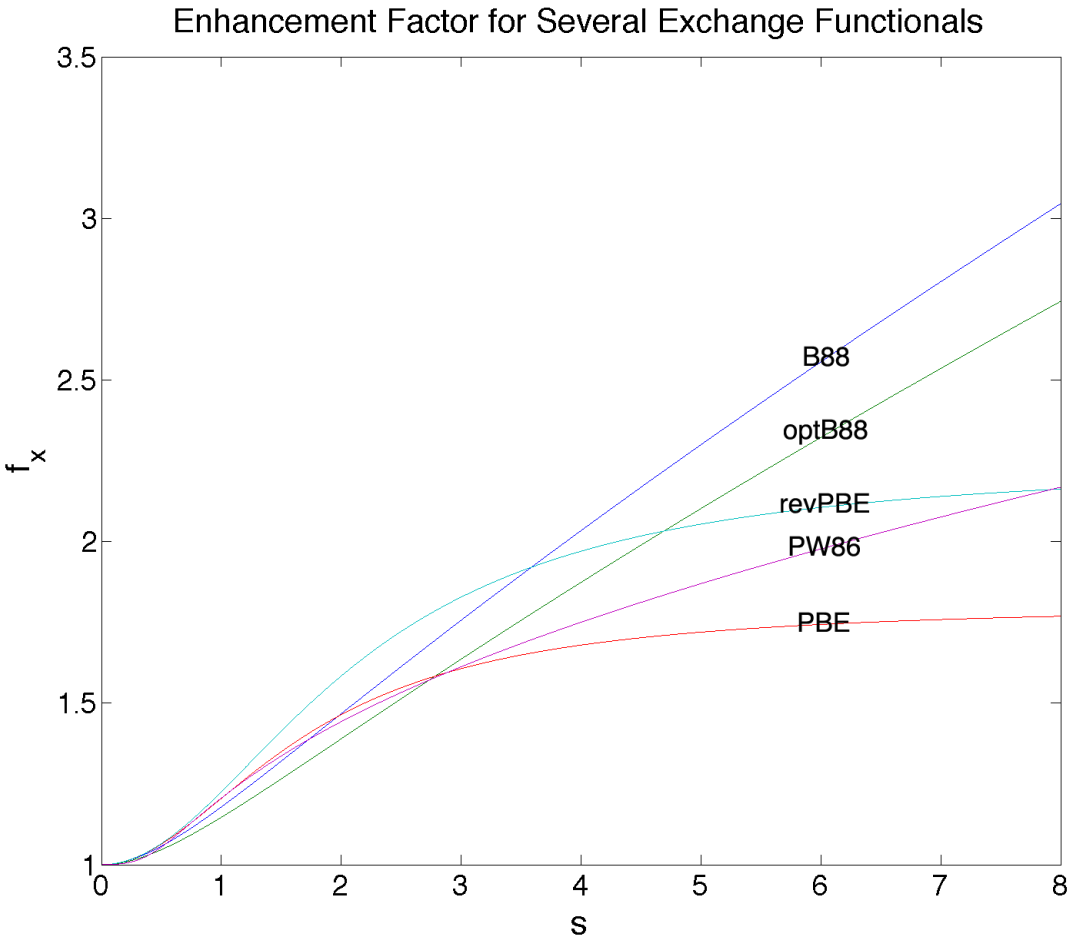

Figure 2.1: Enhancement factors are plotted for the B88, optB88, PBE, revPBE, and PW86 exchange functionals.

Since the valence electron states are the most important for binding and differ the most in solids and molecules from isolated atoms, it is logical to focus on those states and their interaction with the nuclei and core electrons. We will call the combination of a nucleus and its core electrons an ion. Then, the details of the core can be treated minimally. For example, the frozen core approximation fixes the core electron states and occupations, which introduces a usually small constant error in the energies[104]. The details of the valence electron states themselves in the core region are also usually relatively unimportant, which motivates the use of non-physical smoother functional forms in these regions. After such a replacement, the valence states are called pseudo-valence states. Using these functions is computationally advantageous, since outside the core regions, the valence states are already smooth and require a smaller number of basis functions, often plane waves, to represent. Inside the core regions large potential energy gradients produce rapidly varying, nodal, wavefunctions. Pseudopotentials replace the ionic potential with one that is smoother in the core region, but still reproduces the true valence charge density outside the core region.

There are many pseudopotential schemes. For instance, norm-conserving pseudopotentials [65] are accurate and transferable[147], requiring that the all-electron and pseudo valence states have the same eigenvalues and amplitude outside of the core region, while ultrasoft pseudopotentials[23, 213] relax certain requirements and are faster. Here we will focus on the projector augmented wave (PAW)[22] method as it is used throughout this work. First, we introduce pseudo wavefunctions $|\tilde{\psi}\rangle$ and all-electron wavefunctions $|\psi\rangle$ (Kohn-Sham orbitals in that formalism) related by

$$|\psi\rangle = T|\tilde{\psi}\rangle \tag{2.20}$$

where $T = \mathbf{1} + T^1$ is a linear transformation and T^1 is zero outside a sphere centered at the nucleus which we will call the augmentation region, R. Within that region

$$|\tilde{\psi}\rangle = \sum_m c_m |\tilde{\phi}_m\rangle \quad \text{and} \quad |\psi\rangle = \sum_m c_m |\phi_m\rangle \quad \text{within } R \tag{2.21}$$

where $|\tilde{\phi}_m\rangle$ and $|\phi_m\rangle$ are pseudo and all-electron partial waves, respectively, which coincide outside of R. Therefore, we have

$$|\psi\rangle = |\tilde{\psi}\rangle + \sum_m c_m(|\phi_m\rangle - |\tilde{\phi}_m\rangle). \tag{2.22}$$

T is linear so the c_m coefficients must be linear functionals of the $|\tilde{\psi}\rangle$, that is

$$c_m = \langle \tilde{p}_m | \tilde{\psi} \rangle \tag{2.23}$$

for *projector* functions, $\langle \tilde{p}_m|$ that satisfy $\langle \tilde{p}_m | \tilde{\phi}_n \rangle = \delta_{mn}$. Then equations 2.20 and 2.22 can be rewritten as

$$|\psi\rangle = T|\tilde{\psi}\rangle = \left[\mathbf{1} + \sum_m (|\phi_m\rangle - |\tilde{\phi}_m\rangle)\langle \tilde{p}_m|\right] |\tilde{\psi}\rangle. \tag{2.24}$$

The electronic wavefunctions are expressed in 3 parts: the smooth pseudo wavefunction $\tilde{\psi}$, which can be evaluated conveniently on a Cartesian grid, the pseudo partial waves $\tilde{\phi}_m$, and

the all-electron partial waves ϕ_m, which both are evaluated on radial grids. Precalculated atomic reference states can be used for the core electrons, which can be frozen, allowing the use of the PAW formalism on the valence states only, in the spirit of generalized pseudopotentials, as described above.

As a final note, pseudopotentials are generally created using the same exchange-correlation functional as will be used in the full calculation. This is not the case for the van der Waals density functional, described in the next chapter. Instead, this functional is employed with PBE PAW potentials, however, such an inconsistency has been shown to have a negligible effect on the binding energies and distances[64].

Chapter 3

The van der Waals Force and its Calculation

In general, the term *van der Waals forces* can refer to the aggregate of several intermolecular forces, interactions Johannes Diderik van der Waals included in his equation of state for gases and liquids[212]. These interactions can include Pauli exclusion repulsion, dipole-dipole, dipole-induced dipole, and instantaneous dipole-induced dipole. The last interaction, instantaneous dipole-induced dipole, is also known as the London dispersion force, or simply dispersion, and that will be our focus in what follows as well as what we refer to when we mention the van der Waals force. The London dispersion force will often dominate the binding of systems that consist of components that have at least one small dimension (e.g., small clusters, narrow fibers, and thin sheets) and are not otherwise bound by stronger forces. This includes weakly bonded molecules in nanoporous materials, layered materials such as graphite, the interaction of nanomaterials, proteins, molecular crystals, and other sparse matter. The dispersion energy is always present and can also significantly affect the structure (e.g., bond lengths, energies, and geometry) and structurally related properties (e.g., elastic constants and changed band structure due to changed orbital overlap) of many other systems that are primarily bound by other forces. CGS units are used in this chapter.

3.1 London Dispersion Force

The London dispersion force[143] is a quantum mechanical correlated electron effect. The simplest example, which we derive below, is the attractive interaction between separated hydrogen atoms given by correlated instantaneous dipoles, although in general this effect includes N-body terms and higher multipoles. We start with the Hamiltonian for the two hydrogen atoms, call them 1 and 2, neglecting any cross interaction

$$H_0 = -\frac{\hbar^2\nabla_1^2}{2m} - \frac{e^2}{r_1} - \frac{\hbar^2\nabla_2^2}{2m} - \frac{e^2}{r_2} \tag{3.1}$$

where r_i is the distance from nucleus i to electron i. The cross interaction is treated as a perturbation

$$H = H_0 + H' \tag{3.2}$$

$$H' = \frac{e^2}{r} + \frac{e^2}{|\mathbf{r} - \mathbf{r}_1 + \mathbf{r}_2|} - \frac{e^2}{|\mathbf{r} + \mathbf{r}_2|} - \frac{e^2}{|\mathbf{r} - \mathbf{r}_1|} \tag{3.3}$$

where $\mathbf{r}$ is the vector from nucleus 1 to nucleus 2 and $\mathbf{r}_i$ is the vector from nucleus i to electron i. Expanding H' in powers of $\mathbf{r}_i/\mathbf{r}$, which we assume to be small, results in

$$H' = \frac{e^2}{r^3}(x_1x_2 + y_1y_2 - 2z_1z_2) + O\left(\frac{1}{r^4}\right) \tag{3.4}$$

where x_i, y_i, and z_i are the components of $\mathbf{r}_i$ and the separation between the H nuclei is in the z direction. The first term represents the interaction between two dipoles in the far field limit and higher order terms represent the interaction of higher multipoles. The first order perturbation theory energy correction is zero,

$$E_0^{(1)} = \langle 0|H'|0\rangle = 0 \tag{3.5}$$

since the ground state is spherically symmetric. The second order leading term is given by

$$E_0^{(2)} = \sum_{k\neq 0} \frac{|\langle k^{(0)}|H'|0^{(0)}\rangle|^2}{E_0^{(0)} - E_k^{(0)}} = \frac{e^4}{r^6} \sum_{k\neq 0} \frac{|\langle k^{(0)}|x_1x_2 + y_1y_2 - 2z_1z_2|0^{(0)}\rangle|^2}{E_0^{(0)} - E_k^{(0)}}. \tag{3.6}$$

where $E_k^{(m)}$ is the mth order correction to the energy of the kth state and $|k^{(m)}\rangle$ is the mth order correction to the kth state. The 0th state is the ground state and the 0th correction is the unperturbed object. Here we see the r^{-6} dependence of the London dispersion interaction and that it is attractive since $E_k^{(0)} > E_0^{(0)}$. Although this functional form was derived for hydrogen atoms, it is the limit for the dispersion interaction between two finite general clusters of atoms or molecules at large separation and thus is often the form used for pair-wise approximations to the dispersion energy. These pair-wise approximations are given as C_6/r^6 where C_6 is a constant dependent on the interacting pair of atoms.

A first step in considering more complex systems would be the examination of the dispersion interaction between three atoms. The three-body term in perturbation theory to the third order, the Axilrod-Teller term[9], is given by

$$E_0^{(3)} = C\frac{3\cos\gamma_1\cos\gamma_2\cos\gamma_3 + 1}{r_{12}^3 r_{23}^3 r_{31}^3} \tag{3.7}$$

where C is a constant depending on the atomic polarizabilities and ionization energies, r_{ij} is the distance from atom i to atom j, and γ_i is the angle between $\mathbf{r}_{ij}$ and $\mathbf{r}_{ik}$. Depending on the arrangement of the three atoms this term can be repulsive or attractive. Many-body terms can have a significant effect. For instance, as the size of silicon clusters grows from 1 to 172 atoms, the effective C_6 coefficient (coefficient that would describe the vdW energy if only pairwise r^{-6} interactions are considered) decreases by 27% due to renormalization from the many-body interaction[210]. Furthermore, in systems where long-range charge

fluctuations can persist, such as metals and π-conjugated materials, the asymptotic scaling behavior of the interaction between two components can be qualitatively different than that given by a sum of pairwise potentials[47]. The energy between two 2D metal sheets goes like $-D^{-5/2}$ instead of $-D^{-4}$ as with insulators, where D is the separation, for instance[47]. Finally, it is worth noting that past $137a_0$, where a_0 is the Bohr radius, it was shown by Casimir and Polder that retardation effects, i.e., considering the effect of the finite speed of light using quantum electrodynamics, become important and the asymptotic pairwise interaction goes as $-D^7$[27].

3.2 Methods of Calculation for the van der Waals Force

A simple expression for the van der Waals force between two hydrogen atoms was presented in the previous section, however, for larger systems the exact solution quickly becomes impractical to calculate. DFT, as introduced in section 2.2, remains appealing because of its accuracy for many systems and computational efficiency. However, for systems in which the dispersion energy is important, the approximations for the exchange-correlation energy described in section 2.3 are inadequate. LDA and GGA exchange-correlation functionals are expressed as integrals of local and semi-local functions of the density alone and the density and its gradient, respectively. The van der Waals force is a non-local correlation effect and so it is neglected by these functionals.

Several methods have been developed to add back to DFT, under the LDA or GGA, the non-local correlation energy associated with the van der Waals force. In the Grimme approach[57, 58, 59], also referred to as DFT-D(versions 1, 2, and 3), the van der Waals energy is given by a sum of pairwise interatomic interaction terms over all atom pairs in the system. That form to the lowest order (r^{-6}, although in some versions r^{-8} and higher terms are also considered) is given by

$$E_6^{(2)} = s_6 \sum_{i<j} \frac{C_6^{ij}}{|\mathbf{r}_i - \mathbf{r}_j|^6} f_{d,6}(|\mathbf{r}_i - \mathbf{r}_j|). \tag{3.8}$$

where the superscript (2) denotes atom pairs, s_6 is an overall scaling factor, set to 1 in the most recent DFT-D3 version, the C_6^{ij} coefficients are determined in different ways with different levels of empiricism depending on the version of the method used, and $f_{d,6}$ is a damping function. The damping function is used to damp the singularity in r^{-6}; it approaches 1 at large $|\mathbf{r}_i - \mathbf{r}_j|$ and 0 at small $|\mathbf{r}_i - \mathbf{r}_j|$. In DFT-D1 the C_6^{ij} coefficients are given by averages of the empirical coefficient value over the hybridization states of each atom and in DFT-D2 they are given as a function of the atomic ionization energies and polarizabilities, calculated with the PBE0 hybrid functional[1]. In DFT-D3 they are calculated with time-dependent DFT (TDDFT)[193] for different sample geometries which are interpolated in a logical way for the given system that is being calculated, making this the only version that makes the vdW interaction of an atom sensitive to its local environment. In addition, in DFT-D3, 3-body terms were explored[59], however they lowered the accuracy for the S22 reference set of molecular complexes and so are typically not used in a standard DFT-D3 calculation. Higher order ($n > 3$) many-body terms are not considered in DFT-D3.

Since it will be mentioned again below, we note that the S22 set of twenty-two dispersion-bound molecular complexes is a reference for which accurate CCSD(T) (coupled cluster with single, double, and perturbatively treated triple interactions [181]) calculations exist[205]. Many methods of calculating dispersion energies are compared using this set.

In the Tkatchenko-Scheffler (T-S) method[209], DFT+vdW, the same sum over pairwise interactions as in Equation (3.8) is retained, but here the C_6 coefficients are calculated by relating the atomic polarizability to the atomic effective volume which is found from a Hirshfield partitioning[77] of the electron density. Just as in the DFT-D method, the vdW interaction is damped in the short range and compatible with many density functionals, although the damping functions are not necessarily the same in the two methods. Recently, both many-body vdW interactions[210] and screening for binding on inorganic surfaces[192] have been added to this method, although separately.

In the van der Waals density functional (vdW-DF)[46] method, an expression for the non-local correlation energy in terms of a double integral over electron densities is derived from the adiabatic-connection fluctuation-dissipation theorem without any empiricism. Because it is formulated as a double integral, this method is pairwise. Although higher order ($n > 2$) many-body terms of the dispersion energy are not included, it can be argued that screening in metals is captured through the use of the plasmon-pole model[46, 145]. Furthermore, binding energies in agreement with experiment have been achieved for benzene on metals [140]. Due to its first-principles derivation, this method is expected to be more transferable and therefore more reliable than other vdW corrections to DFT of similar computational cost. Since it also has an accuracy comparable to the best versions of the previous two vdW corrected DFT methods, it will be used for much of the work presented below.

Higher accuracy methods are also available that carry a higher computational cost than DFT. These include CCSD(T)[181], the adiabatic-connection fluctuation-dissipation theorem (ACFDT) under the random phase approximation (RPA)[124, 125], and quantum Monte Carlo[50]. The CCSD(T) and RPA methods have a computational scaling of $O(N^5)$ to $O(N^7)$ depending on the exact method and implementation, where N is the system size, instead of $O(N^3)$ as with a typical implementation of the DFT in the GGA or LDA. Although CCSD(T) and RPA are too computationally expensive for many of the systems presented later in this dissertation, they are useful for benchmarking and understanding subtleties of the physics. With fewer approximations, they are not only more accurate, but their contributions can be understood more easily. For example, CCSD(T) and RPA energies can often be broken down diagrammatically.

3.3 van der Waals Density Functional

In this section we will begin by deriving the vdW-DF, starting with the ACFDT and then following the consequences of a series of approximations. Several sources are used from the literature[145, 124, 60, 126, 195, 125, 46] and details are filled in, when necessary. Then we will discuss a few of the versions currently available.

3.3.1 Derivation of the vdW-DF

Partition of the exchange correlation energy

We will begin by dividing the density functional theory correlation energy into a local part and a non-local part,

$$E_c = E_c^0 + E_c^{nl}, \tag{3.9}$$

where E_c^0 is given by E_c^{LDA}, the LDA correlation energy. To calculate the non-local contribution, the formally exact expression for the exchange correlation energy from the ACFDT can be used as a starting point [124, 60, 125]. We will first show how to arrive at that energy. In this section $\mathbf{x}$ is the spatial coordinate, n is the electron density operator, and the angle brackets represent taking the ground state expectation value, at a particular value of λ (defined below), where indicated. The N-electron Hamiltonian is divided into an N-body kinetic energy operator and everything else,

$$H = H_k + H_i, \tag{3.10}$$

where H_k is the N-body kinetic energy operator and

$$H_i = \frac{1}{2}\int d^3x \int d^3x' V_\lambda(\mathbf{x}-\mathbf{x}')n(\mathbf{x})[n(\mathbf{x}') - \delta(\mathbf{x}-\mathbf{x}')] + \int d^3x \nu_\lambda(\mathbf{x})n(\mathbf{x}). \tag{3.11}$$

Above, we have used the Coulomb interaction with strength λ

$$V_\lambda(\mathbf{x}-\mathbf{x}') = \frac{\lambda e^2}{|\mathbf{x}-\mathbf{x}'|}, \tag{3.12}$$

the self-energy δ-function term, and the external potential ν_λ, which is taken to ensure the density, $n(\mathbf{x})$, remains the same as λ is varied. Let E_λ be the ground state energy at a given λ. Then we can express the difference between the realistic system ($\lambda = 1$) and the system with the Coulomb interaction turned off ($\lambda = 0$),

$$\begin{aligned} E_1 - E_0 &= \int_0^1 d\lambda \frac{dE_\lambda}{d\lambda} = \int_0^1 d\lambda \left\langle \frac{\partial H_i}{\partial \lambda} \right\rangle_\lambda \\ &= \int_0^1 \frac{d\lambda}{2\lambda} \int d^3x \int d^3x' \lambda V_1(\mathbf{x}-\mathbf{x}')\langle n(\mathbf{x})[n(\mathbf{x}') - \delta(\mathbf{x}-\mathbf{x}')]\rangle_\lambda \\ &\quad + \int_0^1 d\lambda \frac{\partial}{\partial\lambda} \int d^3x [\nu_\lambda(\mathbf{x})\langle n(\mathbf{x})\rangle_\lambda]. \end{aligned} \tag{3.13}$$

The last line was obtained from

$$\int_0^1 d\lambda \int d^3x \left\langle \frac{\partial}{\partial\lambda}[\nu_\lambda(\mathbf{x})n(\mathbf{x})] \right\rangle_\lambda \tag{3.14}$$

because $n(\mathbf{x})$ is independent of λ, as mentioned above, and so the derivative can be put outside the brackets. This is the adiabatic-connection part of the ACFDT. We now define

$$\begin{aligned} E_0 &= T + \int d^3\nu_0(\mathbf{x})\langle n(\mathbf{x})\rangle, \\ E_{coul} = \frac{1}{2}\int d^3x \int d^3x' V_1(\mathbf{x}-\mathbf{x}')\langle n(\mathbf{x})\rangle\langle n(\mathbf{x}')\rangle &+ \int d^3x \nu_1(\mathbf{x})\langle n(\mathbf{x})\rangle \\ E &\equiv E_1 = T + E_{coul} + E_{xc} \end{aligned} \tag{3.15}$$

where T is the kinetic energy of a non-interacting system with the same electron density. Combining Equations (3.13) and (3.15), we obtain

$$E_{xc} = \frac{1}{2}\int_0^1 \frac{d\lambda}{\lambda}\int d^3x \int d^3x' V_\lambda(\mathbf{x}-\mathbf{x}') \times [S_\lambda(\mathbf{x},\mathbf{x}') - \langle n(\mathbf{x})\rangle\delta(\mathbf{x}-\mathbf{x}')], \tag{3.16}$$

where

$$S_\lambda(\mathbf{x},\mathbf{x}') = \langle [n(\mathbf{x}) - \langle n(\mathbf{x})\rangle] \times [n(\mathbf{x}') - \langle n(\mathbf{x}')\rangle]\rangle_\lambda. \tag{3.17}$$

Matrix form with frequency dependence

We express the static form factor $S(\mathbf{x},\mathbf{x}')$ in terms of the dynamic form factor $S(\mathbf{x},\mathbf{x}',\omega)$,

$$S(\mathbf{x},\mathbf{x}') = \int_{-\infty}^{\infty} d\omega S(\mathbf{x},\mathbf{x}',\omega), \tag{3.18}$$

where

$$S(\mathbf{x},\mathbf{x}',\omega) = \int_{-\infty}^{\infty} \frac{dt}{2\pi} e^{i\omega t}\langle [n(\mathbf{x},t) - \langle n(\mathbf{x},0)\rangle] \times [n(\mathbf{x}',0) - \langle n(\mathbf{x}',0)\rangle]\rangle. \tag{3.19}$$

Using the fluctuation-dissipation theorem[118], we can relate the dynamic form factor and the susceptibility, χ, in the following way

$$S(\mathbf{x},\mathbf{x}',\omega) = -\frac{1}{\pi} Im\chi(\mathbf{x},\mathbf{x}',\omega)\Theta(\omega). \tag{3.20}$$

where

$$\delta n(\mathbf{x},\omega) = \int d^3\mathbf{x}' \chi(\mathbf{x},\mathbf{x}',\omega) V_{ext}(\mathbf{x}',\omega), \tag{3.21}$$

$$\Theta(\omega) = 1 \text{ for } \omega \geq 0,\ 0 \text{ for } \omega < 0, \tag{3.22}$$

and V_{ext} is an external potential. We then switch to a matrix notation from Equation 3.16, replacing V_λ and S_λ with matrices in which rows represent $\mathbf{x}$ and columns represent $\mathbf{x}'$. This transforms the double space integral in that expression into a trace taken over a matrix product.

$$E_{xc} = -\frac{1}{2\pi} Im \int_0^1 d\lambda \int_0^\infty idu Tr[\mathbf{V}\boldsymbol{\chi}(\lambda,iu)] - E_{self}, \tag{3.23}$$

where E_{self} is the self energy, which was represented by the Dirac delta function in Equation 3.16. This reduces to

$$E_{xc} = -\frac{1}{2\pi}\int_0^1 d\lambda \int_0^\infty du Tr[\mathbf{V}\boldsymbol{\chi}(\lambda, iu)] - E_{self}, \tag{3.24}$$

because

$$-\frac{1}{\pi} Im \int_0^\infty i du \chi(\mathbf{x}, \mathbf{x}', iu) = S(\mathbf{x}, \mathbf{x}') = -\frac{1}{\pi}\int_0^\infty du \chi(\mathbf{x}, \mathbf{x}', iu), \tag{3.25}$$

since $S(\mathbf{x}, \mathbf{x}')$ is real. We then switch from the full screened response, $\boldsymbol{\chi}$, to the bare response, $\tilde{\boldsymbol{\chi}}$.

$$\boldsymbol{\chi}(\lambda, iu) = \tilde{\boldsymbol{\chi}}(\lambda, iu) + \lambda\tilde{\boldsymbol{\chi}}(\lambda, iu)\mathbf{V}\boldsymbol{\chi}(\lambda, iu) \tag{3.26}$$

$$\boldsymbol{\chi}(\lambda, iu) = (\mathbf{1} - \lambda\tilde{\boldsymbol{\chi}}(\lambda, iu)\mathbf{V})^{-1}\tilde{\boldsymbol{\chi}}(\lambda, iu) \tag{3.27}$$

$$E_{xc} = -\frac{1}{2\pi}\int_0^1 d\lambda \int_0^\infty du Tr[\mathbf{V}(\mathbf{1} - \lambda\tilde{\boldsymbol{\chi}}(\lambda, iu)\boldsymbol{V})^{-1}\tilde{\boldsymbol{\chi}}(\lambda, iu)] - E_{self}, \tag{3.28}$$

Full Potential Approximation

To simplify the λ integral in Equation 3.28, we assume the bare response is independent of λ and use $\tilde{\boldsymbol{\chi}}(\lambda = 1, iu)$, to obtain the expression

$$E_{xc} = \int_0^\infty \frac{du}{2\pi} Tr[\ln(\mathbf{1} - \mathbf{V}\tilde{\boldsymbol{\chi}})] - E_{self}. \tag{3.29}$$

This corresponds to the so-called Full Potential Approximation (FPA) of Ref. [123]. It is exact for the long-range vdW asymptote and also true in the random phase approximation. Later, we will use the dielectric function to approximate the susceptibility, $\tilde{\boldsymbol{\chi}}$, in the integrand, which does not include exchange and therefore from now on we label only correlation.

In the homogeneous electron gas limit we have,

$$E_c = \int_0^\infty \frac{du}{2\pi} Tr[\ln(\epsilon)] - E_{self}, \tag{3.30}$$

where ϵ is the dielectric function. So, we can subtract this from the equation above it to get

$$E_c^{nl} = \int_0^\infty \frac{du}{2\pi} Tr[\ln(\mathbf{1} - \mathbf{V}\tilde{\boldsymbol{\chi}}) - \ln(\epsilon)]. \tag{3.31}$$

Since this goes to zero in the homogeneous limit, it is consistent with the construction of a non-local contribution to the correlation energy that will be added to the LDA.

The Dielectric Function and the Plasmon Pole Model

Next we expand Equation 3.31 to second order in $S = 1 - \epsilon^{-1}$ (this is a different S than the one used above to represent the static form factor; the derivations presented in this chapter draw from a few separate sources and we have prioritized consistency with those sources over self-consistency in this case)

$$E_c^{nl} \approx \int_0^\infty \frac{du}{4\pi} Tr \left[S^2 - \left(\frac{\nabla S \cdot \nabla V}{4\pi e^2} \right)^2 \right] \tag{3.32}$$

To approximate S we take inspiration from the plasmon pole model, in which the inverse dielectric function is approximated by a single-pole function in ω[145, 86]. For our purposes, we have

$$S_{\mathbf{q},\mathbf{q}'} = \frac{1}{2}[\tilde{S}_{\mathbf{q},\mathbf{q}'} + \tilde{S}_{-\mathbf{q}',-\mathbf{q}}], \tag{3.33}$$

where

$$\tilde{S}_{\mathbf{q},\mathbf{q}'} = \int d^3r e^{-i(\mathbf{q}-\mathbf{q}')\cdot\mathbf{r}} \frac{4\pi n(\mathbf{r}) e^2/m}{[\omega + \omega_{\mathbf{q}}(\mathbf{r})][-\omega + \omega_{\mathbf{q}'}(\mathbf{r})]}. \tag{3.34}$$

We now need $\omega_{\mathbf{q}}(\mathbf{r})$ as a function of the density. To do this we use the form

$$\omega_q(\mathbf{r}) = \frac{q^2}{2m} \frac{1}{h[q/q_0(\mathbf{r})]}, \tag{3.35}$$

where $h(y) = 1 - e^{-\gamma y^2}$ and $\gamma = 4\pi/9$. The function, $\omega_q(\mathbf{r})$, is somewhat arbitrary and chosen to interpolate between a small q form of $1/2ml^2$, where l is a length scale, and the large q form of $q^2/2m$. Finally q_0 is set by considering the expression for the correlation energy above, 3.29, in the homogeneous limit, and comparing it to a GGA calculated correlation energy that is appropriate for the formalism here (see Equation 3.41). This apparent contradiction is so that at finite density gradients, the non-local correlation energy, E_c^{nl}, is connected to a form with gradient corrections. With this scheme, we have

$$E_{xc}^0 = \int d^3r \epsilon_{xc}^0(\mathbf{r}) n(\mathbf{r}) \approx \int_0^\infty \frac{du}{2\pi} Tr \ln \epsilon - E_{self} \approx \int_0^\infty \frac{du}{2\pi} TrS - E_{self}, \tag{3.36}$$

where E_{xc}^0 is the reference exchange-correlation energy that we are using to set the length scale in E_c^{nl}. After evaluating the right hand side using the above approximation for S, the exchange correlation potential is given by

$$\epsilon_{xc}^0 = \frac{e^2 q_0(\mathbf{r})}{\pi} \int_0^\infty dy[h(y) - 1] = -\frac{3e^2}{4\pi} q_0(\mathbf{r}), \tag{3.37}$$

and

$$q_0(\mathbf{r}) = \frac{\epsilon_{xc}^0(\mathbf{r})}{\epsilon_x^{LDA}(\mathbf{r})} k_F(\mathbf{r}), \tag{3.38}$$

where k_F is the Fermi wave vector,

$$k_F = (3\pi^2 n)^{1/3}, \tag{3.39}$$

and

$$\epsilon_x^{LDA}(\mathbf{r}) = -\frac{3}{4}\left(\frac{3}{\pi}\right)^{1/3} e^2 n^{1/3}, \tag{3.40}$$

the LDA exchange potential. For ϵ_{xc}^0, the expression

$$\epsilon_{xc}^0 \approx \epsilon_{xc}^{LDA} - \epsilon_x^{LDA}\left[\frac{Z_{ab}}{9}\left(\frac{\nabla n}{2k_F n}\right)^2\right] \tag{3.41}$$

is used where $Z_{ab} = -0.8491$ and the second term is the *screened exchange* of Ref. [126]. The final form can be expressed as

$$E_c^{nl} = \frac{1}{2}\int d^3r d^3r' n(\mathbf{r})\phi(\mathbf{r},\mathbf{r}')n(\mathbf{r}'). \tag{3.42}$$

ϕ is given by

$$\phi(\mathbf{r},\mathbf{r}') = \frac{2me^4}{\pi^2}\int_0^\infty da\ a^2 \int_0^\infty db\ b^2 W(a,b)T(\nu(a),\nu(b),\nu'(a),\nu'(b)), \tag{3.43}$$

where

$$T(w,x,y,z) = \frac{1}{2}\left[\frac{1}{w+x}+\frac{1}{y+z}\right]\left[\frac{1}{(w+y)(x+z)}+\frac{1}{(w+z)(y+x)}\right], \tag{3.44}$$

$$W(a,b) = 2[(3-a^2)b\cos b\sin a + (3-b^2)a\cos a\sin b + (a^2+b^2-3)\sin a\sin b \\ -3ab\cos a\cos b]/a^3b^3, \tag{3.45}$$

and

$$\nu(y) = y^2/2h(y/d) \tag{3.46}$$

$$\nu'(y) = y^2/2h(y/d') \tag{3.47}$$

$$d = |\mathbf{r}-\mathbf{r}'|q_0(\mathbf{r}) \tag{3.48}$$

$$d' = |\mathbf{r}-\mathbf{r}'|q_0(\mathbf{r}'). \tag{3.49}$$

We note that ϕ has been shown above to depend on r and r' through d and d'. At large d and d'

$$\phi \to -\frac{12(4\pi/9)^3 me^4}{d^2 d'^2(d^2+d'^2)} \tag{3.50}$$

which has the r^{-6} asymptotic form.

As a practical matter, ϕ for different d and d' can be tabulated in advance, however, this does not help the fact that the double integral in Equation 3.42 is six dimensional and therefore computationally prohibitive. To reduce that computational complexity, Román-Pérez and Soler have shown[188] that ϕ can be interpolated,

$$\phi(q_1,q_2,r_{12}) \simeq \sum_{\alpha\beta}\phi(q_\alpha,q_\beta,r_{12})p_\alpha(q_1)p_\beta(q_2), \tag{3.51}$$

where q_α are fixed values and p_α are cubic splines. With this factorized form of the kernel, the vdW self-consistent potential, total energy, and atomic forces can be calculated in $O(N\log N)$ operations[188], where N is proportional to the system volume. Thus, a tractable non-local correlation energy that does not add great computational cost to DFT, has been derived.

3.3.2 Exchange Functionals for the vdW-DF and Modifications to E_c^{nl}

In this dissertation we will focus on three versions of the vdW-DF. The first, from the original 2004 paper[46], which we will refer to simply as the vdW-DF, uses the revPBE[232] exchange functional. Several other GGA exchange functionals alone produce spurious binding in noble gas dimers where exact Hartree-Fock (HF) and revPBE do not. Physically, binding should come from E_c^{nl} and not E_x. However, revPBE is too repulsive in many cases and binding energies and distances were often over-estimated by the vdW-DF[46, 127, 128]. A revised functional, known as vdW-DF2, was published in 2010 [128] and included the PW86 exchange functional[168]. This functional paired with a matching changed parameter in E_c^{nl} (in Equation 3.41, $Z_{ab} = -0.8491$ in vdW-DF and $Z_{ab} = -1.887$ in vdW-DF2) improved results for the S22 set of dispersion bound molecular complexes. The third version pairs the same non-local correlation from the vdW-DF with the optB88 exchange functional[102]. The optB88 exchange has two parameters that were fit to the S22 dataset binding energies as calculated by CCSD(T). This functional obtains binding energies and distances in better agreement with this dataset and also gives better lattice constants, bulk moduli, and atomization energies for solids[103] than the vdW-DF with revPBE or the vdW-DF2 with PW86. Better performance on this diverse range of quantities is a good indication that the vdW-optB88 method remains transferable and not simply fine-tuned to the S22 set. However, for much of the following work, we more often use the vdW-DF2 method, which has no fit parameters.

Part II

Results and Discussion

Chapter 4

Example van der Waals Bound Systems

In this chapter results will be presented for a series of systems for which the dispersion energy is important for a qualitatively correct description (as well as one system dominated by other binding interactions). The set of systems is neither exhaustive nor an attempt to be representative of typical vdW dominated systems. However, the following examples should provide a good primer for the more complicated systems to follow in that several basic binding geometries are considered (interatomic, interplanar, and atom on plane) and calculated results are compared to experiment.

4.1 Noble Gas Dimers

We begin with calculations on the interaction energy between a dimer of krypton, a noble gas that would not bind if not for the van der Waals force. The 2004 paper on the first version of the vdW-DF for general geometries[46] reported results for these dimers which are reproduced here and compared to computations using the PBE GGA[170], vdW-DF2[128], and vdW-optB88 methods[102].

4.1.1 Computational Details

The PBE and vdW-DF calculations were performed using the Vienna Ab Initio Simulation Package(VASP)[112, 113, 110, 111] with the vdW-DF implementation due to Jiří Klimeš[103]. The projector-augmented wave (PAW) scheme[22, 114] is utilized with the potentials taken from the VASP PBE library. The electronic wavefunctions were expanded in a plane wave basis with a cutoff of 500 eV. A single k-point (Γ) was found to be sufficient to sample the Brillouin zone, due to the large size periodic cell of 24×12×12 Å. With these parameters, binding energies are estimated to be converged to better than 1 meV. Binding energies for the Kr dimer are given by

$$E_{bind}^{Kr_2} = E_{total}^{Kr_{AB}} - E_{total}^{Kr_A} - E_{total}^{Kr_B}, \tag{4.1}$$

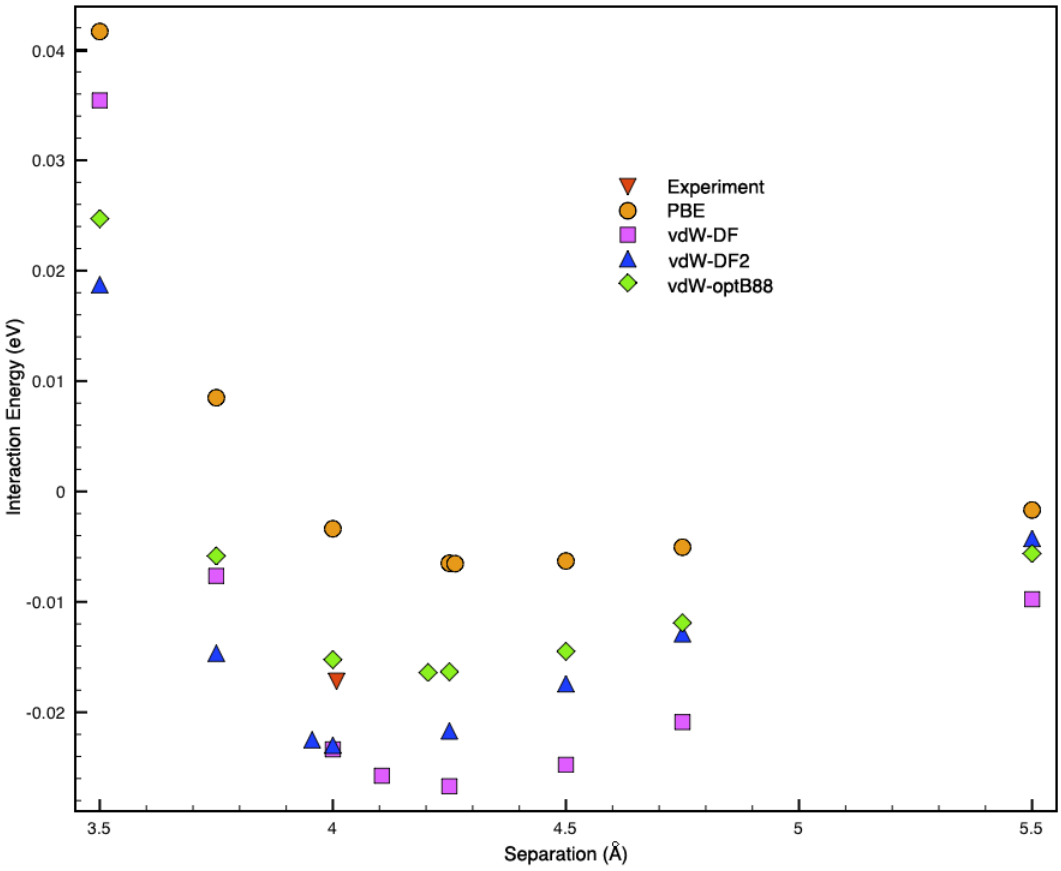

Figure 4.1: Calculated interaction energies between two Kr atoms using PBE, vdW-DF, vdW-DF2, and vdW-optB88. The experimental data point is from Ref. [162]

where $E_{total}^{Kr_{AB}}$ is the total energy of the combined two-Kr system and $E_{total}^{Kr_A}$ and $E_{total}^{Kr_B}$ are the total energies of the isolated constituent Kr A and Kr B at the same positions in the periodic cell as in the combined system. Zero-point energies are not calculated, but are expected to be small since the potential energy well is not steep and the Kr atoms are relatively heavy.

4.1.2 Results

In Figure 4.1, the interaction energies calculated with PBE, vdW-DF, vdW-DF2, and vdW-optB88 are presented for a pair of Kr atoms at various separations as well as the experimental equilibrium bond length (4.0 Å) and energy (-17 meV)[162]. The calculated and experimental binding separations and energies are also given in Table 4.1. PBE predicts binding that is too weak (-6.5 meV) and at too large a separation (4.26 Å), which is consistent with this functional neglecting the van der Waals interaction. The vdW-DF predicts binding that is too strong (-26.7 meV) and at too large a separation (4.25 Å), while the vdW-DF2 gives better results for both (-23.0 meV and 4.00Å). The vdW-optB88

Table 4.1: Kr binding separations and binding energies with an estimated accuracy of 0.05 Å and 1 meV, respectively.

Method	Separation(Å)	Binding Energy(meV)
Experiment	4.01	-17
PBE	4.26	-6.5
vdW-DF	4.25	-26.7
vdW-DF2	4.00	-23.0
vdW-optB88	4.20	-16.4

method yields the most accurate binding energy (-16.4 meV), but at too great a separation (4.20 Å).

4.2 Graphite

Graphite is a prototypical layered van der Waals bound solid with experimental data available on its cohesive energy and interlayer spacing[231, 135]. Thus, it is an ideal test case for the calculation of binding between 2 dimensional sheets using the vdW-DF.

4.2.1 Computational Details

Similar methods to those described in Section 4.1.1 are employed. The plane wave cutoff is at 500 eV and the hard carbon PBE PAW potential is used (this is a PAW potential calculated with a higher than usual plane wave cutoff, 900 eV). The periodic unit cell consists of two layers in the AB stacking arrangement, each layer containing two atoms in the cell. In-plane bond distances are fixed to the experimental value of 2.46 Å[135] and the out-of-plane separation is varied to find the equilibrium distance. A 16×16×4 k-point grid is used, centered at Γ.

4.2.2 Results

Table 4.2: Graphite equilibrium inter-layer separation and cohesive energy (compared to graphene).

Method	Separation(Å)	Cohesive Energy(meV/atom)
Experiment	3.33[135]	-52±5[231]
vdW-DF	3.58	-52
vdW-DF2	3.51	-51
vdW-optB88	3.34	-68

Ground state graphite structures are calculated using three different methods: the vdW-DF, the vdW-DF2, and vdW-optB88. After finding the equilibrium separation, cohesive energies, compared to isolated single layer graphene sheets, are calculated. We

observe that the vdW-optB88 method yields the inter-layer spacing (3.34 Å) that is closest to experiment (3.33 Å). The vdW-DF and vdW-DF2 calculations produce cohesive energies (-52 and -51 meV/atom, respectively) in good agreement with the measured quantity (-52 meV/atom). These results are close in value to finer grained calculations presented more recently in Ref. [56], however, the cohesive energies calculated in that work with vdW-DF2 and vdW-optB88 are slightly smaller in magnitude (-48 meV and -65 meV, respectively). Those calculations utilize hard PAW potentials, a 900 eV plane wave cutoff, a 24×24×2 k-point grid, and relaxed in-plane atomic positions. In addition, after the zero-point energy corrections are added in Ref. [56], it was found that the interlayer spacing is slightly increased (by .03-.04 Å) and the cohesive energies are reduced to -44 meV and -61 meV for the vdW-DF2 and vdW-optB88 methods, respectively. Thus the cohesive energy produced by vdW-optB88 is in slightly better agreement with the experimental value when the zero-point energy is considered.

4.3 Metal Adatoms and H_2 on Graphene

Adatom adsorption on graphene can be used to chemically electron-dope or hole-dope the material[163, 33, 24, 175, 54]. Furthermore, adatoms may possibly be used in the engineering of the spin-orbit interaction[28] in graphene to create a quantum spin hall (QSH) state[220]. Chan et al. reported on DFT studies of 12 metal adatoms on graphene in Ref. [31]. In the following we reproduce their results for the binding of Li and Al in the hollow position (above the center of a graphene hexagon) using PBE and compare with results from the vdW-DF2 and vdW-optB88 methods to see if the dispersion energy contribution is significant.

The energetics of H_2 binding on graphene is a key metric for its feasibility as a hydrogen storage material. Previous DFT studies have utilized LDA and GGA density functionals to calculate the binding energy of molecular hydrogen on graphene[74] and graphite[90]. However, these methods are expected to overbind and underbind H_2, respectively, as reported in Ref. [74]. That work treated the results of those functionals as upper and lower bounds for the interaction energy. In work presented below, we employ the PBE, vdW-DF2, and vdW-optB88 functionals for the study of H_2 binding on graphene.

4.3.1 Computational Details

Following Ref. [31], the electronic wave functions are expanded in a plane wave basis with an energy cutoff of 500 eV. The hard C, standard Al, Li with the 1s states treated as valence, and hard H PBE PAW potentials are used. The graphene lattice constant is set to 2.47 Å and the unit cell utilized in these calculations is equal to 4×4 graphene primitive cells for a total of 32 carbon atoms. It is periodic in the z direction, with a length of 15 Å. There is one adsorbed metal atom or hydrogen dimer per unit cell. Li and Al are relaxed in the center of graphene hexagon and all atoms are allowed to relax. The H_2 molecule is relaxed in the *D* position, as described in Ref. [74] and shown in Figure 4.2. A 9×9×1 k-point grid, centered on the Γ point, is used. Dipole corrections are made, as in Ref. [31]. Spin-polarized calculations are used to obtain the correct ground state for isolated Li and

Al, all other calculations are non-magnetic.

4.3.2 Results

Table 4.3: Binding separation and interaction energy for Li and Al on graphene, in the center of a carbon hexagon, as calculated with PBE, vdW-DF2, and vdW-optB88. PBE results from Ref. [31] are in parentheses.

Adatom	Method	Separation(Å)	Interaction Energy(eV)
Li	PBE	1.71(1.71)	-1.09(-1.10)
	vdW-DF2	1.61	-0.89
	vdW-optB88	1.76	-1.18
Al	PBE	2.11(2.13)	-1.00(-1.04)
	vdW-DF2	2.26	-0.65
	vdW-optB88	2.14	-1.18

Table 4.3 lists the binding separations and energies, calculated with PBE, vdW-DF2, and vdW-optB88 for Li and Al on graphene. The PBE results were published previously in Ref. [31]. In that work, it was determined that Li and Al were primarily ionically bound to the graphene. This results in shorter binding distances and larger binding energies than are typically observed for dispersion dominated binding. Interestingly, the PBE determined binding energies have magnitudes between the results from vdW-DF2 and vdW-optB88. This contradicts the expectation that the vdW corrected methods would both have stronger binding, due to the added dispersion interaction.

The weaker binding observed with the vdW-DF2 may be due to the exchange functional, PW86, which has a larger enhancement factor than the exchange functional for vdW-optB88 for values between 1 and 3 of the reduced gradient (Figure 2.1). The vdW-DF2 is accurate for dispersion bound systems, for instance, the mean absolute deviation in the S22 data set (see Chapter 3) is less than 22 meV[128], and lattice constants are reasonable for solids (typically within 5% of experiment[103]). However, the vdW-DF2 gives qualitatively incorrect results for benzene on Pt (calculated interaction energy of -0.34 eV vs. experimental energy of -1.57 to -1.91 eV). This is a system which combines binding of a covalent character with a strong dispersion interaction[140]. In that same system, PBE also underestimates the binding energy (-0.81 eV) while the vdW-optB88 method produced results in good agreement with experiment (-1.84 eV)[140]. Thus, for the mixed binding system, Al and Li on graphene, it is consistent with previous results to hypothesize that the smaller binding energies for vdW-DF2 and PBE are less accurate than the results calculated with vdW-optB88. The latter method produces interaction energies that are stronger than PBE by -0.09 and -0.18 eV for Li and Al, respectively, which may be attributed to the dispersion energy contribution.

Finally, we present the results of a comparison of the vdW-DF2 and vdW-optB88 methods with two different GGA functionals, PW91 and PBE, and LDA for the binding of molecular hydrogen on graphene in Table 4.4. The binding position, depicted in Figure 4.2, corresponds to the strongest binding, as calculated with several methods[74]. The system

Table 4.4: Binding energies and separations for molecular hydrogen on graphene in the position indicated in Figure 4.2. LDA and PW91 results taken from Ref. [74]. The experimental result is for H_2 on graphite[215].

Method	Separation(Å)	Binding Energy(meV)
LDA[74]	2.7	-93
PW91[74]	3.3	-24
PBE	3.3	-12
vdW-DF2	3.0	-70
vdW-optB88	3.0	-77
exp.[215]	2.87	-41.6

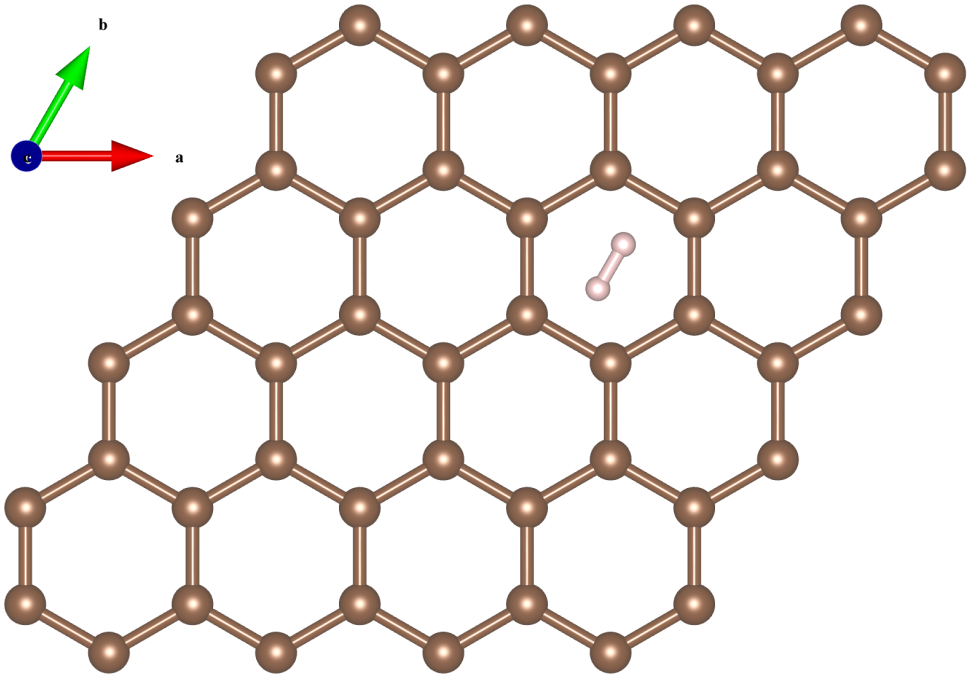

Figure 4.2: H_2 on graphene.

is expected to be primarily dispersion bound, which is consistent with the H_2-graphene separation of ∼3 Å and the lack of charge transfer[74]. The vdW-DF2 and vdW-optB88 schemes predict binding energies and separations between the values predicted by LDA and the GGA type functionals. Notably, the two vdW methods give more consistent results (within 10%) for this vdW dominated system than for the ionically dominated metal on graphene binding described above. Vidali et al., in reference [215], give a best estimate of -41.6 meV for the binding energy and 2.87 Å for the separation of H_2 on graphite, based on several experimental studies. While this energy is roughly 30 meV lower in magnitude than our vdW-DF calculated values, the calculated values do not include zero-point energy corrections. These corrections should reduce the binding energy magnitude, bringing the

vdW-DF2 and vdW-optB88 results closer to the experimental value and the PW91 result further from experiment. Thus, of the methods presented, vdW-DF2 and vdW-optB88 likely produce the most accurate binding energies.

4.4 Conclusion

In this chapter we have examined several systems using versions of the van der Waals density functional. In the Kr dimer, graphite, and H_2 on graphene, the attraction is dominated by the dispersion interaction[46, 56, 74]. Therefore, for these systems, the LDA and GGA density functionals are not expected to give qualitatively correct results since they do not capture the energy associated with non-local electron correlation. For example, PBE predicts a binding energy for the Kr dimer of -6.5 meV, less than half the measured value. In these systems the binding/cohesive energies per atom are calculated with vdW-DF type methods to be less than 70 meV in magnitude, consistent with dispersion dominated attraction. In addition, these results agree reasonably well with experiment.

For Li and Al on graphene, the binding energy is much higher in magnitude, $\sim$1 eV, and of an ionic character. For ionic interactions, PBE can be expected to predict reasonable binding energies[31]. However, the vdW-DF2 calculated adsorption energy is 35% smaller for Al on graphene than the value calculated with PBE. The smaller binding energy is most likely due to a more respulsive exchange functional. On the other hand, vdW-optB88 calculated binding energies are marginally stronger than the PBE results, consistent with the additional dispersion energy.

Chapter 5

van der Waals Density Functional Study of CO_2 Binding in Zeolitic Imidazolate Frameworks

The van der Waals density functional (vdW-DF) formalism is employed in a study of the binding energetics for CO_2 in a set of five zeolitic imidazolate framework (ZIF) compounds. The ZIF structures investigated share the same **rho**-type zeolite topology and metal atoms, but feature imidazolate linkers with different chemical functionalization. Three distinct binding sites are identified, for which the binding energies are found to show different dependencies on the functionalization of the linker molecules. The origin of the variations in the binding energies across the ZIF compounds is discussed through analyses of the binding geometries and charge-density distributions. A comparison of the vdW-DF results with those obtained by generalized-gradient-approximation calculations highlights the important contribution of the non-local correlation energy to the CO_2 binding energies in these compounds.

5.1 Forward

The work presented in this chapter was published by K. G. Ray, D. Olmsted, N. He, Y. Houndonougbo, B. B. Laird and M. Asta, in Phys. Rev. B, vol. 85, 085410 (2012)[185], and is reproduced here with permission of the co-authors and publishers.

Ning He, Brian Laird, and Yao Houndonougbo provided and tested the OPLS and UFF parameters for the classical force field calculations. David Olmsted assisted with the configuration of LAMMPS and the automation necessary for the classical force field calculations. Colin Ophus helped with some of the initial potential energy landscape plots and William Morris provided Figure 1(c). Mark Asta, Brian Laird, and David Olmsted provided useful discussion and feedback.

5.2 Introduction

Zeolitic imidazolate frameworks (ZIFs) are a class of metal-organic-framework compounds that have received widespread interest for applications involving capture, storage and separation of molecular gas species [174, 70, 214, 166, 85, 13]. As illustrated in Fig. 5.1, for the example of ZIF-96, the structures of ZIF compounds are characterized by a tetrahedral coordination of the metal ions to the nitrogen atoms on the imidazole organic linker molecules. The geometry of the linkers dictates that the bond angle between the metal ions is close to 145 degrees, which is similar to that associated with the Si-O-Si bonds connecting SiO_4 tetrahedra in zeolite compounds. Consequently, ZIFs are observed to assemble in many of the same topologies as zeolites. Experimental efforts over the past five years have demonstrated that ZIF compounds can be formed with a range of structural topologies and compositions. ZIFs have been synthesized using different metal ions (e.g., Co and Zn), and with linkers featuring a variety of different functional groups, which can be attached to the 2 or 4 and 5 sites of the imidazole ring [174].

Due to the wide variety of possible topological and compositional variations, a detailed understanding of the factors that govern gas adsorption is desired to guide optimization of ZIF compounds for gas storage and separation applications. Experimental measurements have demonstrated a pronounced dependence on ZIF chemical compositions and structural topologies, for the equilibrium adsorptions of H_2, CO_2, CH_4, N_2, and CO gases and their mixtures[174, 2, 156, 134, 172, 82]. Neutron-scattering, spectroscopy measurements, and Monte-Carlo computer simulations [5, 7, 17] have provided important insights related to these results, by demonstrating that the gas molecules bind primarily in sites localized near the atoms in the imidazolate linkers in ZIF compounds[35, 25, 225, 234, 7, 156, 139, 61, 66, 79, 130, 138, 183, 200, 223]. The magnitudes of the binding energies underlying the interactions between the gas species and ZIF linkers can be estimated based on the measured isosteric heat of adsorption, e.g., 0.24 eV (23 kJ mol^{-1}) for CO_2 in ZIF-69 [172].

The interactions between gas and linker molecules in ZIF compounds have been investigated theoretically for a few ZIFs using quantum-chemistry methods. Focusing specifically on the case of CO_2 molecules, of interest in the present study, the nature of these interactions have been investigated for isolated fragments of the 2-nitrobenzimidazolate (nbIM) and methylbenzimidazolate (MebIM) linkers in ZIF-78 and ZIF-79[130], and for embedded clusters involving the benzimidazolate (bIM), nbIM, and 5-chlorobenzimidazolate (cbIM) linkers in ZIF-68 and ZIF-69[79]. In Ref. [130], binding energies ranging between -0.0518 eV (-5.00 kJ mol^{-1}) and -0.1371 eV (-13.23 kJ mol^{-1}) were obtained. The geometries of the strongest binding sites in these studies involved two types of interactions. In the first the C atom in CO_2 is located at distances 2.8 to 3.15 Å from the O atoms in the -NO_2 groups on the nbIM linkers, or the N atoms in the imidazole ring. The second involved hydrogen bonds between the O atoms in CO_2 and H atoms attached to the benzene ring.

In the current work we employ the framework of the van der Waals density functional (vdW-DF)[46, 128] in a computational study of the energetics of CO_2 binding in the set of five ZIF compounds illustrated in Fig. 5.1. These compounds are referred to as ZIF-25, ZIF-71, ZIF-93, ZIF-96 and ZIF-97, and are described in detail in Ref. [156]. These ZIFs share the same **rho**-type zeolite topology, and differ only in the nature of the functional

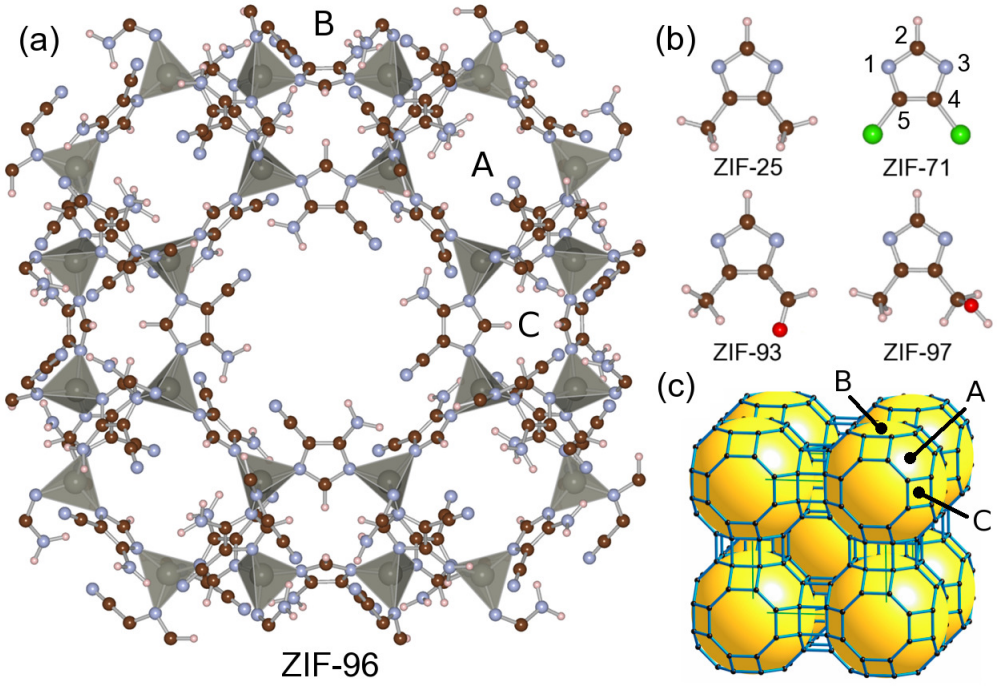

Figure 5.1: Structure of the **rho**-topology ZIFs considered in this chapter, with important binding sites A, B, C labeled. Purple spheres are nitrogen, red are oxygen, brown are carbon, green are chlorine, light rose are hydrogen, and the grey tetrahedra are centered on the zinc atoms. (a) ZIF-96 as an example, viewed along the [100] direction. The functional groups in ZIF-96 are -NH_2 and -CN (b) The structure and composition (functional groups in parentheses) of the linkers in ZIF-25 (-CH_3), ZIF-71 (-Cl), ZIF-93 (-CH_3, -CHO), and ZIF-97 (-CH_3, -CH_2OH). Imidazolate site labels are given for ZIF-71. (c) A representation of the BCC periodic structure of zeolite **rho** topology, where vertices correspond to zinc positions, and the large yellow spheres represent the size of the pores within the framework.

groups attached to the 4 and 5 sites of the imidazole linkers (see Section 5.4). The **rho**-type net consists of a BCC arrangement of truncated cuboctohedra along with smaller space filling polyhedra, see Fig. 5.1(c). In a previous experimental and computational study of CO_2 uptakes in these compounds [156], the measured adsorptions were shown to vary by a factor of 3.3 at 298K and a gas pressure of 103 kPa. Additionally, Monte-Carlo simulations based on classical force fields were used to identify the main binding sites, and established the importance of electrostatic interactions for compounds featuring asymmetric linkers (i.e., different functional groups on the 4 and 5 sites of the imidazole ring). Due to the variation in equilibrium adsorptions displayed by these compounds, and the fact that they differ only in the composition of their linkers, they represent an ideal set of structures for probing the nature of CO_2 interactions with ZIF framework atoms, and the ways in which these interactions can be altered through variations in linker chemistry.

In the next section we describe the approach employed in the present work, based on the use of the vdW-DF. This approach offers a methodology within density-functional-theory (DFT) for incorporating non-local correlation contributions to the total energy, which are known to be critical for accurately modeling non-bonded interactions in molecules and solids[46, 128, 102, 103]. Due to relatively recent algorithmic developments[188], vdW-DF calculations can be performed with a computational expense only moderately increased relative to standard DFT methods. The vdW-DF formalism is thus well suited to studies of gas binding in metal-organic-framework materials such as ZIFs[107, 108, 106]. Specifically, the formalism allows one to perform direct calculations of gas binding energies in fully periodic structures, incorporating in a natural way simultaneous interactions with multiple linkers (e.g., in small apertures), and the steric constraints imposed by the topology of the framework. After describing the details of the computational approach, the results from DFT are presented and compared with those obtained from classical force fields in Section 5.4. An analysis of the binding geometries and energies is given in Section 5.5. A short summary of the main conclusions is given in Section 5.6.

5.3 Methods

The computational approach employed in this work involves a combination of classical force field (FF) and vdW-DF calculations. The former are used to map the potential energy landscape of the CO_2 molecule within the unit cell of the ZIF compound. The most stable binding geometries identified from these calculations are then used as a starting point for vdW-DF calculations in which the positions of the atoms in the CO_2 molecule are relaxed to a local minimum. The framework atomic positions are taken from experiment[156] and remain fixed. The remainder of this section describes the details surrounding both the classical force-field and vdW-DF calculations.

5.3.1 Classical simulations

The classical simulations employed in this work were used to map out the potential energy landscape of a single CO_2 molecule within the ZIF framework, as a function of the position of its center of mass, and its angular orientation. The calculations employed

force fields including van der Waals interactions modeled with Lennard-Jones potentials, and electrostatic interactions modeled through the assignment of partial charges on each of the atoms. The Lennard-Jones potential parameters and partial charges for CO_2 were taken from the elementary physical model 2 (EPM2) force field of Harris and Yung[69]. For the framework atoms the Lennard-Jones parameters were taken from the Optimized Potentials for Liquid Simulations (OPLS) set[96] that most closely represented the chemical coordination of the functional groups. Lennard-Jones parameters between CO_2 and framework atoms were derived using Lorentz-Berthelot mixing rules[80]. Partial charges for the framework atoms were derived from electrostatic potentials, computed from Perdew-Burke-Ernzerhof (PBE)[170] generalized gradient approximation (GGA) DFT calculations, using the Repeating Electrostatic Potential Extracted ATomic (REPEAT) charges algorithm[26], as described in detail in the supplementary material to Ref. [156].

Energies for a single molecule in a single cubic unit cell of the ZIF compound were computed using the Large-scale Atomic/Molecular Massively Parallel Simulator (LAMMPS) molecular-dynamics code[177] with charge interactions summed using a particle-particle particle-mesh Ewald (PPPM) technique[178]. Appropriate energies for the ZIF and molecule alone were subtracted to compute binding energies. The binding energies were computed sampling the center-of-mass position of the CO_2 molecule on a rectangular grid with steps $L/128$, where L is the length of a side of the cubic unit cell. The symmetries of the ZIF structure were used to reduce the number of actual computations. CO_2 was treated as a linear rigid molecule and energies were computed for 61 orientations at each center-of-mass position. These consisted of all the <100>, <110>, <111>, <321>, <2.414 1 0>, and <2.732 1 1> directions over the half-sphere. The results plotted in Fig. 5.2 represent the minimum energies over these 61 orientations, for each center-of-mass position.

5.3.2 van der Waals DF calculations

For the three most stable binding sites obtained from the classical simulations described above, we undertake calculations of CO_2 binding energies employing the formalism of the vdW-DF[46]. In this formalism, the vdW contribution to the total energy is described through modifications to the correlation energy functional within DFT. Specifically, the DFT exchange-correlation functional is divided into three parts:

$$E_{xc} = E_{lc} + E_{nlc} + E_x, \tag{5.1}$$

where E_{lc} is a local correlation energy described within the local density approximation, E_{nlc} is the nonlocal correlation energy, and E_x is a semi-local exchange functional. The E_{nlc} contribution is given by the integral:

$$E_{nlc} = \frac{1}{2} \int d\mathbf{r} d\mathbf{r}' n(\mathbf{r}) \phi(\mathbf{r}, \mathbf{r}') n(\mathbf{r}'), \tag{5.2}$$

over electron densities, n at $\mathbf{r}$ and $\mathbf{r}'$, multiplied by an integration kernel, ϕ, which is derived from the adiabatic-connection theorem through a series of approximations [46]. We consider three different exchange functionals for use with the vdW-DF approach, as proposed previously in the literature[46, 128, 102, 103]. These are revPBE[232], as in the

original vdW-DF [46], PW86[168], as in vdW-DF2 [128], and optB88 [102], a new exchange functional based on the B88 exchange functional [18]. E_{nlc} in the original vdW-DF and the optB88 formulation are based on the same parameterization. By contrast, E_{nlc} in vdW-DF2 has a single changed parameter, which relates how the length scale in E_{nlc} is set by a corresponding generalized-gradient-approximation (GGA) calculation. In vdW-DF2 and vdW-DF this parameter comes from energy expansions appropriate for molecules or a slowly varying electron gas, respectively. The PW86 and optB88 functionals were shown to be the most accurate for the S22 data set of dispersion bound molecular complexes[128, 102]. In what follows we use the vdW-DF2 functional in calculating binding energies for all five ZIFs listed in Fig. 5.1. For comparison purposes, we also present results using the vdW-DF, optB88 and PBE-GGA[170] functionals for ZIF-25 and ZIF-96.

The PBE and vdW-DF calculations were performed using the Vienna Ab Initio Simulation Package (VASP)[112, 113, 110, 111] with the vdW-DF implementation due to Jiří Klimeš[103]. The projector-augmented wave (PAW) scheme[22, 114] is utilized with the potentials taken from the VASP PBE library. The electronic wavefunctions were expanded in a plane wave basis with a cutoff of 550 eV. A single k-point (Γ) was found to be sufficient to sample the Brillouin zone, due to the large size of the ZIF unit cell. In the calculations, the position, bond lengths and bond angles of the CO_2 molecule were optimized with a convergence criteria for the forces of 0.01 eV/Å. With these parameters, binding energies are estimated to be converged to better than 2 meV.

5.4 Results

The five ZIF compounds considered in this work share the same **rho** topology, illustrated in Fig. 5.1, and feature Zn ions coordinated to the following linkers: $C_5H_8N_2$ **dmeIm** (ZIF-25), $C_3H_2N_2Cl_2$ **dcIm** (ZIF-71), $C_5H_6N_2O$ **aImeIm** (ZIF-93), $C_4H_4N_4$ **cyamIm** (ZIF-96) and $C_5H_8N_2O$ **hymeIm** (ZIF-97). These linkers feature the following functionalizations on the 4, 5 sites of the imidazole ring: two -CH_3 groups (ZIF-25), two -Cl atoms (ZIF-71), one -CHO and one -CH_3 group (ZIF-93), one -CN and one -NH_2 group (ZIF-96), and one -CH_2OH and one -CH_3 group (ZIF-97).

The results of the classical force-field calculations of potential-energy landscapes are shown in Fig. 5.2. This figure plots the binding energies of a single CO_2 molecule, minimized with respect to angular orientation, as a function of the center of mass position. The results illustrate that there are three main binding sites common to each of the ZIF structures. These sites are labeled *A*, *B*, and *C* in the middle panel of Fig. 5.2. The same sites are also labeled in Fig. 5.1(a,c) to establish the relationship between the plots in Fig. 5.2 and the framework atoms.

Site *A* lies in the hexagonal connection between the large Linde Type A (*lta*) pores along the <111> direction from the center of the pore in Fig. 5.1. This site is surrounded by a six-fold ring of Zn ions connected by six linkers. Site *B* lies in the bridging double 8-fold rings (*d8r*) connecting the pores along the <100> direction. Site *C* corresponds to a binding site on the inner surface of the pore along the <110> direction near the 4-fold zinc ring (see Fig. 5.1(a,c)). The multiplicity of these binding sites per primitive unit cell is *A*: 4, *B*: 3, *C*: 12.

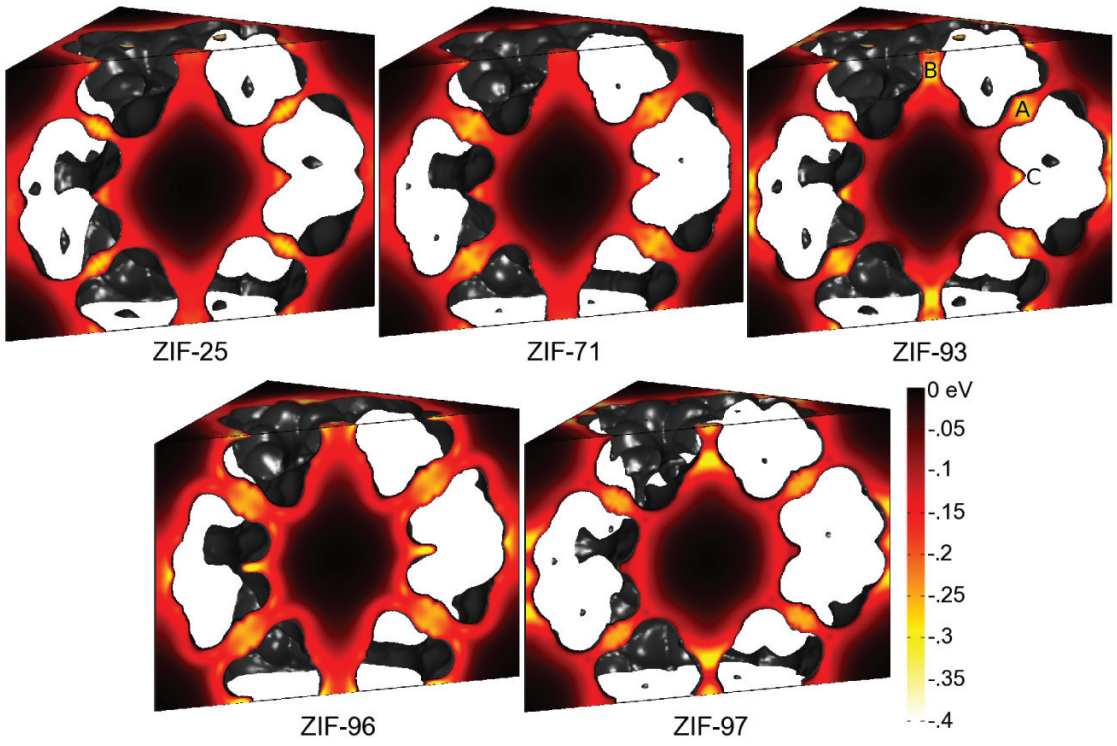

Figure 5.2: CO_2 binding energies derived from classical force fields are plotted as a function of the center-of-mass position within the five **rho**-topology ZIFs considered in this work. The slice corresponds to a (110) plane centered on the middle of the pore for each unit cell. The 3 dominant binding sites, common to each structure, are labeled A, B, and C on the plot for ZIF-93. The positions of the same three points are also labeled on Fig. 5.1 to reference the positions in this figure to the atomic sites.

Table 5.1: A comparison of CO_2 binding energies (in eV) calculated with classical force-fields (FF), PBE and three different vdW-DF methods. Results are listed for each of the three binding sites A, B and C in ZIF-25 and ZIF-96.

ZIF	Site	FF	PBE	vdW-DF	vdW-DF2	vdW-optB88
	A	-0.299	-0.090	-0.461	-0.419	-0.463
25	B	-0.210	-0.047	-0.329	-0.235	-0.272
	C	-0.254	-0.053	-0.359	-0.319	-0.367
	A	-0.286	-0.039	-0.467	-0.376	-0.440
96	B	-0.306	-0.105	-0.401	-0.385	-0.433
	C	-0.342	-0.134	-0.388	-0.434	-0.475

In Fig. 5.2 it is apparent that the strength of the binding energies for site A is fairly constant across the different structures, with a value of approximately -0.3 eV predicted by the classical force field. By contrast, larger variations are seen for the strength of the binding in sites B and C. Specifically, sites B and C show the weakest binding in ZIF-71 (-0.19 eV) and ZIF-97 (-0.15 eV), respectively, and the strongest binding in ZIF-96 (-0.31 eV for site B and -0.34 eV for site C). These variations in binding energies in sites B and C correlate with the fact that ZIF-71 and ZIF-97 show the lowest two measured CO_2 adsorptions, while ZIF-96 shows the highest [156].

In Table 5.1 classical FF, PBE and vdW-DF calculated results are listed for the binding energies in sites A, B and C in ZIF-25 and ZIF-96. The PBE binding energies are considerably smaller in magnitude than the binding energies derived from the vdW-DFs, as well as the classical force-fields. Given that the classical models produce adsorption values in reasonable agreement with measurements, the PBE functional significantly underestimates the strength of the binding energy for the CO_2 molecules in the ZIF frameworks. This result is not surprising given that the dispersion contributions to the non-bonded interactions are not properly accounted for in this functional. The vdW-DF methods are seen to lead to significantly larger magnitudes for the binding energies than PBE. The differences between PBE and vdW-DF results can be viewed as a manifestation of the sizeable contributions arising from the non-local correlation energy in the latter formalism.

The vdW-DF binding energies in Table 5.1 are generally larger in magnitude than the values obtained with the classical FFs. This general trend is also observed in a comparison of vdW-DF and FF results for the three binding sites in the three other **rho**-structured ZIF compounds considered in this work (71, 93, and 97). The reason for this trend may be partly due to polarization effects which are not explicitly accounted for in the classical FF results. For example, we note that the vdW-DF2 results for the B site show relatively small differences with the FF results in ZIF-25, while the differences are much larger for this site in ZIF-96. As shown in the next section, the charge density redistribution on the functional groups induced by the CO_2 molecule are much larger in magnitude for ZIF-96 than for ZIF-25. Thus, explicit inclusion of polarization terms in the classical FFs may be required to accurately reproduce the magnitudes of the binding energies, and associated variations across the different compounds, obtained by the vdW-DF calculations.

The differences between the binding energies obtained with the different vdW density functionals in Table 5.1 are largely consistent with trends reported previously in

Table 5.2: CO_2 binding energies (in eV) calculated by vdW-DF2 for binding sites A, B and C in five **rho**-structured ZIFs. The contribution of the non-local correlation (nlc) energy to the binding energy is listed in parentheses.

ZIF	Site A total (nlc)	Site B total (nlc)	Site C total (nlc)
25	-0.419 (-0.437)	-0.235 (-0.275)	-0.319 (-0.430)
71	-0.413 (-0.469)	-0.323 (-0.367)	-0.310 (-0.393)
93	-0.373 (-0.465)	-0.408 (-0.282)	-0.433 (-0.469)
96	-0.376 (-0.444)	-0.385 (-0.393)	-0.434 (-0.449)
97	-0.460 (-0.465)	-0.464 (-0.268)	-0.250 (-0.219)

the literature. Specifically, the original vdW-DF is known to over-bind at greater than equilibrium separations for dispersion bound systems and predict equilibrium bond lengths that are too large for such systems[46, 102, 128]. The vdW-DF2 method was designed to improve the method in both regards[128]. Most of the vdW-DF results in Table 5.1 show larger binding energies relative to vdW-DF2. One exception is the C site in ZIF-96; the smaller magnitude of the binding energy for this site predicted by vdW-DF relative to vdW-DF2 may be due to the larger bond lengths predicted in the former functional and the possibility that the bonding geometry is more optimally satisfied for the latter. For completeness, we also include in Table 5.1 results for the recently developed vdW-optB88 functional[102]. This functional yields magnitudes for the binding energies that are uniformly larger than vdW-DF2, and in some cases larger than those obtained with vdW-DF.

Overall, the results in Table 5.2 show a relatively large variation (by as much as 0.09 eV) in the binding energies predicted by the different vdW-DF theories, and also highlight the significantly larger magnitudes of the vdW-DF binding energies relative to those obtained with the classical FF (as large as 0.12 eV). Unfortunately, the available experimental data for CO_2 adsorption in the **rho**-structured ZIF compounds considered here[156] does not provide a basis for direct comparisons with the results presented in Table 5.2. Thus, to better assess the relative accuracy of the different vdW-DF formalisms in their application to CO_2 adsorption in the ZIF compounds studied here and the performance of the classical FFs, direct experimental measurements of binding energies and/or vibrational frequencies would be particularly useful. In the remainder of this paper we will focus on results obtained with the vdW-DF2 method. The main emphasis in what follows will be the trends in the energetics across the different compounds, and the nature of the interactions underlying CO_2 binding.

Calculated binding energies, obtained with the vdW-DF2 formalism, are listed in Table 5.2 for the three major binding sites in ZIF-25, 71, 93, 96, and 97. Consistent with the results obtained with the classical force fields, the binding energies for the A site show relatively small variations across the five ZIF compounds: these energies vary by approximately ten percent about the mean value of -0.41 eV. By contrast the binding energies for sites B and C show variations in the range of 0.2 eV across the different compounds. For site B the magnitude of the binding energy is significantly larger for the three ZIFs (93, 96 and 97) featuring linkers with asymmetric functionalizations, i.e., two

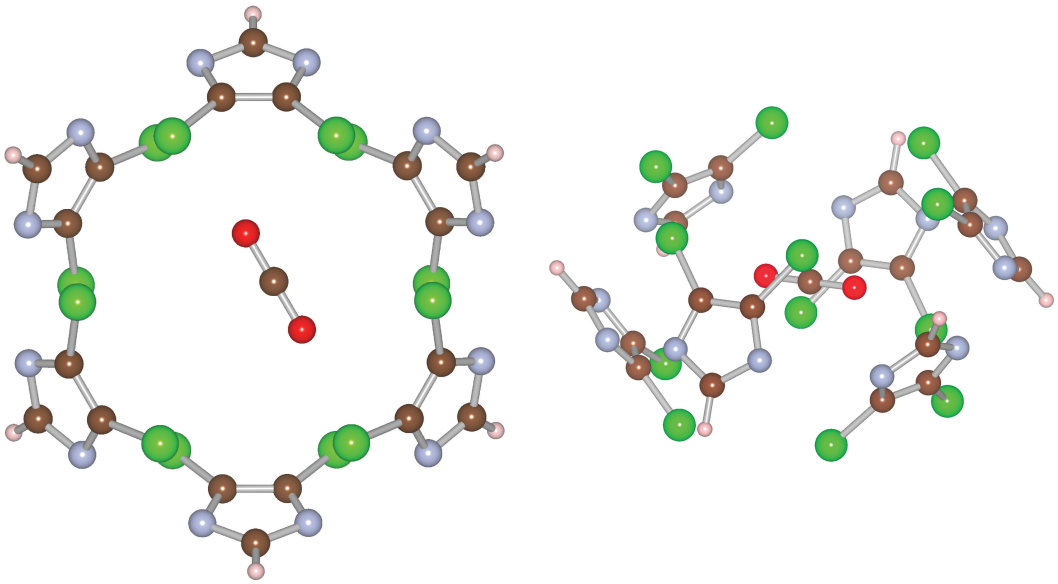

Figure 5.3: The position of the CO_2 molecule in binding site A of ZIF-71 is shown in relation to the six nearest **dcIm** imidazole linkers in a view along the [111] direction (left) and in a view along a direction slightly rotated out of the (100) plane (right).

different functional groups on the 4 and 5 sites. For site C this trend is also observed, but with the exception of ZIF-97 which features the binding energy with the smallest magnitude. In the next section we discuss the origins of the variations in the binding energies listed in Table 5.2, through analyses of the binding geometries, the dispersion contributions to the interaction energies, and the electronic charge distributions.

5.5 Discussion

We consider first site A, for which the binding energy shows the least variation between the five ZIF compounds. Figure 5.3 shows the configuration of the CO_2 molecule in this binding site for the example of ZIF-71. The molecule is positioned near the center of this site, allowing it to interact with all six nearby linkers. The closest neighbors to the CO_2 molecule are the carbon atoms at the 4 and 5 sites in the imidazole ring, which are located at a distance of 3.3 Å from an oxygen in CO_2 (the chlorine atoms are found at larger distances). This trend is similar for site A for the other four ZIFs as well: the CO_2 molecule in all cases is positioned such that its closest neighbors are within the imidazole rings, and such that its coordination with these neighbors is maximized. The relatively small variation in the binding energies in site A across the compounds is consistent with the similarity of the binding geometries, and the fact that the primary interactions (i.e., closest neighbor distances) are with the atoms in the imidazole ring, rather than the functional groups attached to these rings. An analysis of the electronic charge redistribution shows relatively little polarization of the neighboring framework atoms by the CO_2 molecule in site A (as

compared to sites B and C discussed below), such that the interactions are interpreted to be largely dispersive in nature. This interpretation is consistent with the fact that the binding energies calculated for the A site show the largest differences between the PBE and the vdW-DF method in Table 5.1, given that van der Waals contributions to non-bonded interactions are known to be significantly underestimated by PBE.

The binding energies in site B show the largest variation between the ZIF compounds. In contrast to site A, the CO_2 molecule is positioned most closely to the atoms in the functional groups on the linkers in site B. The binding geometries and the electronic charge density redistributions associated with site B are shown in Fig. 5.4. (The charge density redistributions plotted in Fig. 5.4 are defined as the difference between the self-consistent charge density with the CO_2 molecule present in the ZIF, and the sum of the charge densities of the ZIF compound and an isolated CO_2 molecule.) The closest neighbors to the atoms in the CO_2 molecule are all at distances of at least 2.7 Å, with the exception of ZIF-96, where the oxygen atoms in CO_2 are positioned 2.2 Å from the H atoms in the -NH_2 functional groups. The site-B binding geometry in ZIF-25 and ZIF-71 is influenced by the symmetric nature of the linkers, i.e., the fact that the functional groups on sites 4 and 5 are identical in these structures. This gives rise to a symmetric positioning of the CO_2 molecule relative to the functional groups. Dipole moments are induced on the functional groups pointing away from (towards) the positively (negatively) charged C (O) atoms of the CO_2 molecule. ZIF-93 and ZIF-97 show very similar binding geometries, which are characterized by a pronounced polarization of the CO_2 molecule. Both ZIF-93 and -97 feature asymmetric linkers that contain one -CH_3 functional group, which is seen to show minimal polarization. By contrast, polarization of the alternate functional group, -CHO in ZIF-93 and -CH_2OH in ZIF-97, is more pronounced and its proximity to the carbon in CO_2 is consistent with a favorable electrostatic interaction. In both ZIF-93 and ZIF-97 the center of mass position of the CO_2 molecule is shifted so that one of its oxygen atoms, with the larger induced electron density, is positioned away from the ring and towards the center of the pore. The binding geometry in ZIF-96 is seen to be much more complex, and features interactions between the -CN functional group nitrogen and the carbon atom in the CO_2 molecule at a distance of 3.2 Å, as well as between the oxygen atoms in the CO_2 and the hydrogen atoms in -NH_2 which form hydrogen bonds at a distance of 2.2 Å.

A representative binding geometry for site C is shown in Fig. 5.5, for the case of ZIF-96. This site features a positioning of the CO_2 molecule such that it is located near the hydrogen atoms attached to the 2-site carbon atoms on four linkers, and near one of the two functional groups on four other linkers; in the ZIF structures with asymmetric linkers the four neighboring functional groups are two of each type. Thus, the binding geometry in this site shows a behavior intermediate between sites A and B, where the primary interactions are with the imidazole and functional group atoms, respectively. For all of the ZIF compounds except ZIF-97, the closest neighbor distances are between the oxygen atoms in CO_2 and the hydrogen atoms on the 2-site of the imidazole ring: these neighboring atoms feature bond lengths of 2.45 Å in ZIF-96 and ZIF-71, 2.32 Å in ZIF-93 and 2.68 Å in ZIF-25. The magnitude of the binding energy is largest in the asymmetrically functionalized ZIF-93 and ZIF-96 structures. In these structures the positively charged carbon atom in CO_2 is positioned close to the negatively charged atoms in the functional

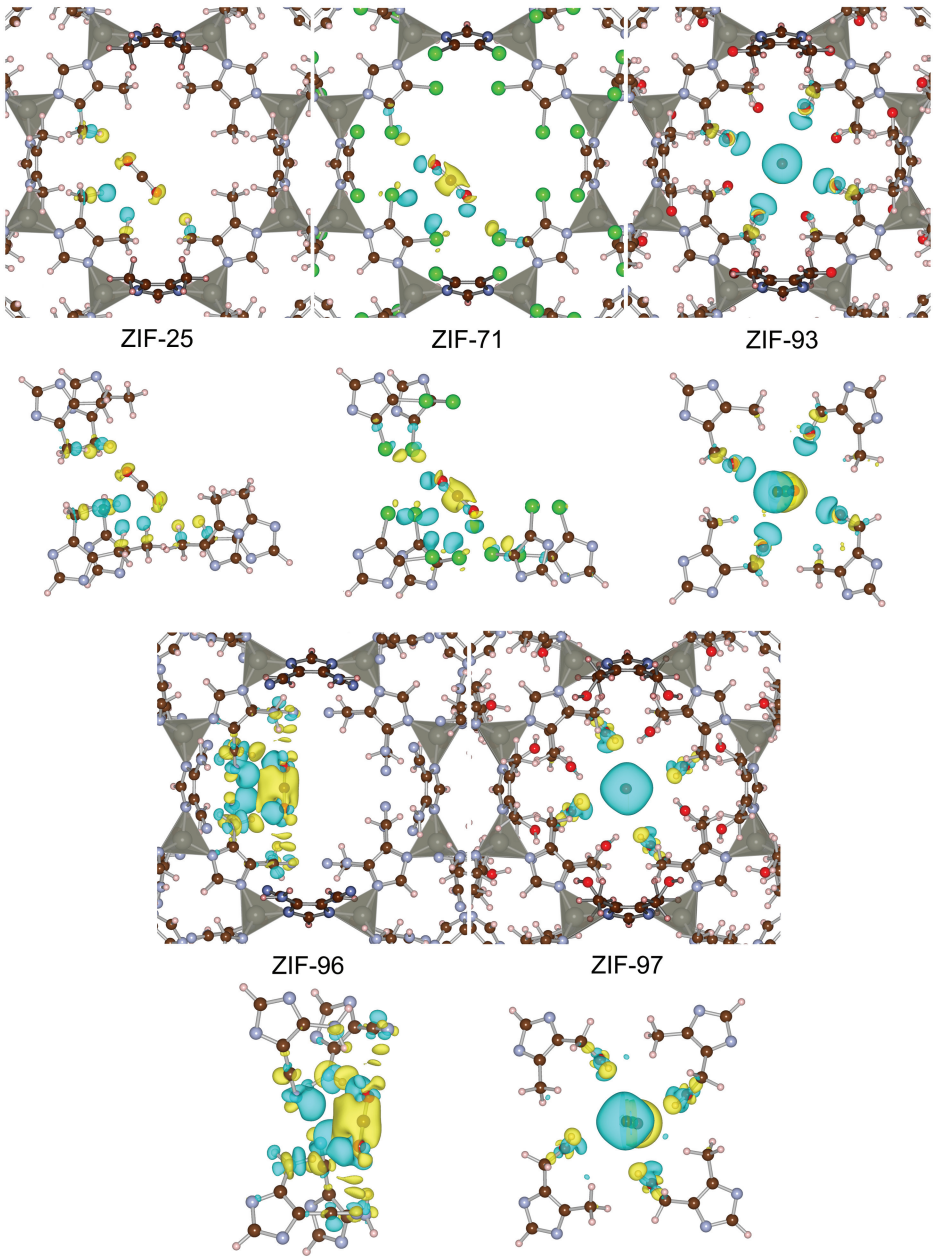

Figure 5.4: Charge redistribution induced by the presence of the CO_2 molecule in binding site *B* for ZIF-25, 71, 93, 96, and 97. In the upper panels the entire framework is shown. In the lower panels only the neighboring linkers that display significant polarization are shown. The yellow and blue isosurfaces denote a charge density of -.002 e/Å^3 and +.002 e/Å^3 respectively, where e is negative, indicating regions which lost and gained electrons. Purple spheres are nitrogen, red are oxygen, brown are carbon, green are chlorine, light rose are hydrogen, and the grey tetrahedra are centered on the zinc atoms.

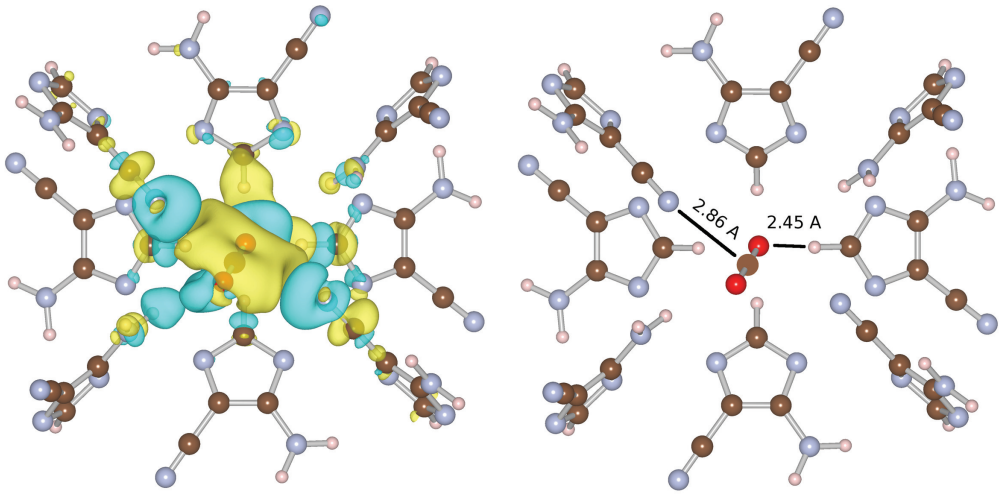

Figure 5.5: The position of the CO_2 in binding site C of ZIF-96 is shown in relation to the nearest **cyamIm** imidazole linkers. The charge density redistribution is plotted using the same thresholds as in Fig. 5.4 and relevant C-N and O-H distances are indicated in Å.

groups. Specifically the CO_2 carbon is located at a distance of 2.9 Å from the oxygen atom in the -CHO group in ZIF-93, and 2.8 Å from the nitrogen atom in the -CN group in ZIF-96. The weakest binding energy for site C is found for ZIF-97. In this structure the CO_2 molecule is found to be positioned further out into the pore, relative to the other compounds, minimizing the types of interactions with the linker atoms described above for ZIF-93 and ZIF-96. This may reflect steric hindrance caused by the large size of the -CH_2OH groups in ZIF-97.

We turn finally to an analysis of the role of the non-local-correlation (*nlc*) contribution to the binding energies calculated in the vdW-DF formalism. This contribution underlies the large differences between the PBE and vdW-DF results listed in Table 5.1, and the variations in this term across the ZIFs can be used as a measure of the variations in the strength of the dispersion interactions underlying CO_2 binding with the framework atoms. The *nlc* contribution to the binding energy is defined by the double integral given in Eq. (2), which reduces to the asymptotic $1/R^6$ form at large distances.[46] The magnitudes of the *nlc* contributions to the binding energies are given in parentheses next to the total values in Table 5.2. In general, this contribution is seen to be large, with magnitudes that are comparable to or even larger than the total binding energy. The value of the *nlc* energy contribution varies by only 0.032 eV in the A site across the five ZIF compounds. By contrast, in the B and C sites this contribution shows much larger variations of 0.125 eV and 0.250 eV, respectively.

Focusing on site B, the trends in the values of the *nlc* contribution to the binding energy across the ZIFs can be rationalized by interpreting this term as being dominated by the dispersion interactions between the CO_2 and the functional groups on the linkers. The dispersion interactions between two atoms or molecules can be approximated through the

generalized Casimir-Polder formula [27, 149, 121]:

$$E_{AB}^{disp} \approx -\frac{C_6}{R^6}, \tag{5.3}$$

$$C_6 = \frac{3}{\pi}\int_0^\infty \alpha^A(iw)\alpha^B(iw)dw, \tag{5.4}$$

where R is the intermolecular distance and α is the frequency-dependent dipole polarizability. Due to the rapid decay of this energy with respect to distance, and the nature of the binding geometries of the B site discussed above, the largest dispersion interactions are expected to be between the CO_2 molecule and the atoms in the closest neighboring functional groups. Thus, the coordination and polarizability of these groups are expected to be the key factors governing the magnitude of the dispersion interactions in this site. We define the coordination in site B by the number of functional groups at a distance less than 3.5 Å from the CO_2 molecule. The coordination number for the binding geometries in ZIF-25, 71, and 96 is 8, while in ZIF-93 and ZIF-97 it is 4. Thus, we expect the dispersion interactions to be larger in the former three ZIFs assuming similar polarizabilities. However, the -CH_3 groups in ZIF-25 have a smaller polarizability than the functional groups for the other ZIFs with the CO_2 sharing the same coordination, namely, the -Cl atom in ZIF-71 and the -NH_2 and -CN groups in ZIF-96. Thus, the total contribution from dispersion interactions should be relatively smaller in ZIF-25. With this reasoning we can rationalize the trend:

$$E_{96}^{disp}, E_{71}^{disp} > E_{25}^{disp}, E_{93}^{disp}, E_{97}^{disp} \tag{5.5}$$

shown for the *nlc* contribution in the B site in Table 5.2.

5.6 Summary and Conclusions

The formalism of the vdW-DF has been used to compute the binding energies of CO_2 in five ZIF compounds featuring the same zeolite-**rho** topology, but different functionalizations of the imidazole linkers. A comparison of the vdW-DF results with similar calculations performed using PBE highlights the important role of the non-local correlation energy in governing the binding energies in these systems, and points to the significance of the dispersive contributions to the interactions between CO_2 and framework atoms in these compounds.

Results are presented for the three dominant binding sites labeled A, B and C in Figs. 5.1 and 5.2. Site A shows the least variation in the calculated binding energies across the different compounds, consistent with a binding geometry featuring shortest neighbor distances between CO_2 and the atoms in the imidazole ring. Site B displays the largest variation in binding energies, consistent with binding geometries featuring dominant interactions between the CO_2 molecule and the atoms in the functional groups attached to the linkers. In site C the binding is intermediate in behavior, featuring comparable neighbor distances between CO_2 and atoms in both the imidazole ring and the functional groups.

From an analysis of the bond lengths, electronic charge redistribution, and contributions from non-local correlation energy, we conclude that CO_2 binding in the ZIF

compounds studied in this work is governed by a combination of electrostatic, dispersive and hydrogen-bonding interactions. The vdW-DF calculations suggest that these contributions work in a delicate balance to produce a variety of binding behavior that can be optimized through changes in the functionalization of the linker molecules, and that should be sensitive to changes in the framework topology as well.

Chapter 6

Binding Energy Landscape Analyses

The work presented in this chapter includes analyses of *the binding energy landscape* in two sets of ZIFs, one set is examined to show the effect of framework topology on CO_2 uptake and the other is examined to show the effect of chemical functionalization on CH_4 uptake. These data consist of potential energies of a guest gas molecule on a fine 3 dimensional grid in real space in the free volume of a ZIF, as calculated using classical Coulomb and Lennard-Jones potentials. The landscapes provide information on the binding site location, accessibility, depth, and width. Furthermore, they can be correlated with gas molecule density maps generated with grand canonical Monte Carlo (GCMC).

6.1 Forward

Section 6.2.3, Figure 6.2, and Table 6.1 were published by W. Morris, N. He, K. G. Ray, P. Klonowski, H. Furukawa, I. N. Daniels, Y. A. Houndonougbo, M. Asta, O. M. Yaghi, and B. B. Laird., in J. Phys. Chem. C, 116(45), 2408424090 (2012)[155], and is reproduced here with permission of the co-authors and publishers.

Section 6.3.3, Figure 6.3, and Table 6.2 were published by Y. A. Houndonougbo, C. Signer, N. He, W. Morris, H. Furukawa, K. G. Ray, D. L. Olmsted, M. D. Asta, B. B. Laird, and O. M. Yaghi., in J. Phys. Chem. C[80], and is reproduced here with permission of the co-authors and publishers.

Ning He, Brian Laird, and Yao Houndonougbo provided and tested the OPLS and UFF parameters for the classical force field calculations. David Olmsted assisted with the configuration of LAMMPS and the automation necessary for the binding energy landscape calculations. Colin Ophus helped with some of the initial potential energy landscape plots and Jessica Burton assisted with some of the LAMMPS calculations and plotting. Mark Asta, Brian Laird, and David Olmsted provided useful discussion and feedback. Yao Houndonougbo performed the GCMC simulations that produced the CH_4 density maps in Figure 6.3(b).

Table 6.1: Structural parameters for ZIF-7, 11, 93, and 94 from Ref. [155]

ZIF	functionalization (Im sites 4 & 5)	topology	density (g cm^{-3})	pore volume (cm^3 g^{-1})	pore diameter (Å)
-7	benzene	**sod**	1.24	0.207	7.5
-11	benzene	**rho**	1.02	0.457	14.9
-93	-CHO and $-CH_3$	**rho**	0.99	0.464	17.9
-94	-CHO and $-CH_3$	**sod**	1.32	0.229	9.1

6.2 The Effect of Framework Topology

6.2.1 Introduction

ZIFs can be synthesized in a variety of network topologies, which affects material density and surface area, as well as pore connectivity, morphology, and size. These structural properties can have significant effects on gas uptake, and therefore it is desirable to examine ZIFs which differ only in their topology in order to isolate the effect of variations in topology. Such materials are presented by Morris et al. in Ref. [155]: ZIF-93 and ZIF-94 both have the same functionalizations on the imidazole ring, but form in the **rho** and sodalite (**sod**) topologies respectively, and ZIF-11 and ZIF-7 share a different set of functionalizations, and also form in the **rho** and **sod** topologies respectively. In these systems the effect of network topology on CO_2 uptake was investigated with volumetrically measured adsorption isotherms, up to pressures of 55 bar, GCMC simulated isotherms and adsorbed gas molecule densities, and an analysis of the CO_2 binding energy landscape in each ZIF.

The ZIF-7, 11, 93, and 94 structures are shown in Figure 6.1 and structural parameters are presented in Table 6.1. For the compounds studied here, the **sod** topology ZIFs have smaller pore diameters and volumes, as well as higher densities, when compared to **rho** topology ZIFs. With regard to the functionalizations of these materials, ZIF-93 and 94 have one -CHO and one $-CH_3$ group on each imidazole ring while ZIF-7 and ZIF-11 have the two adjacent carbon atoms on the imidazole ring (sites 4 and 5) shared with a benzene ring (benzimidazole).

Experimental adsorption isotherms at 298 K for these four ZIFs from Ref. [155] show a larger CO_2 uptake in the **sod** topology ZIFs than the **rho** topology ZIFs at low pressure. At high enough pressure, this trend is reversed and the **rho** topology ZIFs show higher uptakes, with the crossover occurring between 2 and 5 bar for ZIF-7 and ZIF-11 as well as ZIF-94 and ZIF-93. The GCMC simulations from Ref. [155] reproduced the experimental adsorption isotherms from experiment well, with the exception of ZIF-7 at intermediate pressures. This discrepancy is due to a structural change[3, 4] that occurs in ZIF-7 with loading and therefore a step is observed in the uptake vs. pressure. CO_2 density maps were given that showed that the majority of the adsorbed CO_2 at low pressure is confined to the binding sites, discussed below, of both the **sod** and **rho** ZIFs, however, at high pressure, CO_2 is found in the GCMC simulations on more of the interior surfaces in the **rho** ZIFs while adsorption is still found mostly in the strongly binding sites in the **sod** ZIFs. In the following, we use the binding energy landscapes calculated for these materials to show the difference between the binding sites in the sodalite and rho topologies and how

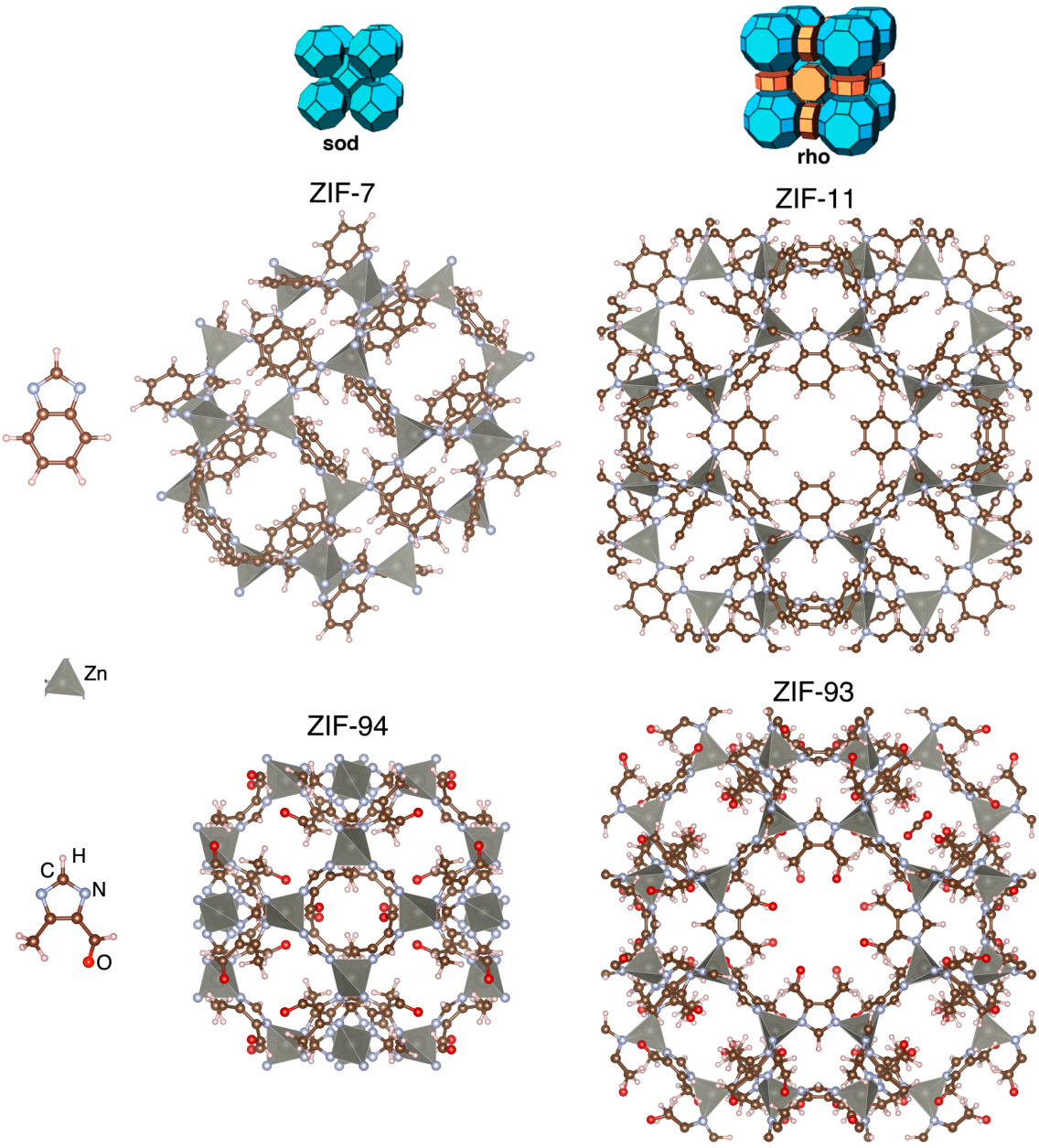

Figure 6.1: ZIF-7, 11, 93, and 94 with the shared **sod** and **rho** topologies and chemical functionalizations highlighted.

those differences affect carbon dioxide uptake at different pressures.

6.2.2 Methods

Energies shown in Figure 6.2 were computed using the Large-scale Atomic/Molecular Massively Parallel Simulator (LAMMPS)[177], a molecular dynamics code. This software was used to run a series of static calculations on a grid of points within the unit cell in order to map the binding energy landscape. These grids are 128×128×128 for the cubic cell of the **rho** topology ZIF-93 and ZIF-11, and 132×132×132 for the cubic unit cell of the **sod** topology ZIF-94 and the rhombohedral unit cell of **sod** topology ZIF-7. Structural symmetries are exploited so fewer actual calculations are performed. At each grid point the energy was calculated for 61 orientations of the CO_2 molecule and the minimum energy resulting from these calculations is plotted as a function of the center-of-mass position of the molecule below. For these calculations we used Lennard-Jones(L-J) and Coulomb potentials to model the gas-framework interaction. These are the same interactions and parameterizations included in the GCMC simulations mentioned in the introduction.

The pairwise interaction energy can be expressed as

$$U_{AB} = 4\epsilon_{AB}\left[\left(\frac{\sigma_{AB}}{r_{AB}}\right)^{12} - \left(\frac{\sigma_{AB}}{r_{AB}}\right)^{6}\right] + \frac{Q_A Q_B}{r_{AB}} \tag{6.1}$$

where ϵ_{AB} is the L-J interaction strength, σ_{AB} is the L-J range, r_{AB} is the distance between atom A and B, and $Q_{A(B)}$ is the charge on atom A(B). The first term in Equation 6.1 is the L-J 12-6 potential and the second term is the Coulomb interaction. The Lorentz-Berthelot mixing rules[144, 21] give ϵ_{AB} and σ_{AB} in terms of the parameters for interactions between identical atoms. That is,

$$\epsilon_{AB} = \sqrt{\epsilon_{AA}\epsilon_{BB}} \tag{6.2}$$

and

$$\sigma_{AB} = \frac{\sigma_{AA} + \sigma_{BB}}{2}. \tag{6.3}$$

So, for every atom (A), three parameters are needed: ϵ_{AA}, σ_{AA}, and Q_A.

The L-J parameters for the framework were chosen from the universal force field (UFF)[184] and optimized potentials for liquid simulations (OPLS)[96] force field sets. The framework charges are derived using the REPEAT algorithm[26], which fits these charges in such a way as to reproduce the electrostatic potential, calculated with DFT, in open regions of the framework. The periodic DFT calculations were performed using the PBE GGA exchange correlation functional[170] and the PAW method[22] in VASP[112, 113, 110, 111]. The L-J parameters and charges for the CO_2 come from the elementary physical model 2 (EPM2) of Harris and Young[69].

6.2.3 Results and Discussion

To supplement the experimental and GCMC data reviewed in the introduction, in order to better understand the role of topology in the gas adsorption performance of ZIF-7, -11, -93, and -94, we have analyzed the CO_2 binding energy landscapes for each framework.

The results are shown in Figure 6.2, which plots the binding energy, minimized over 61 CO_2 orientations, as a function of the CO_2 center of mass position. These results facilitate an analysis of the important binding sites, including the magnitude of the binding energy, the size and shape of the potential-energy wells, and the accessibility of the binding sites.

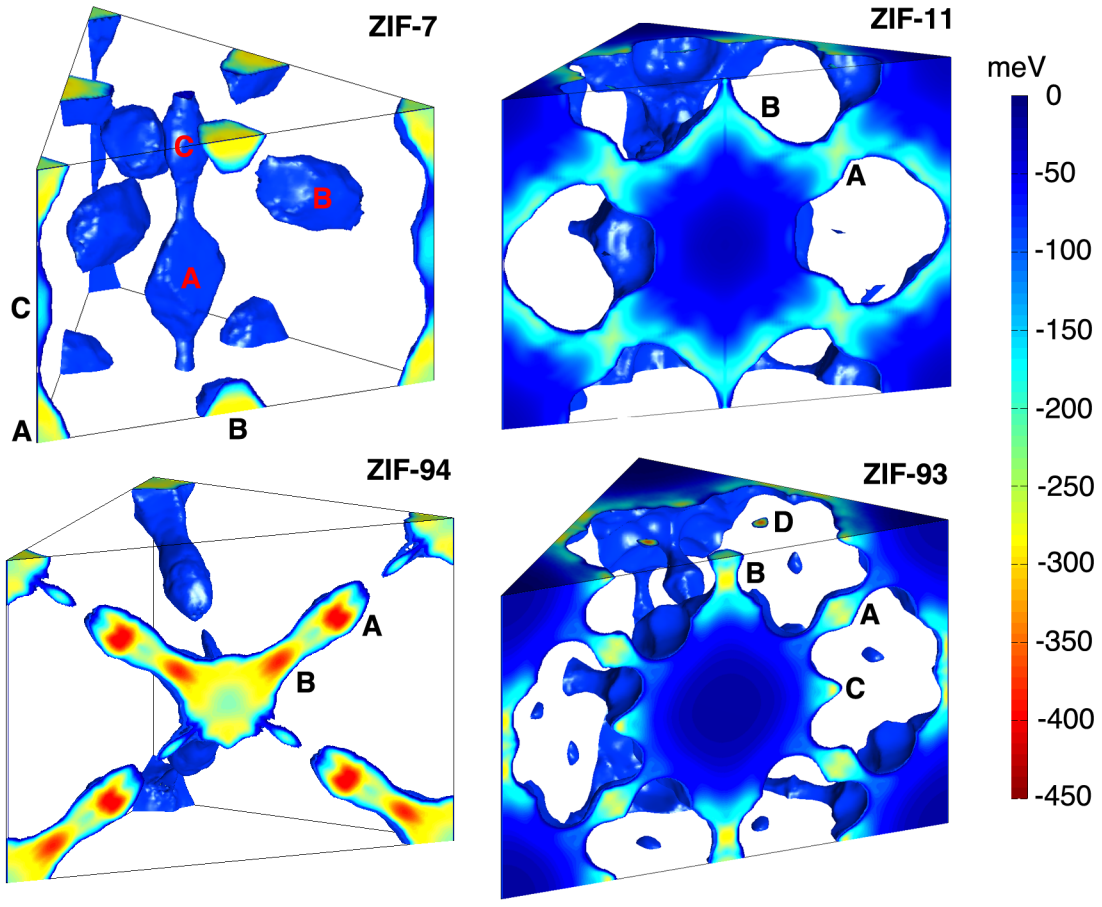

Figure 6.2: Diagonal {110} slices through the cubic unit cells of ZIF-11, -94, and -93, and the rhombohedral unit cell of ZIF-7 showing the binding energy of CO_2 minimized versus orientation and plotted by center of mass position. Important binding regions are indicated by capital letters (A, B, C, and D), referred to in the discussion in the text.

There are three distinct binding sites in ZIF-7, which we will call A, B, and C. Binding site A, located within a ring of six zinc atoms, has a binding energy of -307 meV. Site B, located within a distorted ring of six zinc atoms, has a binding energy of -330 meV. Site C, located in the center of the truncated octahedron (Scheme 1) and surrounded by imidazolate linkers, has a binding energy of -148 meV. These binding sites are relatively localized compared to the sites found in the rho topology ZIFs discussed below. The classical potentials used in this study produce a CO_2 transport barrier from the A site to the C site of roughly 410 meV and from the B site to the C site of roughly 530 meV. This first barrier represents transport through the vertical channel shown in the center and vertical

edges of the ZIF-7 polyhedral section in Figure 6.2, and the second barrier corresponds to interchannel transport. Transport through the channel is mentioned in previous studies on the gate-opening mechanism in ZIF-7[2, 62].

The primary binding in ZIF-11 occurs in two regions, herein referred to as A and B. The A site is situated within a ring of six zincs and six imidazolate linkers and has a binding energy of -233 meV. Binding region B occurs on the inner surface of the largest pore, near the ring of eight zincs at a binding energy of -283 meV. This geometry differs from previously reported rho ZIFs[156, 185], including ZIF-93, described below, where binding occurs within the ring of eight zincs. Both binding regions in ZIF-11 are broad and open onto the large Linde Type A (lta) cavity facilitating multiple occupancies at each site at high pressure. Both binding sites are accessible from this cavity due to a lack of a high energy barrier. Pore-to-pore transport should be possible through the six-ring channel, passing through site A, with a barrier of roughly 190 meV.

Binding in ZIF-94 occurs within a ring of six zincs, which we denote site A, and additionally in the same channel as A, but closer to the center of the pore and surrounded by the functional groups on the linkers, which we denote site B. These sites have binding energies of -421 and -392 meV respectively. Binding site A is surrounded by the framework atoms, and binding site B opens to a pore that is relatively small compared with the rho-topology ZIFs. Both of these sites are accessible from the pore; however, the CO_2 must pass through the B site to get the A site, which involves a $\sim$155 meV barrier. Between pores, a larger barrier of $\sim$520 meV in one direction and $\sim$380 meV in the other are encountered.

ZIF-93 contains four important binding sites: A, B, C, and D. Site A is within a ring of six zincs, as with ZIF-11. Site B is within the ring of eight zincs, instead of on the surface of the lta cavity as in ZIF-11, most likely due to the smaller functional groups in ZIF-93, which allow CO_2 to fit in this channel. Site C is on the inner surface of the lta cavity in the 110 direction from the center of this cavity. Site D, represented by ellipsoidal sections in Figure 4, lies between four zincs and four imidazolate linkers and is accessible from site B. The binding energies are -262, -290, -276, and -390 meV, respectively. Binding sites A, B, and C open to the large lta cavity. Binding energies in these sites are weaker than those in ZIF-94, but there is more room for additional CO_2 molecules on the inner surface of the pore. Interpore transport appears possible along the channel through the ring of eight zincs as well as the channel through the ring of six zincs.

The binding energy landscapes provide data on the primary binding sites in the four ZIFs considered in this work. The positions and relative strengths of the binding sites identified are consistent with the results given by GCMC density maps in Ref. [155]. CO_2 is more strongly bound in the binding sites found in sod-topology ZIF-7 and ZIF-94, relative to those in the corresponding rho-topology ZIF-11 and ZIF-93. However, the sites in the rho ZIFs open to the large lta cavity with a correspondingly large surface area for additional gas adsorption outside of the deepest wells. Transport barriers determined through classical potentials provide information on binding site accessibility; however, the framework is fixed in these calculations and flexibility in the imidazolate linkers is expected to reduce these barriers.

The trends in the binding energies calculated for the four ZIFs considered in this work can be rationalized as follows, based on an analysis of the electrostatic versus van

der Waals contributions to the classical potential models. In Ref. [156], it is argued that ZIFs with asymmetrically functionalized imidazolate linkers (that is, having two different functional groups attached to the imidazole ring) tend to produce stronger electrostatic contributions to the CO_2 binding energy. This trend is consistent with the larger average Coulomb contribution to the binding sites in asymmetrically functionalized ZIF-94 (-104 meV) compared to ZIF-7 (-70 meV). However, this is not the case for the rho ZIFs considered, because the asymmetrically functionalized ZIF-93 has a smaller average Coulomb contribution (-59 meV), compared to ZIF-11 (-92 meV), which suggests that local binding geometry can influence the importance of the electrostatic energy for a particular site. The van der Waals forces favor a large framework surface area close enough to the CO_2 to maximize the attractive contribution to the Lennard-Jones interactions. This contribution favors the small pores in **sod** ZIF-7 and ZIF-94 when compared to the **rho**-structured ZIF-11 and ZIF-93, which is reflected in the average Lennard-Jones energy, which is -196 and -302 meV compared to -164 and -259 meV, respectively.

6.2.4 Conclusion

From an analysis of the binding energy landscape we find that the binding sites of the **sod** topology ZIF-7 and ZIF-94 bind CO_2 more strongly than those found in the **rho** topology ZIF-11 and ZIF-93. However, the binding sites in the **rho** topology ZIFs open onto the large LTA pores, supporting multiple occupancy with the extra volume available. In addition, the high surface areas of these ZIFs provide more room for weaker binding. Thus, at high pressure the **rho** topology ZIFs have higher CO_2 uptakes while at low pressure the **sod** topology ZIFs have higher uptakes. By examining the L-J and Coulomb contributions to the binding energy separately we are able to show how confined binding sites enhance the van der Waals binding strength by enabling the gas molecule to interact with a large nearby surface area and how asymmetric ZIF functionalizations can enhance the electrostatic interaction in some cases.

6.3 Methane Binding in an Isoreticular set of Rho Topology ZIFs

6.3.1 Introduction

ZIFs are interesting for potential applications in natural gas separations and storage. To better tailor materials for this purpose, an understanding of the effect of ZIF chemical functionalization on the adsorption of CH_4 is essential. Although this effect was investigated for the binding of CO_2 in ZIF-25, 71, 93, 96, and 97, as discussed in Chapter 5 as well as Refs. [185] and [156], the behavior of CH_4 should be distinct due to its vanishing electric dipole and quadrupole moments. For the same set of ZIFs as used for the CO_2 studies mentioned in Chapter 5, Houndonougbo et al., in Ref. [80], reported experimental methane adsorption isotherms at several temperatures and up to 1 bar pressure and GCMC simulations up to 80 bar. These ZIFs all share the same zeolite **rho** topology, but differ in the way in which functional groups are attached to the imidazole ring. For more detail on these materials see Section 5.4.

Houndonougbo et al. found that the CH_4 uptake was largely proportional to the ZIF Brunauer-Emmett-Teller (BET) surface area. This trend differs from CO_2, where instead, adsorption is enhanced in the asymmetrically functionalized frameworks [185, 156]. Methane isosteric heats of adsorption, Q_{st}, were calculated up to 1 bar from experimental adsorption isotherms using a virial-type expansion[41, 91, 51]. The same quantities were calculated for pressures up to 80 bar from GCMC simulations using the virial-type expansion as well as fluctuations in the total energy of the simulated system[201]. Q_{st} was found to initially decrease with pressure and loading, but at adsorbed amounts higher than 2.6 to 4.6 mmol CH_4/g, depending on the ZIF, Q_{st} increased due to CH_4-CH_4 interactions. In the following we analyze the binding energy landscape encountered by methane in the set of **rho** topology ZIFs examined in Ref. [80], as well as the CH_4 occupations as calculated with GCMC. With these data, we discuss the primary methane binding locations and the uptake as a function of pressure.

Table 6.2: Maximum CH_4 binding energies by binding site in meV. Site A refers to the six-membered ring window of the α-cavity, site B refers to the center of the connecting double 8-rings, and site C refers to the inner surface of the pore along the $\langle 110 \rangle$ direction, as discussed in the text. From Ref. [80]

	Binding Energy		
ZIF	Site A	Site B	Site C
25	-255	-167	-193
71	-207	-149	-119
93	-222	-194	-121
96	-207	-155	-65
97	-220	-190	-109

6.3.2 Methods

Similar to the method described in section 6.2.2, the binding energies shown in Figure 6.3 were computed using LAMMPS[177]. A 256×256×256 grid of CH_4 positions is used for ZIF-25, 71, 93, 96, and 97 and structural symmetries are exploited so fewer actual calculations are performed. Coulomb interactions are neglected since the methane molecule has an electric octupole as its lowest non-zero moment. L-J potentials are utilized with Lorentz-Berthelot mixing rules. ZIF L-J parameters were chosen from the Optimized Potentials for Liquid Simulations - All Atom (OPLS-AA) set[96, 97], except for the zinc atom parameters, which come from the UFF set [184]. CH_4 is treated as a united atom at the carbon position using the Transferable Potentials for Phase Equilibria - United-Atom (TraPPE-UA) force field[203].

6.3.3 Results and Discussion

To examine the main adsorption sites for methane in the **rho** ZIFs considered in this work, we have computed the binding energy as a function of the center of mass (COM) position of a CH_4 molecule. In Figure 6.3(a) the results are presented by contour plots

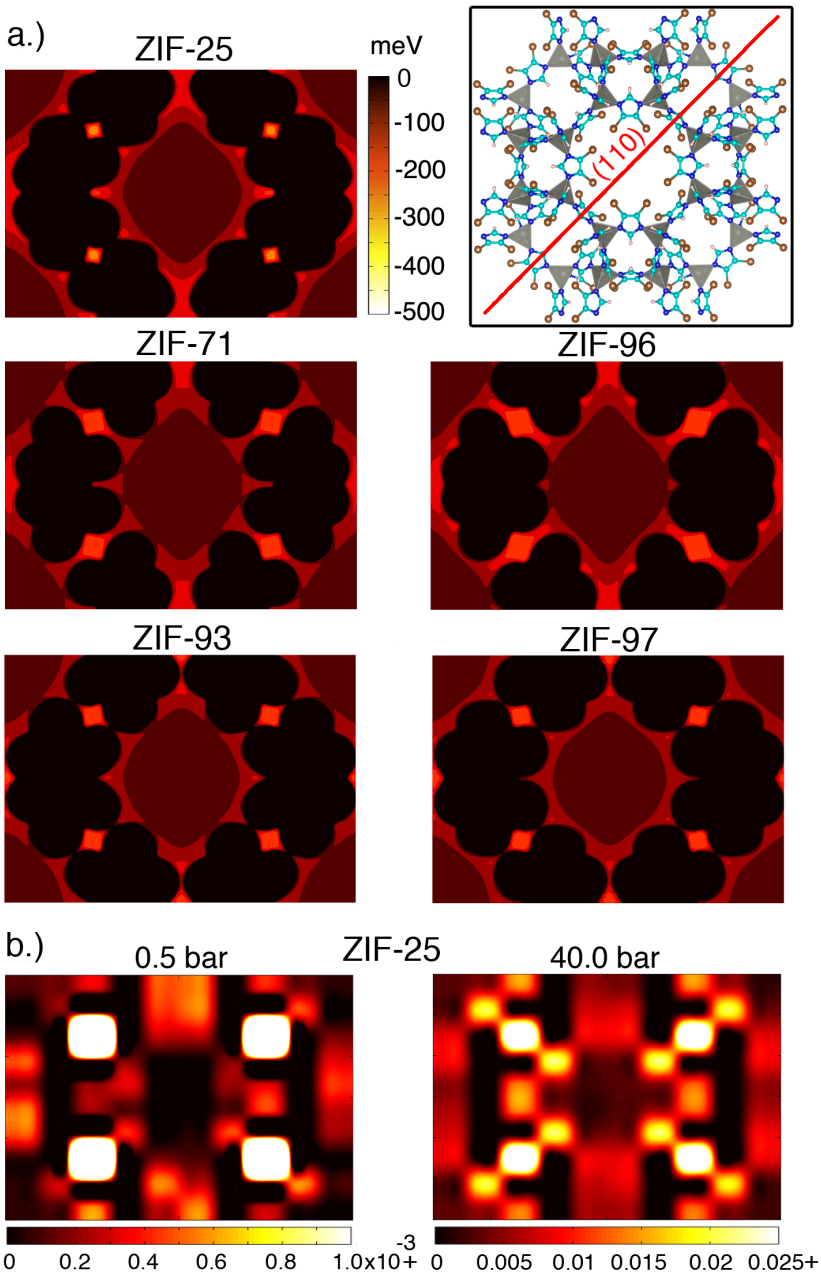

Figure 6.3: (a) Methane binding energy as a function of position in the (110) plane in meV. (b) Methane density maps in the (110) plane of ZIF-25 for 0.514 bar and 40.0 bar in number of molecules per Å^3. Inset: ZIF-71 viewed along the [001] direction. The projection of the (110) plane in which the binding-energy and density maps are plotted is shown by the red line. This plane cuts through the center of the main pore in the **rho** structure.

in a slice through the structure corresponding to a (110) plane through the middle of the α-cavity, the empty volume in the center of the **rho** topology ZIF cubic cell. This cubic cell is presented in the top right of Figure 6.3. Similar to the analysis for CO_2 adsorption in Ref. [185], we identify three sets of binding sites: one between the ZIF linkers in the six-membered ring window of the α-cavity, another in the center of the connecting double 8-rings, and a final set on the inner surface of the α pore (along the $\langle 110 \rangle$ direction, as well as in the entrance to the six-membered ring window). The maximum binding energies in each of these sites are listed in Table 6.2. We find that the binding site confined to the six-membered ring window features the strongest binding in each of the ZIFs considered in this work, indicating that this site should dominate adsorption in the dilute limit.

We have further computed the COM of CH_4 probability distribution directly from the GCMC simulations. The two-dimensional distributions at 298 K are plotted in Figure 6.3(b) for low (0.514 bar) and moderate (40.0 bar) pressures. These data are consistent with the three adsorption sites described above and illustrated in Figure 6.3(a). A slice along the (110) plane of the CH_4 density in ZIF-25 at low and high pressure, Figure 6.3(b), shows that the largest methane density is found near areas shown to have strong binding in Figure 6.3(a). At low pressure CH_4 molecules are primarily adsorbed between the ZIF linkers in the six-membered ring window of the α cavities, consistent with the binding energy results. A comparatively small methane population is also present in the center of the connecting double 8-rings. With increasing pressure, methane continues populating these two sites and distributes throughout the connecting double 8-rings. In addition, the inner surfaces of the cavities begin to host larger methane concentrations, both in the $\langle 110 \rangle$ direction as well as at the entrance to the six-membered ring window. At high pressure, these sites continue to carry an increasing proportion of the methane load. Specifically, when increasing the pressure from 0.514 bar to 40.0 bar the densities in the six-ring site increase by roughly a factor of 5, the density in the 8-rings by a factor of 18, and the density on the inner surface of the pore by a factor of 52.

With increasing pressure, there is a shift in the fraction of the adsorbed methane at the different sites: at low pressure the majority of the adsorbed methane resides in the small-volume/high-binding-energy sites, while at high pressures more methane is found in the more weakly bound sites that are open to empty space within the pores.

6.3.4 Conclusion

The six-membered ring window site is calculated to have the strongest methane binding in the **rho** topology ZIFs considered. GCMC simulations show adsorbed CH_4 densities at low pressure that are consistent with this result. At higher pressure, binding in the center of the connecting double 8-rings and on the inner surface of the pore increases.

Chapter 7

Origins of CH_4/CO_2 Adsorption Selectivity in Zeolitic Imidazolate Frameworks: A van der Waals Density Functional Study

The energetics of methane binding are calculated in a set of five zeolitic imidazolate framework (ZIF) materials using the van der Waals Density Functional 2 (vdW-DF2)[128]. These results are compared to previous calculations for carbon dioxide in the same ZIFs[185] (See Chapter 5) to examine the roles of electrostatic interactions, polarization, molecule size, and hydrogen bonding in determining the CO_2/CH_4 adsorption selectivity. To isolate the effect of the chemical functionalization of the imidazolate linkers, the ZIFs considered share the same zeolite RHO topology and metal atom (Zn). Methane is found to be primarily bound by dispersion forces and ZIF binding site geometry and steric constraints have the greatest influence on its binding. These results are in contrast to carbon dioxide where electrostatic interactions play a sizeable role. To quantify the relative importance of dispersion forces versus electrostatic contributions to the binding energies, we isolate these different contributions through an approach combining an analysis of the non-local contributions to the exchange-correlation energy, and a decomposition of the charge density based on Bader analysis.

7.1 Forward

The work presented in this chapter was submitted by K. G. Ray, D. Olmsted, Y. Houndonougbo, B. B. Laird and M. Asta, to J. Phys. Chem. C[186], and is reproduced here with permission of the co-authors.

For this chapter Mark Asta, Brian Laird, and David Olmsted provided useful discussion and feedback.

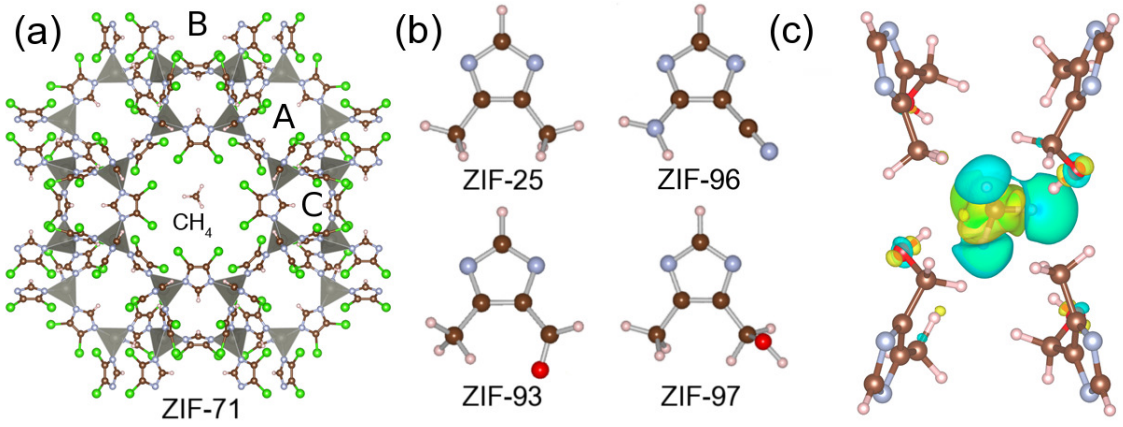

Figure 7.1: (a) ZIF–71 cubic cell, CH_4 in binding site B, sites A, B, and C labeled (b) ZIF–25, –93, –96, and –97 linkers (c) CH_4 in ZIF–97 B site showing induced charge density.

7.2 Introduction

Zeolitic Imidazolate Frameworks (ZIFs) are crystalline nanoporous network materials formed by tetrahedrally coordinated transition metal atoms bridged by organic imidazolate linkers. The bridging bonds in these linkers have a 145° angle, identical to the Si-O-Si bond found in zeolites; consequently, ZIFs are observed to form network topologies homeomorphic to those found in zeolites[166, 84]. A great variety of ZIFs have been already synthesized, involving different metal atoms, network topologies, and chemical functionalizations of the imidazolate linker[13]. Thus a large parameter space exists for the optimization of the properties of ZIFs for applications such as gas separation or storage. In particular, ZIFs have received considerable attention for application to separations in gas mixtures involving methane, for the upgrading of natural gas[132, 208, 8]. For such applications the adsorption selectivity of CH_4 relative to other gas species, such as CO_2, is a property of fundamental interest[204, 29, 10].

Methane adsorption and selectivity in ZIFs have been studied both experimentally [214, 172, 70, 12, 141] and computationally[10, 208, 172, 17, 129, 137] for pure gases and gas mixtures relevant in the context of natural-gas separations. Experimental studies in ZIFs have involved measurements of adsorption isotherms[214, 172, 70], breakthrough[70], and membrane selectivity[12]. The understanding derived from these studies has been complemented by relevant investigations in other related MOF systems[15, 52, 187, 75, 230, 199, 14, 44, 157, 45], featuring data on the time-resolved uptake of methane and carbon dioxide[14], as well as neutron scattering to find CH_4 and CO_2 binding sites and occupations[224, 221]. The studies of ZIFs have shown that these frameworks can exhibit adsorption selectivities and uptakes that exceed the performance of commercial adsorbents used for natural gas separation[75, 15] and that the performance depends on several factors, including the choice of linker, functionalization, pore size, and metal ion[52, 172, 214, 187, 75, 230, 199].

The understanding derived from experimental investigations has been supple-

mented with computational studies employing a variety of methods, from Grand Canonical Monte Carlo (GCMC) and Molecular Dynamics (MD)[137, 172, 17, 227, 208, 219, 228, 226, 158, 99, 129, 10, 83, 34] simulations based on classical force fields, to studies of binding energetics and geometries based on density functional theory (DFT), coupled cluster, and second order Møller-Plesset perturbation theory (MP2) [187, 34, 196, 176]. GCMC simulated adsorption isotherms have reproduced experimentally measured trends in adsorption selectivity in several ZIFs. For separations involving CO_2 and CH_4 mixtures, in particular, gas selectivity in these materials is often attributed to stronger CO_2 electrostatic interactions[10, 172, 228, 219, 227, 226, 158, 129, 187], specifically with an ionic framework[10], the linker[158, 172], or polarizable functionalities[187, 158], depending on the system.

In the current study we examine in detail the origin of the selective binding of CO_2 relative to CH_4 in five ZIFs, namely, ZIF–25, –71, –93, –96, and –97[156]. These ZIFs share the same zeolite RHO topology, but differ in the types of functional groups attached to the linker, allowing us to explore the effects of chemical functionalization on the relative binding energies of CH_4 and CO_2. This work builds on recent studies by Houndonougbo et al. [80] involving experimental measurements and GCMC simulation calculations of adsorption isotherms for CH_4 in this same set of ZIFs, as well as calculations of CO_2/CH_4 adsorption selectivities using the ideal adsorbed solution theory (IAST)[182]. In Ref. [80] it was found that the CH_4 adsorption per unit surface area was relatively constant with respect to ZIF functionalization, while previous investigations on CO_2[156] in this set of ZIFs showed an increase of adsorption per unit surface area in those frameworks that featured two different functional groups on the same imidazole ring. In these ZIFs with asymmetric-functionalities it was concluded that CO_2 interacts more strongly with the linkers through electrostatic interactions, which enhances the selectivity relative to CH_4.

To understand in further detail the role of electrostatic and dispersion contributions to the selective binding of CO_2 relative to CH_4, we employ in the current work calculations based on the van der Waals Density Functional 2 (vdW-DF2) approach. We begin by presenting vdW-DF2 calculations of binding energies for CH_4 in the ZIFs under consideration. The results are compared with our previous calculations of CO_2 binding energies[185] in the same systems with the same functional[128] to highlight the energetic origins of adsorption selectivity. The binding-energy results are complemented by an analysis of the relative importance of dispersion versus electrostatic and polarization contributions to the binding energies. For this purpose, we quantify the relative magnitudes of these different contributions through an approach combining an analysis of the non-local contributions to the exchange-correlation energy and a decomposition of the charge density based on Bader analysis[206, 197, 72]. This analysis includes an estimate of the contributions to the binding energy resulting from the static polarizability of the gas molecule and functional groups. Such information can be useful for guiding the development of classical force fields for classical simulations and complements previous related studies undertaken with symmetry adapted perturbation theory (SAPT)[150, 151, 229].

7.3 Materials and Methods

Our aim is to elucidate the variations in CO_2/CH_4 binding selectivity resulting from changes in the functional group in a series of isoreticular ZIFs. We first use the results of the classical simulations reported in Ref. [80] to identify the important binding sites. Next, we relax the gas molecule position and orientation using the vdW-DF2 and separate the contribution to the binding energy due to dispersion from the non-local contribution to the correlation energy. Finally, we utilize a method of estimating the individual contributions to the electrostatic interactions due to static charge distributions, and induced polarization, to analyze trends in these contributions across functional groups.

7.3.1 ZIF Structures

We focus on a set of RHO topology ZIFs, each of which have a different set of functional groups on the 4 and 5 sites of the imidazole ring. With the exception of these functional group differences and a resultant 1.5% variation in lattice constants, the structures are identical[156]. The chemical functionalities, depicted in Fig. 7.1, are as follows: two -CH_3 groups (ZIF–25), two -Cl atoms (ZIF–71), one -CHO and one -CH_3 group (ZIF–93), one -CN and one -NH_2 group (ZIF–96), and one -CH_2OH and one -CH_3 group (ZIF–97). The latter three ZIFs: –93, –96 and –97, each have two different functional groups on each imidazole linker.

7.3.2 van der Waals Density Functional Calculations

The most favorable binding sites obtained from the classical force field calculations reported in Ref. [80] are used to develop initial geometries for input into the first-principles calculations based on the vdW-DF2 method[128], as was done in our previous work on CO_2[185]. In the vdW-DF2 method the exchange correlation energy is divided into a semilocal exchange energy, a local correlation energy, and a nonlocal correlation energy.

$$E_{xc} = E_x + E_{lc} + E_{nlc} \tag{7.1}$$

where E_x is a semi-local exchange functional (taken from the PW86 parameterization[168] in the vdW-DF2 method), E_{lc} is a local correlation energy that is given by the local density approximation, and E_{nlc} is the non-local contribution to the correlation energy, which can be written as

$$E_{nlc} = \frac{1}{2}\int d\mathbf{r}d\mathbf{r}' n(\mathbf{r})\phi(\mathbf{r},\mathbf{r}')n(\mathbf{r}'). \tag{7.2}$$

In Equation 7.2, the kernel, ϕ, is a function of both $\mathbf{r}$ and $\mathbf{r}'$ through a dependence on the electron densities ($n(\mathbf{r})$) at $\mathbf{r}$ and $\mathbf{r}'$. E_{nlc} is derived from the adiabatic connection fluctuation dissipation theorem through a series of approximations including an expression for the dielectric response based on the plasmon pole model[46]. The vdW-DF2 differs from the original vdW-DF of Dion et al.[46] in that it uses a different exchange functional and a changed parameter in E_{nlc} representing a limit more appropriate for molecular interactions. It is worth noting that related functionals have been proposed involving different exchange functionals and have been shown to yield accurate results[102]. We choose the vdW-DF2

because it yields more accurate binding energies and distances than the vdW-DF[128], but still has no fitted parameters and therefore may be more transferable than other methods which introduce fitting to a particular reference dataset.

The vdW-DF class of methods has been previously applied to the calculation of binding energies, binding geometries, and vibrational frequencies of CO_2 in metal organic frameworks and ZIFs[185, 180, 179, 159, 119] as well as $(H_2)_4CH_4$, C_2H_6, C_3H_8, and C_4H_{10} in MOFs[133, 160]. To the best of the authors' knowledge the vdW-DF method has not been used previously for calculations of methane binding energies in MOFs or ZIFs. Because we are concerned with non-bonded interactions between the framework and guest CH_4 molecule, which has an octupole as its lowest non-vanishing electric multipole, the dispersion interaction is expected to be of primary importance, such that use of the vdW-DF formalism is viewed to be essential for computing realistic binding energies within the formalism of DFT.

vdW-DF2 calculations have been performed with the Vienna Ab Initio Simulation Package (VASP)[112, 113, 110, 111] using the projector-augmented wave (PAW) method[22, 114] with Perdew-Burke-Ernzerhof (PBE)[170] based potentials from the VASP library. The vdW-DF, as implemented in VASP, uses the efficient numerical algorithm for evaluating E_{nlc} due to Roman-Perez and Soler[188]. The electronic wavefunctions are expanded in a plane-wave basis set with a cutoff energy of 400 eV and only a single (Γ) k-point is used in the Brillouin-zone sampling due to the large size of the primitive unit cell. Forces on CO_2 and CH_4 molecules are relaxed to 0.01 eV/Å and the atoms in the framework are held fixed at the experimentally-determined positions[156] to reduce the computational cost. From representative calculations performed with full relaxations, it is expected that the fixing of the ZIF atom positions produces an error of less than 15 meV in the binding sites considered below. Binding energies are estimated to be converged to better than 3 meV with respect to the plane-wave cutoff energy, number of k-points, and the density of the real-space grid used to represent the charge density.

In what follows, we will estimate the dispersion contribution to the binding energy by comparing E_{nlc} in the combined gas molecule-ZIF system with the sum of the values for the isolated gas molecule and isolated ZIF. That is,

$$E_{nlc}^{bind} = E_{nlc}^{gas-ZIF} - E_{nlc}^{gas} - E_{nlc}^{\mathrm{ZIF}} \tag{7.3}$$

where E_{nlc}^{bind} is the contribution to the binding energy from the non-local correlation and $E_{nlc}^{gas-ZIF}$, E_{nlc}^{gas}, and E_{nlc}^{ZIF} are the non-local correlation energies of the combined ZIF-gas molecule system, the isolated gas molecule, and the isolated ZIF, respectively. The value of E_{nlc}^{bind} has been shown to depend largely on the low electron density regions surrounding the two bonded components[20]. Although in the asymptotic limit E_{nlc}^{bind} represents the dispersion energy and has the usual r^{-6} dependence[46], when there is a significant overlap of charge, there can be other contributions to E_{nlc}^{bind}. For the non-bonded gas molecule-ZIF interactions considered in the current work, we expect small electron density overlap between the gas molecule and the framework atoms. This is consistent with equating E_{nlc}^{bind} defined in Eq. (7.3) with the contribution to the binding energy arising from dispersion interactions.

7.3.3 Electrostatic Induction Energy Calculations

Strong electrostatic framework-gas molecule interactions suggest that charge redistribution may be important to binding and highly polarizable functional groups have been associated with high CO_2/CH_4 adsorption selectivity in previous work[187]. Static charge redistribution, i.e., electrostatic induction, can occur in the gas molecule due to the electrostatic potential of the ZIF and vice versa. To compute the contributions to the binding energy due to this polarization effect we employ the following approach.

To first order in the induced charge, the contribution to the gas-framework binding energy due to charge polarization can be obtained by considering the energy of the induced charge density in the ZIF in the electric potential of the gas molecule (E_{ind}^{ZIF}) and the induced charge density on the gas molecule in the electrostatic potential of the ZIF (E_{ind}^{gas}). This induction term has been previously calculated using SAPT for CO_2 in several ZIFs[150, 151]. The contribution from this energy was found to be less than 10 meV for the ZIFs considered[151]. We note, however, that this result was obtained for ZIFs which did not display the type of asymmetric functionalization which the work in Ref. [156] suggests will feature stronger electrostatic interactions. Further, the work in Ref. [151] presented induction energies averaged over several binding geometries, and the contribution could be larger for specific binding sites. We thus consider the importance of this contribution in further detail in the current work for the ZIFs described above, three of which feature asymmetrically functionalized linkers.

To leading order in the induced charge densities, the contribution of electrostatic induction (i.e., induced static polarization) to the binding energy can be written as:

$$E_{ind}^{total} = E_{ind}^{\mathrm{ZIF}} + E_{ind}^{gas} \tag{7.4}$$

where the two terms on the right-hand side are defined as:

$$E_{ind}^{gas} = \int d\mathbf{r} \rho_{ind}^{gas}(\mathbf{r}) \Phi^{\mathrm{ZIF}}(\mathbf{r}) \tag{7.5}$$

and

$$E_{ind}^{\mathrm{ZIF}} = \int d\mathbf{r} \rho_{ind}^{\mathrm{ZIF}}(\mathbf{r}) \Phi^{gas}(\mathbf{r}) \tag{7.6}$$

In Eq. (7.5), ρ_{ind}^{gas} is the difference in the charge distribution of the gas molecule when bound to the ZIF relative to when it is an isolated molecule, and Φ^{ZIF} is the electrostatic potential associated with an isolated ZIF. Similarly, $\rho_{ind}^{\mathrm{ZIF}}$ is the induced charge density in the ZIF, and Φ_{gas} denotes the electrostatic potential of an isolated gas molecule.

In the current work we obtain ρ_{ind}^{gas} by first determining a volume associated with the gas molecule using Bader analysis[206, 197, 72] applied to the charge density calculated for the combined ZIF-gas system. This choice of volume is non-unique and to some extent, arbitrary. However, because we are looking at only the induced difference in charge density, and the electron density is small in the region midway between the gas molecule and the neighboring ZIF functional groups (i.e., the interactions are non-bonded in nature), our results are relatively insensitive to changes in the exact shape of the volume provided it is not enlarged to include charge density from neighboring molecules or functional groups. We

extract the electron density in this volume and call it $\rho^{gas}_{combined}$. We also perform calculations on the isolated ZIF and isolated gas systems in the same binding geometry (but with the gas molecule at its isolated equilibrium geometry, unbent and unstretched) and sum their charge densities. This is the charge density without any induction, from which we extract the same Bader volume and call the result $\rho^{gas}_{summed\ isolated}$. We then define

$$\rho^{gas}_{ind} = \rho^{gas}_{combined} - \rho^{gas}_{summed\ isolated}. \tag{7.7}$$

The induced charge density $\rho^{\mathrm{ZIF}}_{ind}$ is defined similarly using the volume outside of the gas molecule Bader volume. It should be noted that the procedure described above includes the deformation of the gas molecule, but not of the ZIF functional groups, which remain frozen at their experimentally determined positions in the calculations.

In addition, we calculate the monopole and dipole moments of the induced charge density of the gas molecule as:

$$\Delta q^{gas}_{monopole} = \int d\mathbf{r}\rho^{gas}_{ind}(\mathbf{r}) \tag{7.8}$$

and

$$\Delta\mu^{gas}_{dipole} = || \int d\mathbf{r}[\mathbf{r}\rho^{gas}_{ind}(\mathbf{r})]||_2 \tag{7.9}$$

where $||\mathbf{x}||_2$ is the Euclidean norm of $\mathbf{x}$. We find $\Delta q^{gas}_{monopole}$ to be quite small, less than .016 e, although nonzero, which means that $\Delta\mu^{gas}_{dipole}$ would be origin dependent. To remedy this, the Bader volumes could be slightly expanded or contracted to be made neutral, however, in practice we rescale the negative charge, which is equivalent to changing the volume if the new choice of volume does not change the center of negative charge. With this modification our definition of $\Delta\mu^{gas}_{dipole}$ is independent of origin.

We also calculate the change in monopole and dipole moments of the ZIF functional group nearest to the gas molecule. As described above for the gas molecule, our definition of the change in dipole moment is made independent of origin by rescaling the negative charge associated with the functional group. Included in the Bader volume associated with the functional group are the nearest carbon and nitrogen atoms on the imidazole ring so that we do not exaggerate the changes in the monopole and dipole with charge transfer between the ring and functional group. The relevant definitions for these quantities are:

$$\Delta q^{FunctGrp}_{monopole} = \int d\mathbf{r}\rho^{FunctGrp}_{ind}(\mathbf{r}) \tag{7.10}$$

and

$$\Delta\mu^{FunctGrp}_{dipole} = || \int d\mathbf{r}[\mathbf{r}\rho^{FunctGrp}_{ind}(\mathbf{r})]||_2. \tag{7.11}$$

7.3.4 Binding Energy Decomposition

In the previous sections, we have described methods to evaluate the portion of the binding energy due to dispersion, E^{bind}_{nlc}, and electrostatic induction, E^{total}_{ind}, giving us the following decomposition.

$$E^{bind}_{total} = E^{bind}_{nlc} + E^{total}_{ind} + E^{bind}_{other}. \tag{7.12}$$

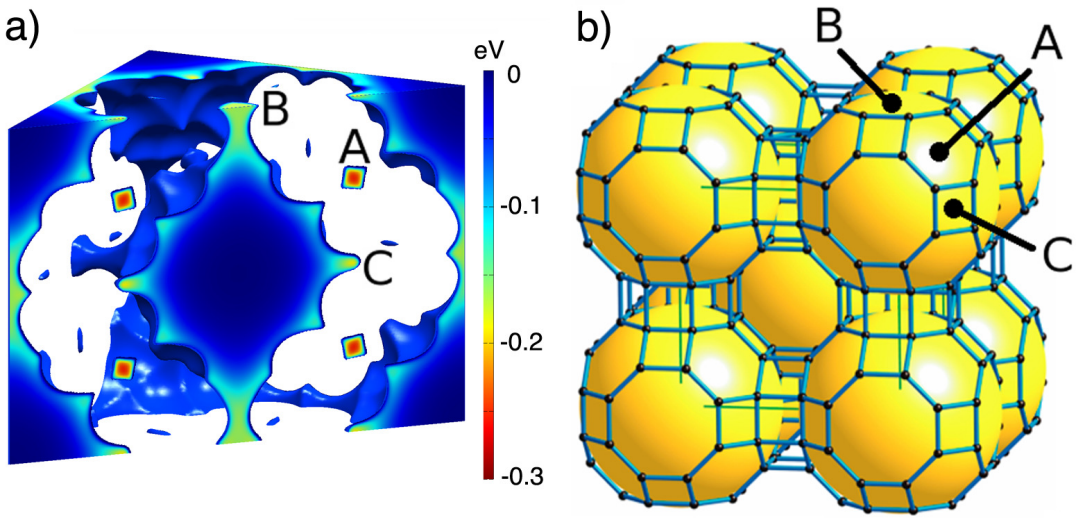

Figure 7.2: a) CH_4 binding energy landscape on a {100} slice of the cubic unit cell of ZIF–25 calculated using Lennard-Jones potentials. b) RHO topology net of the ZIFs considered in this work with important binding sites A, B, and C labeled.

In this decomposition, $E_{other}^{binding}$ contains contributions from the electrostatic interaction between the unperturbed gas molecule and ZIF charge distributions, exchange repulsion, higher order contributions from electrostatic induction, and the correlation energy associated with the local density approximation.

7.4 Results and Discussion

7.4.1 Calculated Binding Energies

In Chapter 6, Lennard-Jones potentials with parameterizations optimized for CH_4 were used to calculate binding energy landscapes for CH_4 in the five RHO ZIFs described in Section 7.3.1. We summarize here the results presented in Ref. [80] to define the positions of the binding sites that will be discussed in the context of the vdW-DF2 calculations below. A binding energy landscape calculated with classical force fields is shown in Fig. 7.2(a) for the representative case of ZIF–25. Labeled on Fig. 7.2 (a) and (b) are the positions of three primary binding sites: A, B, and C, which are common to each of the five RHO ZIFs considered in this work. Sites A and B are each located in a different channel between Linde Type A (LTA) cavities of the RHO topology ZIFs. Binding site A is within a ring of six Zn atoms and six imidazolate linkers in channels along $< 111 >$ crystallographic directions and B is within a ring of eight zinc atoms and eight imidazolate linkers in channels along $< 100 >$ directions. Site C is located on the surface of the LTA pore, along $< 110 >$ directions from the center of the pore. These framework locations correspond to the positions of the primary sites for CO_2 binding in the same ZIFs, as identified by classical force fields and reported in Ref. [185].

Binding energies taken from vdW-DF2 calculations for CH_4 and CO_2 in the three

Table 7.1: CH_4 and CO_2 binding energies, E_{total}^{bind}, calculated with the vdW-DF2 method, as well as the contribution of the non-local correlation to the binding energy, E_{nlc}^{bind}, are tabulated in units of meV. CO_2 values are taken from Ref. [185].

		CH_4			CO_2		
Site	ZIF	E_{total}^{bind}	E_{nlc}^{bind}	E_{total}^{bind}-E_{nlc}^{bind}	E_{total}^{bind}	E_{nlc}^{bind}	E_{total}^{bind}-E_{nlc}^{bind}
A	25	-374	-426	52	-419	-437	18
	71	-343	-382	38	-413	-469	56
	93	-364	-396	32	-373	-465	92
	96	-309	-359	50	-376	-444	68
	97	-395	-449	54	-460	-465	5
B	25	-201	-222	21	-235	-275	41
	71	-223	-254	31	-323	-367	44
	93	-258	-286	29	-408	-282	-126
	96	-238	-259	21	-385	-393	8
	97	-330	-337	7	-464	-268	-196
C	25	-277	-365	89	-319	-430	110
	71	-266	-372	106	-310	-393	84
	93	-192	-278	86	-433	-469	37
	96	-96	-145	48	-434	-449	16
	97	-220	-249	30	-250	-219	-31

binding sites of ZIF–25, –71, –93, –96, and –97 are presented in Table 7.1. The results for CH_4 were obtained in the present work, while those for CO_2 are taken from Ref. [185]. In every instance the binding for CO_2 is stronger than that for CH_4, showing a universal selectivity in these materials for carbon dioxide over methane. The selectivity in binding energy ranges from a negligible 9 meV in site A of ZIF–93 to 338 meV in site C in ZIF–96. The calculated results are qualitatively consistent with the trends in adsorption reported in Ref. [80], based on IAST calculations employing measured single-component adsorption isotherms. Specifically, the IAST results give the following CO_2/CH_4 adsorption selectivities at 1 bar and 298 K: ZIF–96: 10.2, ZIF–93: 8.2, ZIF–97: 6.1, ZIF–71: 2.7, and ZIF–25: 2.5. If we order the ZIFs using the difference in the CO_2 and CH_4 calculated binding energies averaged across all of the binding sites, using the calculated results in Table 7.1, we obtain the same ranking (positive numbers indicate stronger CO_2 average binding): ZIF–96: 184 meV, ZIF–93: 133 meV, ZIF–97: 76 meV, ZIF–71: 70 meV, ZIF–25: 40 meV.

7.4.2 Dispersion Contributions

In Table 7.1, the nonlocal correlation contributions to the binding energy, E_{nlc}^{bind}, are representative of the magnitude of the dispersion contributions to the binding energies. In site A this energy varies with respect to ZIF functionalization by 90 meV for CH_4 and 32 meV for CO_2. In this site the gas molecule is surrounded by a ring of six linkers, and is in closest proximity with the atoms in the imidazole ring rather than those in the functional groups, as illustrated in Fig. 7.1(a).

In site B, E_{nlc}^{bind} varies by 115 meV for CH_4 and 125 meV for CO_2. As illustrated

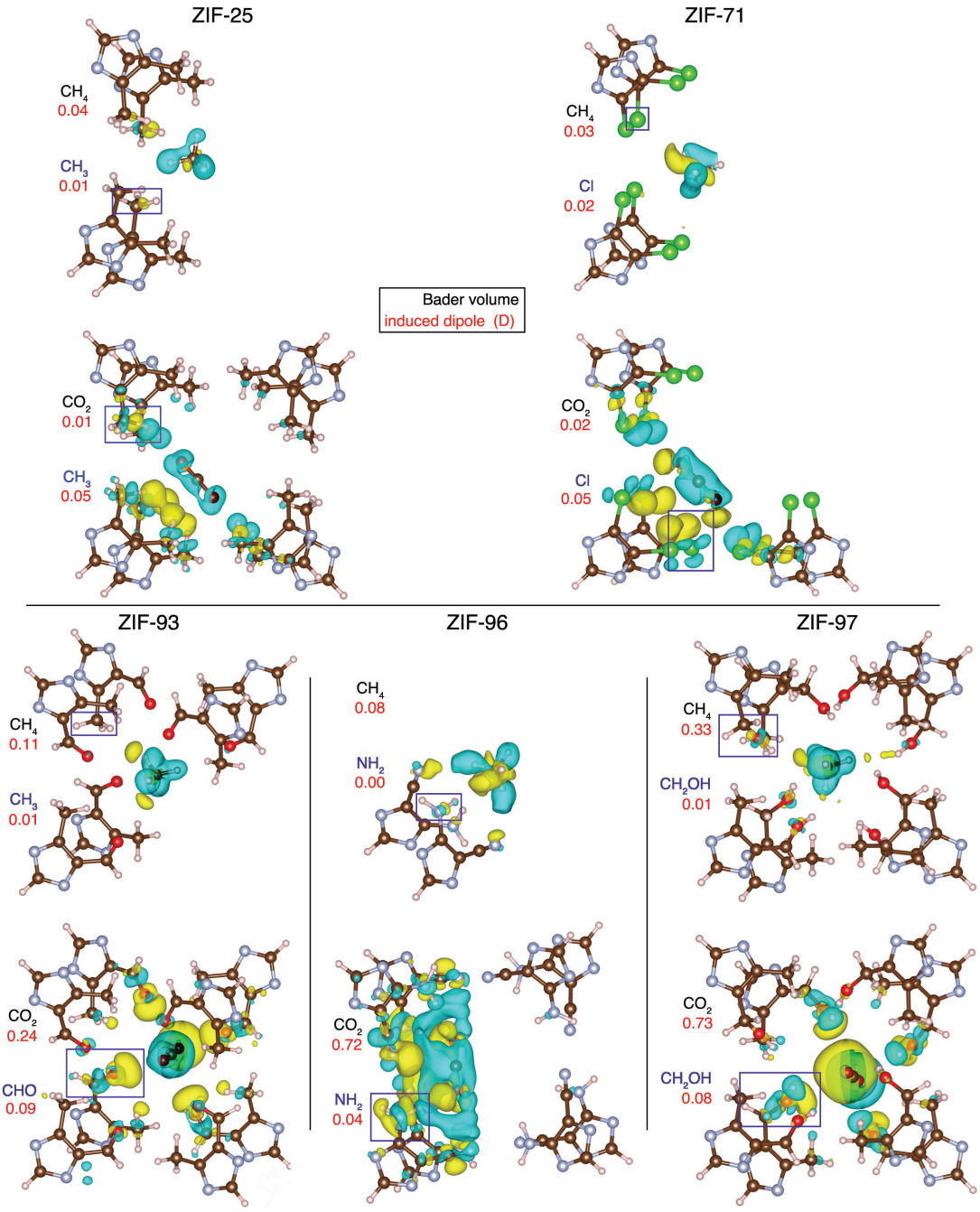

Figure 7.3: Site B for ZIF–25, –71, –93, –96, and –97 with CH_4 and CO_2. Induced polarizations due to gas molecule - framework interactions are given by yellow (blue) isosurfaces showing electron accumulation (depletion) at a density of 0.001 e $Å^{-3}$. For each gas molecule and nearest functional group, boxed in blue, the magnitude of the induced dipole moment of the associated Bader volumes are listed in units of D.

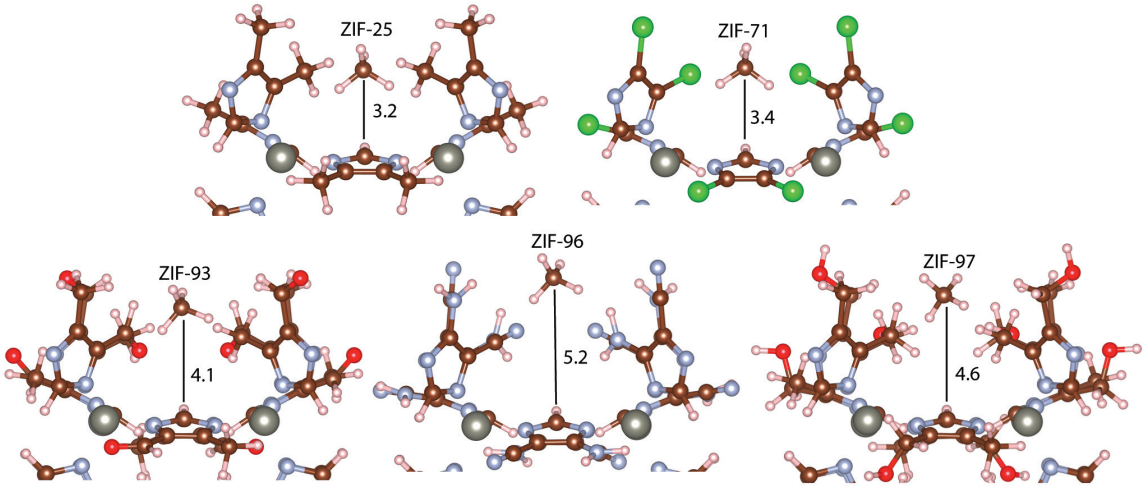

Figure 7.4: CH_4 in site C for the ZIFs considered. CH_4 carbon to framework hydrogen distances are given in Å, highlighting steric constraints.

in Fig. 7.3, the gas molecule in site B is located closer to the functional groups attached to the imidazole ring than the rings themselves or the metal ions, consistent with the larger variation in the calculated binding energies across the ZIFs. In this geometry, the variation in E_{nlc}^{bind} may be roughly attributed to the number of nearby functional groups and their effective frequency dependent polarizability[209]. In site B, the CO_2 dispersion energies do not follow the same trend as CH_4, because CO_2 has different binding orientations and positions in this site, depending on the host ZIF, as shown in Fig. 7.3. These differing CO_2 binding geometries have varying numbers of nearby framework atoms, so E_{nlc}^{bind}, which depends strongly on the local coordination to members of the framework, will also vary[185]. In contrast, the number of nearby functional groups to CH_4 in site B is the same in each ZIF (although only the functional groups that have an induced charge density greater than 0.001 eÅ^{-3} are shown in Fig. 7.3).

Site C is cup shaped with the sides defined by four functional groups and the bottom defined by four hydrogen atoms, each bound to the carbon atom positioned directly between two nitrogens in an imidazole ring. As illustrated in Fig. 7.4, larger functional groups force methane to bind further away from the center of the site. A larger binding distance results in a smaller E_{nlc}^{bind} and the variation in the distance is responsible for the large variation in E_{nlc}^{bind} in this site across the ZIFs considered: 227 meV for CH_4 and 250 meV for CO_2, respectively. This cup geometry can enhance selectivity because the binding energy of CH_4 is observed to be reduced by steric constraints in ZIF–93, –96, and –97, while there is only a hindrance in ZIF–97 for the linear CO_2 molecule. In site C the binding energy for CH_4 (CO_2) in ZIF–93 and –96 is -192 (-433) meV and -96 (-434) meV respectively, showing a large influence on selectivity arising from steric constraints.

Table 7.2: For site B, the maximum change in the bond angle between neighboring CH bonds in CH_4 ($\Delta\angle_{\text{H-C-H}}$) and between CO bonds in CO_2 ($\Delta\angle_{\text{O-C-O}}$) are listed along with the respective greatest changes in bond length ($\Delta R_{\text{C-H}}$ and $\Delta R_{\text{C-O}}$). Also tabulated are the induced dipole moments of the Bader volumes associated with these molecules. Lastly, the energies associated with these electronic and ionic distortions in the field of the fixed ZIF are reported.

gas	ZIF	$\Delta\angle_{\text{H-C-H}}$ (°)	$\Delta R_{\text{C-H}}$ (Å)	$\Delta\mu^{gas}_{dipole}$ (D)	E^{gas}_{ind} (meV)
CH_4	25	0.14	0.002	0.04	-13
	71	0.18	0.002	0.03	-10
	93	0.43	0.002	0.11	-39
	96	0.43	0.002	0.08	-13
	97	0.45	0.002	0.33	-31
gas	ZIF	$\Delta\angle_{\text{O-C-O}}$ (°)	$\Delta R_{\text{C-O}}$ (Å)	$\Delta\mu^{gas}_{dipole}$ (D)	E^{gas}_{ind} (meV)
CO_2	25	0.11	0.001	0.01	-12
	71	0.33	0.001	0.02	-34
	93	0.06	0.002	0.24	-6
	96	1.70	0.000	0.72	-54
	97	0.05	0.009	0.73	-110

7.4.3 Electrostatic Contributions

We begin by examining the difference in E^{bind}_{total} and E^{bind}_{nlc} in order to analyze the non-dispersive contributions to binding energy that depend on the ZIF functionalization. These contributions include the electrostatic interactions between the charge distributions of the gas molecule and ZIF, as well as the exchange energy and local correlation energy associated with the induced polarization and (small) charge overlap.

As shown in Table 7.1, the trends in the difference E^{bind}_{total} - E^{bind}_{nlc} for CH_4 in ZIFs with distinct chemical functionalities differs from those of CO_2. For CH_4 in sites A and B, which do not show the pronounced steric constraints associated with site C, the variation in the magnitude of this energy difference is very small, only 22 meV for site A and 24 meV for site B. Thus in these sites, non-dispersive contributions to the binding energy are relatively insensitive to functional group identity. In contrast, the variations in E^{bind}_{total} - E^{bind}_{nlc} for CO_2 are 87 meV in site A and 240 meV in site B. Therefore non-dispersive interactions are important for CO_2 binding and in governing the selectivity of CO_2 over CH_4 in these materials. In site B of ZIF–93 and –97, non-dispersive contributions to the binding energy account for 155 and 203 meV of the difference in CH_4 and CO_2 binding energies, respectively.

Because the magnitudes of the energy difference E^{bind}_{total} - E^{bind}_{nlc} show large variations in site B across the ZIF series, we focus on this site to examine in more detail the factors contributing to this quantity. In what follows, we discuss the energy associated with induced charge polarization as defined in Eqs. (7.4-7.6), as well as the structural distortion of CH_4 and CO_2, and the changes in the gas molecule dipole moments.

The energy of electrostatic induction in the gas molecule due to the ZIF electrostatic potential, E^{gas}_{ind}, is given in Table 7.2 for CO_2 and CH_4 in site B. For CH_4, the values

Table 7.3: Data for the functional group in each ZIF closest to the guest gas molecule. The chemical formula, proximity, and change in dipole moments of this functional group are given, as well as the energy due to the total change in ZIF electron charge density in the electrostatic field of the gas molecule.

gas	ZIF	functional group	distance (Å)	$\Delta\mu_{dipole}^{FunctGrp}$ (D)	E_{ind}^{ZIF} (meV)
CH_4	25	CH_3	2.65	0.01	0
	71	Cl	3.22	0.02	0
	93	CH_3	2.76	0.01	0
	96	NH_2	2.68	0.00	0
	97	CH_2OH	2.53	0.01	0
CO_2	25	CH_3	2.88	0.05	-9
	71	Cl	3.42	0.05	-12
	93	CHO	3.23	0.09	-12
	96	NH_2	2.20	0.04	-17
	97	CH_2OH	2.72	0.08	-10

are, in general, smaller than for CO_2. The largest CH_4 induced polarization energies are found in the asymmetrically-functionalized ZIF–93 and –97 (-39 and -31 meV, respectively). Correspondingly, the induced gas dipole moments, $\Delta\mu_{dipole}^{gas}$, are also highest for CH_4 in –93 and –97 (0.11 and 0.33 D, respectively). However, in every ZIF considered, the distortions in CH_4 bond angles and lengths are relatively much smaller than the maximum found for CO_2. For CO_2, we see values of E_{ind}^{gas} as high as -54 and -110 meV in ZIF–96 and –97. The largest magnitudes of $\Delta\mu_{dipole}^{gas}$ for CO_2 are also obtained in these ZIFs, 0.72 D in ZIF–96 and 0.73 D in ZIF–97. The largest O-C-O bond angle and C-O bond length distortions are also found in ZIF–96 and –97, respectively.

For CH_4, the binding geometry in site B, as characterized by the center of mass and orientation of the molecule relative to the neighboring functional groups, is similar across the five different ZIFs. However, for CO_2, the variations in electrostatic induction energy, molecule distortion, and induced dipole moments in site B across the five ZIFs can be understood to be due to the differences in binding geometry illustrated in Fig. 7.3 and discussed previously in Ref. [185]. In ZIF–25 and –71 the CO_2 is bound in a position that is symmetrically oriented with respect to the two functional groups which are identical in these ZIF structures. By contrast, in ZIF–93, –97 and –96, which feature asymmetrically-functionalized linkers, the CO_2 molecule is asymmetrically oriented with respect to the two functional groups such that the positively-charged C atom in CO_2 is nearest the negatively charged O, N and O atoms in the functional groups in –93, –96 and –97, respectively. For –96 and –97, the O atom in the CO_2 is nearest hydrogen atoms in ZIF–96 and –97, at distances of 2.2 Å and 2.7 Å, respectively, that are indicative of hydrogen bonding[185]. The interactions between the gas and functional group atoms give rise to the bond stretching reported in Table 7.2 for –97 and the bond bending reported for –96.

In Table 7.3, the functional group nearest the gas molecule in the B-site is listed for both CH_4 and CO_2 in each of the five ZIFs. Also listed are the nearest-neighbor distances between the atoms in the gas molecule and neighboring functional groups, as well

Table 7.4: CH_4 and CO_2 vdW-DF2 binding energies in meV. E_{total}^{bind} is the total binding energy, E_{nlc}^{bind} is the dispersion contribution to the binding energy, E_{ind}^{total} is the contribution to the binding energy from electrostatic induction, and $E_{other}^{bind} = E_{total}^{bind} - E_{nlc}^{bind} - E_{ind}^{total}$.

gas	ZIF	E_{total}^{bind}	E_{nlc}^{bind}	E_{ind}^{total}	E_{other}^{bind}
CH_4	25	-201	-222	-13	34
	71	-223	-254	-10	41
	93	-258	-286	-39	68
	96	-238	-259	-13	34
	97	-330	-337	-31	38
CO_2	25	-235	-275	-22	62
	71	-323	-367	-46	90
	93	-408	-282	-18	-108
	96	-385	-393	-71	79
	97	-464	-268	-120	-76

as the induced dipole moment on the neighboring functional groups and the magnitude of the energy E_{ind}^{ZIF} defined in Eq. (7.6). The dipole moments on the neighboring functional groups are an order of magnitude larger for the case of CO_2 compared with CH_4, in qualitative agreement with expectations, given that the lowest-order non-vanishing electrostatic moment for CO_2 is that of a quadrupole, while it is an octupole for CH_4. Overall, however, the induced dipole moments on the functional groups in Table 7.3 are significantly smaller than those for the gas molecules in Table 7.2. Consistent with this finding, the values of E_{ind}^{ZIF} in Table 7.3 are significantly smaller in magnitude than E_{ind}^{gas}. The largest value the energy associated with induced polarizations in the ZIF is -17 meV, obtained for CO_2 in ZIF–96. For CH_4 in all ZIFs considered, this energy is zero within the precision of our calculations.

7.4.4 Binding Energy Decomposition

In Table 7.4 we list for CH_4 and CO_2 in site B the calculated values of the binding energy (E_{total}^{bind}), the values of E_{nlc}^{bind} which reflect the contribution of the dispersion interactions, and E_{ind}^{total} defined by Eqs. (7.4-7.6), which gives a measure of the contributions due to induced polarization. In the last column of Table 7.4 is listed the quantity $E_{other}^{bind} = E_{total}^{bind} - E_{ind}^{total} - E_{nlc}^{bind}$ which represents exchange, local correlation, higher order electrostatic interactions due to charge redistribution, and the electrostatic interaction between the unperturbed charge distributions of the ZIF and gas molecule. For CH_4 in site B we notice that E_{total}^{bind} runs between -201 and -337 meV while the quantity $E_{other}^{binding}$ varies by only 34 meV across the five ZIFs and E_{ind}^{total} varies by only 29 meV. These results highlight the dominant contribution of dispersion interactions for CH_4 binding in this site, as measured by E_{nlc}^{bind}.

For CO_2 in site B, E_{ind}^{total} varies between -18 and -120 meV, showing that this energy can be a significant portion of the total binding energy and that this contribution is selective with respect to the adsorbed gas molecule (i.e., the contribution is larger in magnitude for CO_2 than CH_4). As discussed in the previous paragraphs, the variation in

this quantity is due most likely to differences in the electrostatic interactions between the CO_2 and ZIF depending on chemical functionalities and their symmetry, as well as hydrogen bonding in ZIF–96 and –97. For CO_2, $E_{other}^{binding}$ has the values of 62, 90, and 79 meV in ZIF–25, –71, and –96, respectively, which are opposite in sign to the attractive values of -108 meV and -76 meV in ZIF–93 and –97, respectively. These differences are consistent with the expected variations in the electrostatic energy across these ZIFs. Specifically, in the symmetrically functionalized ZIF–25 and 71, CO_2 relaxes to a position maximizing the dispersion energy, as we can see with the larger value of E_{nlc}, and there are negligible electrostatic interactions between the unpolarized charge distributions. In ZIF–93 and –97, E_{nlc} is smaller, and instead electrostatic interactions with the framework are maximized by the position of the CO_2 and an attractive $E_{other}^{binding}$ is calculated. In ZIF–96, CO_2 has a large attractive induced polarization energy as well as a large E_{nlc}^{bind}.

The results of the partitioning of the binding energies into dispersion, electrostatic induction, and a combination of other contributions including electrostatic and exchange, are similar to what was reported by McDaniel et al.[150, 151] using SAPT. The non-local correlation energies for CH_4 and CO_2 in the five ZIFs considered here range from 58% to 117% of the total binding energies and the electrostatic induction energies correspond to 4.5% to 26% of the total binding energy. These results are consistent with those found for CO_2 in ZIF-8 and ZIF–71 in ref. [151], which shows a roughly 5% contribution from induction and a roughly 160% contribution from dispersion (although this is not a direct comparison since the numbers in that study are averages over many CO_2 positions and our results are for a particular binding site). Furthermore, in Ref. [150], SAPT derived potentials show that the ratio of dispersion energy to electrostatic energy is much higher for N_2 in several ZIFs than CO_2 in the same ZIFs. This could be due do to a smaller electrostatic energy associated with N_2, which has roughly one third the electric quadrupole moment of CO_2[55], as is suggested in their paper. The electrostatic interaction for CH_4 is found to be smaller than that for CO_2 in our work, as expected because CH_4 lacks electric quadrupole and lower moments.

7.5 Summary and Conclusion

In this work the vdW-DF2 formalism was used to compute the binding energies of CH_4 and CO_2 molecules in three different binding sites across five differently functionalized RHO topology ZIFs. These calculations show that ZIF–93 and ZIF–96 both bind CO_2 more strongly than CH_4 in site B and C by more than 147 meV and as high as 338 meV. The selectivity in binding site B is determined to originate from enhanced electrostatic interactions between asymmetrically-functionalized ZIFs and the electric quadrupole moment of the CO_2, as opposed to the higher-order octupole moment of the CH_4. Hydrogen binding with the CO_2 also occurs in ZIF–96 and –97. Site A is found to be comparatively non-selective to CO_2 versus CH_4 binding in all of the RHO ZIFs considered. The selectively in site C is determined to originate from steric constraints due to the geometry of the binding site and the different sizes of carbon dioxide and methane. For two of the ZIFs studied in this work (namely ZIF–96 and –97) the contribution to the binding energy due to polarization is calculated to be on the order of 20 to 25 % of the binding energy, and is thus

significant.

7.6 Appendix

Below we consider the approximations used in calculating the energy of the induced polarization of a gas molecule in the electrostatic potential produced by an unpolarized ZIF. The approximations include the frozen core approximation, the valence pseudocharge approximation, and the use of the CHGCAR file to determine Bader volumes. The CHGCAR file is a VASP output file containing the valence pseudocharge and compensation charges, as described below. In addition, an origin independent method of determining the induced dipole moment of a cluster of atoms is considered for the case of negligible charge transfer to and from the cluster. These considerations for the gas molecule charge density apply equally well to the induced polarization of the ZIF in the electrostatic potential of an unpolarized gas molecule.

7.6.1 Frozen Core Approximation

The frozen core approximation, described in Section 2.4, demands that the lowest lying orbitals remain doubly occupied, so they do not contribute to the polarization. The induced charge density of all the electrons associated with the gas molecule in its Bader volume is

$$\rho_{ind}^{gas} = \rho_{polarized}^{gas} - \rho_{unpolarized}^{gas}. \tag{7.13}$$

where $\rho_{polarized}^{gas}$ and $\rho_{unpolarized}^{gas}$ include core and valence electrons, in the polarized and unpolarized cases, respectively. Under the frozen core approximation the above equation is replaced with

$$\tilde{\rho}_{ind}^{gas} = \rho_{combined}^{gas} - \rho_{summed\ isolated}^{gas}. \tag{7.14}$$

where $\rho_{combined}^{gas}$ and $\rho_{summed\ isolated}^{gas}$ contain only the valence charge density. The *combined* and *summmed isolated* systems are defined in Section 7.3.3 and serve as the *polarized* and *unpolarized* cases, respectively. $\tilde{\rho}_{ind}^{gas}$ represents the approximated induced charge density, as used in the work in this chapter without the tilde. The difference

$$\tilde{\rho}_{ind}^{gas} - \rho_{ind}^{gas} = \rho_{polarized\ core}^{gas} - \rho_{unpolarized\ core}^{gas} \tag{7.15}$$

is given by the induced polarization in the core, to first order in the induced charge density. The core polarizability of carbon is less than .01 a_0^3 [95] and the isotropic polarizability of carbon dioxide is around 17 a_0^3 [94], therefore we conclude this is a reasonable approximation for our purposes (a_0 is the Bohr radius).

7.6.2 Valence Pseudocharge Approximation

The valence charge density and compensation charge used to calculate the polarization energy is given by the CHGCAR output of VASP 5.2.12.

$$\rho_{CHGCAR} = \tilde{\rho} + \hat{\rho} \tag{7.16}$$

where $\tilde{\rho}$ is the pseudo valence charge density and $\hat{\rho}$ is the compensation charge. This is related to the all-electron valence density (ρ) by

$$\rho = \tilde{\rho} + \hat{\rho} - \hat{\rho} - \tilde{\rho}^1 + \rho^1 \tag{7.17}$$

where 1 denotes an onsite charge density (referred to as region R in Section 2.4), according to the Projector Augmented-Wave method [22, 114]. In VASP the compensation charge, $\hat{\rho}$, is defined such that

$$\rho^1 - \tilde{\rho}^1 - \hat{\rho} \tag{7.18}$$

has vanishing electric multipole moments [68]. We then calculate the error due to using ρ_{CHGCAR} instead of the all electron valence charge density, ρ, for the gas molecule

$$\begin{aligned} E^{gas}_{ind} &= \int d\mathbf{r}[\rho^{gas}_{polarized}(\mathbf{r}) - \rho^{gas}_{unpolarized}(\mathbf{r})]\Phi_{ZIF}(\mathbf{r}) \\ &= \int d\mathbf{r}[\rho^{gasCHGCAR}_{polarized}(\mathbf{r}) - \rho^{gasCHGCAR}_{unpolarized}(\mathbf{r})]\Phi_{ZIF}(\mathbf{r}) \\ + \int d\mathbf{r}[(\rho^1 - \tilde{\rho}^1 - \hat{\rho})^{gas}_{polarized}(\mathbf{r}) &- (\rho^1 - \tilde{\rho}^1 - \hat{\rho})^{gas}_{unpolarized}(\mathbf{r})]\Phi_{ZIF}(\mathbf{r}). \end{aligned} \tag{7.19}$$

The last line of Equation (7.19) can be shown to be zero as follows. Since the charge density of the ZIF (ρ_{ZIF}) and that of the gas molecule are assumed not to overlap significantly, we can rewrite the last term in Eq. (7.19):

$$\begin{aligned} &\int d\mathbf{r}[(\rho^1 - \tilde{\rho}^1 - \hat{\rho})^{gas}_{polarized}(\mathbf{r}) - (\rho^1 - \tilde{\rho}^1 - \hat{\rho})^{gas}_{unpolarized}(\mathbf{r})]\Phi_{ZIF}(\mathbf{r}) \\ &= \int d\mathbf{r}d\mathbf{r}'[(\rho^1 - \tilde{\rho}^1 - \hat{\rho})^{gas}_{polarized}(\mathbf{r}) - (\rho^1 - \tilde{\rho}^1 - \hat{\rho})^{gas}_{unpolarized}(\mathbf{r})]\frac{\rho_{ZIF}(\mathbf{r}')}{|\mathbf{r} - \mathbf{r}'|} \\ &= \int d\mathbf{r}\Phi(\mathbf{r})[(\rho^1 - \tilde{\rho}^1 - \hat{\rho})^{gas}_{polarized} - (\rho^1 - \tilde{\rho}^1 - \hat{\rho})^{gas}_{unpolarized}]\rho_{ZIF}(\mathbf{r}) = 0 \end{aligned} \tag{7.20}$$

where $\Phi(\mathbf{r})[\rho]$ is the potential of the charge distribution in the brackets. By construction the terms $(\rho^1 - \tilde{\rho}^1 - \hat{\rho})$ have zero multiple moments. As a consequence, they give rise to a potential that is zero everywhere outside of the volume of the gas molecule, and the integral in Eq. (7.20) is thus zero. The same steps apply with the ZIF interchanged with the gas molecule, indicating that use of CHGCAR for the ZIF also does not introduce an error in the electrostatic energy.

7.6.3 Using CHGCAR for Bader Volumes

The Bader volume decomposition method divides space according to a steepest accent method in which each point on a grid of charge densities is assigned to a particular volume by following the largest positive gradient until a local maximum is discovered [11]. This definition is consistent with assigning volumes to atoms since the atomic core region contains a large peak in the electron density. However, the core charge density, AECCAR0, an output file from VASP, is slow to converge with respect to the grid, so one may be tempted to use the pseudovalence + compensation charge density, CHGCAR, instead, to

determine the volumes. This can lead to problems since for a particular atom, there may not be a corresponding peak in the CHGCAR (which does not include the core electron states), which means no volume at all will be assigned to that atom. An example of this would be when an atom is covalently bonded to another atom of greater electronegativity, for instance, the carbon in carbon dioxide will not be in the position of a local maximum in the CHGCAR and so the volume in that molecule would be split between the two oxygens.

However, if one calculates the Bader volume of a whole isolated CO_2 molecule in a molecular framework, instead of the constituent atoms, then results will be identical no matter whether the total charge density or the valence charge density is used. The reason for this is that in weakly bonded systems (e.g. van der Waals and electrostatic bonding with negligible charge transfer) the boundary between Bader volumes is determined in the region of low charge density between the molecule and framework. This region is far enough away from the atomic centers that the charge density from the core region is negligible.

We also use Bader analysis to find volumes associated with functional groups bonded to the framework imidazole rings. Here, using the CHGCAR creates volumes that do not correspond to a reasonable charge being associated with each atom. If we find the Bader volume associated with the functional group and the closest carbon on the imidazole ring, much of the volume around this carbon is instead assigned to the nitrogen near it on the ring. Although this charge distribution does not correspond to the Bader volume formed from the all-electron charge density, it suits our purposes for calculating induced dipoles. If the induced charge density in a region away from the functional group is very small, including more or less volume in this region does not change the integrated difference in charge between polarized and unpolarized systems. This means that in most cases, including the carbon and nitrogen on the same side of the imidazole ring as the functional group of interest does not change the calculated difference in dipole due to polarization induced by the gas molecule electrostatic potential. We do include the closest ring carbon and nitrogen in our functional group Bader volumes since we do not want the change in dipole on the functional group to be influenced by charge transfer to and from the ring.

7.6.4 Calculating Changes in Dipoles Associated with Functional Groups and Gas Molecules

Using the formula

$$\mathbf{P}_{gas} = \int d\mathbf{r} \rho_{gas}(\mathbf{r})\mathbf{r} \tag{7.21}$$

to calculate the dipole moment in a region of space gives a quantity that depends on the choice of origin for nonneutral charge distributions. In our systems we encounter these charge distributions when our choice of volume does not include the same amount of electrons as protons in the nuclei. Although for a general charge distribution with both positive and negative values, it does not make sense to define a center of charge, for the electron charge and nuclear charge individually, this definition is clear.

$$\mathbf{r}^{\pm}_{center} = \frac{\int d\mathbf{r}|\rho^{\pm}_{gas}(\mathbf{r})|\mathbf{r}}{\int d\mathbf{r}|\rho^{\pm}_{gas}(\mathbf{r})|} \tag{7.22}$$

where +(-) denotes the formula for the nuclear(electron) center of charge. So we can rewrite the polarization as

$$\mathbf{P}_{gas} = \mathbf{r}^{+}_{center} \int d\mathbf{r} |\rho^{+}_{gas}(\mathbf{r})| - \mathbf{r}^{-}_{center} \int d\mathbf{r} |\rho^{-}_{gas}(\mathbf{r})|. \tag{7.23}$$

Assuming that the magnitudes of positive and negative charge are almost equal, we can imagine adding or subtracting volume to slightly change the number of electrons to obtain a neutral charge distribution. It seems reasonable to do this in a way that does not change $\mathbf{r}^{\pm}_{center}$. If $\mathbf{r}^{\pm}_{center}$ is unchanged by adding or subtracting from the Bader volume, then from the above equation we see that scaling the charge is equivalent to changing the volume. In this way we can reasonably define the part of the dipole moment that is independent of origin.

If we wish to calculate only the change in dipole moment and if the nuclei are held fixed, it is given by

$$\Delta\mathbf{P}_{gas} = \mathbf{r}^{-Polarized}_{center} \int d\mathbf{r} |\rho^{-Polarized}_{gas}(\mathbf{r})| - \mathbf{r}^{-Unpolarized}_{center} \int d\mathbf{r} |\rho^{-Unpolarized}_{gas}(\mathbf{r})| \tag{7.24}$$

and we can rescale the polarized charge to match the unpolarized charge for similar reasons as above. This equation is used for the induced polarizations of the functional groups in this chapter, while equation 7.23 is used to calculate the induced polarization in the gas molecules.

Chapter 8

CO_2 Transport Barriers

The climbing nudged elastic band (climbing-NEB) method is used with the vdW-DF2 and vdW-optB88 to elucidate the effect of framework flexibility on gas transport through the constricted double 8-ring channel of ZIF-97. We find that flexibility reduces the barrier to movement through this channel by 33 meV when compared to the rigid system with relaxed coordinates obtained by the vdW-DF2.

8.1 Introduction

In previous chapters we have primarily discussed gas adsorption and adsorption selectivity in ZIFs. These properties can be useful for gas storage applications, e.g., CO_2 or H_2, as well as gas separations based on adsorption, e.g., CO_2 from N_2 for carbon capture from flue gas or CO_2 from CH_4 for the upgrading of natural gas. In this scheme one gas is selectively adsorbed by the sorbent material. After saturation, this material will need to be regenerated by a swing in pressure or temperature, before being used again.

ZIFs may also be used in membrane separations, taking advantage of both the kinetic selectivity as well as the adsorption selectivity. In this scheme, the preferential flow of a gas or gases through the material is used to separate those gases from others. For this use, the membrane selectivity, α, defined as the ratio of permeabilities, is an important metric[208]. According to Ref. [100], membrane selectivity for gas i over gas j is given by

$$\alpha_{(i/j)} = \frac{x_i/x_j}{y_i/y_j} \times \frac{D_{i,self}(x_i, x_j)}{D_{j,self}(x_i, x_j)} \tag{8.1}$$

where $x_{i(j)}$ is the molar fraction of the adsorbed phase of gas $i(j)$, $y_{i(j)}$ is the molar fraction of the bulk phase of gas $i(j)$, and $D_{i(j),self}(x_i, x_j)$ is the self-diffusivity of gas $i(j)$ in a binary mixture, evaluated at the adsorbed composition (x_i, x_j). The first factor is the adsorption selectivity and the second is the diffusion selectivity. Thus, in addition to the calculations related to adsorption in previous chapters, a computational examination of gas transport in ZIFs would be useful for the evaluation of these materials for membrane separation applications.

Diffusivities for CO_2 and CH_4 have been recently calculated by David Olmsted and co-workers[164] using molecular dynamics (MD) with LAMMPS[177] for the isoreticular set

Table 8.1: CO_2 and CH_4 self-diffusivities in 10^{-9} m^2 s^{-1} at 298 K.

gas	ZIF-25	ZIF-71	ZIF-93	ZIF-96	ZIF-97
CO_2	2.34 ±0.06	3.71 ±0.11	1.19 ±0.06	3.04 ±0.09	0.18 ±0.01
CH_4	3.74 ±0.10	6.08 ±0.17	0.40 ±0.02	7.56 ±0.15	0.79 ±0.04
CO_2/CH_4	0.63	0.61	3.01	0.40	0.23

of **rho** topology ZIFs featured in Chapters 5, 6, and 7. These are ZIF-25, -71, -93, -96, and -97. The MD simulations utilized Lennard-Jones(L-J) and Coulomb potentials. The L-J parameters for the framework were chosen from the universal force field (UFF)[184] and optimized potentials for liquid simulations (OPLS)[96] force field sets. Lorentz-Berthelot mixing rules were utilized, see Chapter 6. The framework charges were derived using the REPEAT algorithm, which fits these charges in such a way as to reproduce the electrostatic potential, calculated with DFT, in open regions of the framework. The periodic DFT calculations were performed using the PBE GGA exchange correlation functional[170] and the PAW method[22] in VASP[112, 113, 110, 111]. The L-J parameters and charges for the CO_2 come from the elementary physical model 2 (EPM2) of Harris and Young[69]. CH_4 is treated as a united atom at the carbon position using the Transferable Potentials for Phase Equilibria - United-Atom (TraPPE-UA) force field[203].

From these simulations, the self-diffusivities were determined for carbon dioxide and methane in the set of **rho** topology ZIFs mentioned in the previous paragraph and are listed in Table 8.1 along with the ratios of diffusivities[164]. In addition, it has been determined, through the work in Ref. [164], and previous examination of the **rho** ZIF structure, that the primary channels for gas transport lie in the <111> direction through the ring of six Zn atoms and in the <001> direction through the double ring of 8 Zn atoms. These channels and rings of Zn atoms are illustrated in Figures 1.1, 5.1, 5.2, and 6.3. The double 8-ring channel is shown in more detail in Figure 8.1. By tracing the movement of gas molecules through two or more pores, the relative importance of transport through the two distinct channels has been quantified. These data are presented in Table 8.2, which gives the number of jumps through each channel per molecule per ns, for both CH_4 and CO_2. These results were obtained for the case of a rigid framework. To assess the effect of the rigid framework approximation, in the following we utilize climbing nudged elastic band (climbing-NEB) calculations to calculate the energy barrier through a channel, with and without framework flexibility. Because these calculations are very expensive (the work here represents over 250k cpu hours), we limit our work to one gas molecule through one channel. The system is chosen to represent the largest effect of flexibility, i.e., transport in the material and gas combination with the smallest self-diffusivity.

The self-diffusivity is smallest for CO_2 through ZIF-97, at 0.18 10^{-9} m^2 s^{-1}. This is the unique gas and **rho** framework combination, in this study, for which the diffusion through the double ring of 8 zinc atoms (<001>) is smaller than diffusion through the ring of six zinc atoms (<111>), in other cases transport through the double 8-ring is dominant. In fact the transport for CO_2 through the zinc 8-ring in ZIF-97 is the slowest example of transport through the double 8-ring by a factor of at least 6 and as high as 123, when compared to the other **rho** topology ZIF materials considered in this Chapter. Therefore, we

Table 8.2: CO_2 and CH_4 jumps through channels in the $< 001 >$ and $< 111 >$ directions, per molecule, per ns at 298 K.

gas	direction	ZIF-25	ZIF-71	ZIF-93	ZIF-96	ZIF-97
CO_2	$< 001 >$	135.7	223.0	69.4	175.9	3.6
	$< 111 >$	5.5	39.5	2.9	60.8	8.1
CH_4	$< 001 >$	222.4	358.2	23.7	443.7	42
	$< 111 >$	0	61.2	1.6	155	1.3

analyze the energy barriers for CO_2 transport though the 8-ring in ZIF-97 in the following, utilizing the vdW-DF2 and vdW-optB88 methods.

8.2 Methods

The calculations proceed exactly as those described for the use of the vdW-DF2[128] in Section 7.3.2. In addition, we also employ the vdW-optB88 method[102]. We use these van der Waals corrected density functionals in the climbing-NEB scheme[73]. In this scheme a minimum energy path is found, between two CO_2 positions for our purposes, using intermediate images effectively connected by springs. The *climbing* modification causes the highest energy image to converge to the saddle-point. We use 4 intermediate images for these calculations and the energies are converged to better than 5 meV.

In order to quantify the effect of flexibility on the barrier through the 8-ring channel for CO_2, we need to compare the fully flexible calculation to a rigid one. However, the framework coordinates relaxed with vdW-optB88 or vdW-DF2 differ from the experimental coordinates. Therefore, we calculate the barriers for three cases with each density functional. These are the rigid framework set to experimental coordinates (refined to X-ray measurements), the rigid framework corresponding to vdW-DF2 or vdW-optB88 relaxed coordinates (forces relaxed to better than 0.01 eV/Å), and the flexible framework within vdW-DF2 or vdW-optB88. In all cases the experimental volume was used. See figure 8.2.

8.3 Results

It was found, both in classical simulations and in vdW-corrected DFT, that there are two equivalent binding sites for each double 8-ring channel of ZIF-97, as illustrated in Figure 8.1 by the two horizontally oriented CO_2 molecules in the rightmost image. These are the 8-ring binding sites (referred to as B sites in Chapters 5 and 7). It should be noted that other **rho** topology ZIFs do not necessarily also have two binding local minima per double 8-ring. Since these two degenerate binding sites each open onto a pore for easy transport into these sites, the primary barrier through the double 8-ring channel in ZIF-97 will be between the two binding positions.

Also shown in Figure 8.1 is a third minimum energy position for CO_2 in the double 8-ring, that we call the 8-ring mid site. CO_2 is more weakly bound here, than in the other two degenerate 8-ring sites, however, this binding position allows us to calculate the barrier

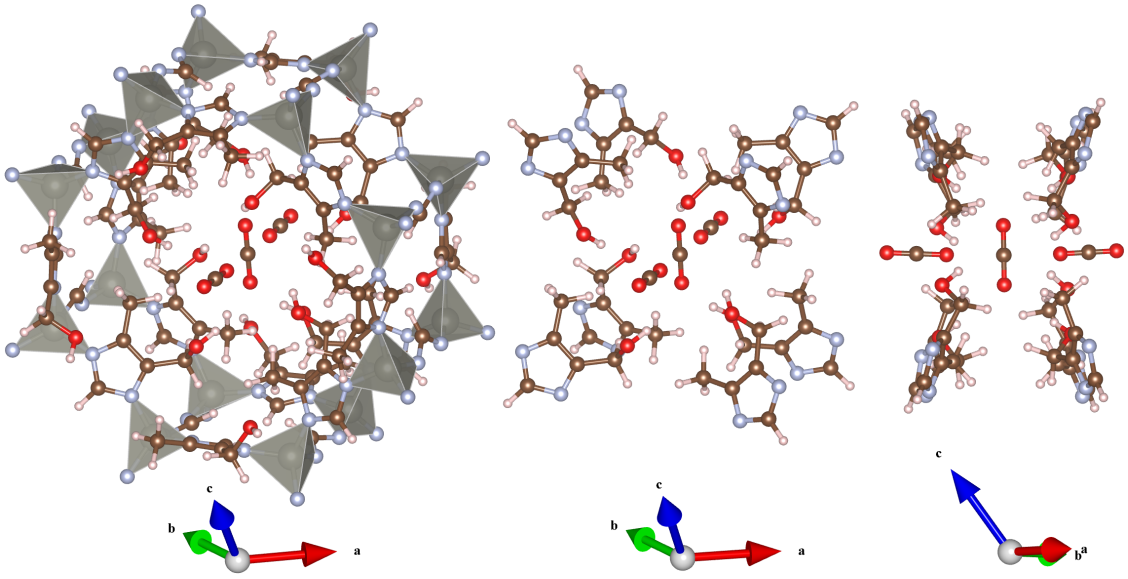

Figure 8.1: CO_2 minimum energy positions in the double 8-ring channel of ZIF-97. The leftmost image shows the double 8-ring of Zn atoms, the middle image shows only the functional groups closest to the bound CO_2 molecules, and the rightmost image shows a side view. The two horizontal CO_2 molecules in the rightmost image are bound at equivalent binding sites, which we call the 8-ring site (B site in Chapters 5 and 7). The vertical CO_2 in the middle position of the double 8-ring channel (shown in all three images) is more weakly bound, but also at a minimum of interaction energy, which we call the 8-ring mid site.

for transport through the double 8-ring channel by only considering transport from a single 8-ring site to the 8-ring mid site. This is due to the symmetry of the channel.

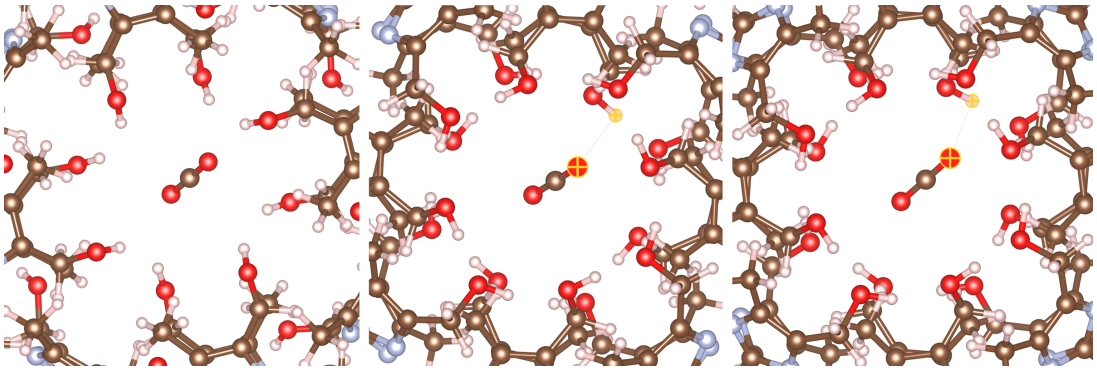

Figure 8.2: CO_2 in double 8-ring channel of ZIF-97. left: experimental coordinates, middle: coordinates relaxed with vdW-DF2, but held rigid in the presence of CO_2, right: coordinates relaxed with vdW-DF2 and kept flexible in the presence of CO_2. Note the positions of the H atoms nearest the CO_2 molecule.

As described in the methods section, we apply the climbing-NEB method to the

Table 8.3: Binding energies (BEs) for CO_2 in the 8-ring site and 8-ring mid site in ZIF-97 as well as the energy barrier into the 8-ring mid site from the 8-ring site, utilizing the vdW-DF2 and vdW-optB88 methods. Different framework coordinates and their flexibility are considered.

method	framework	flexible?	8-ring BE	8-ring mid BE	barrier to mid
vdW-DF2	experiment	No	-463	-399	243
	theory	No	-532	-415	166
	theory	Yes	-552	-426	133
vdW-optB88	experiment	No	-502	-438	235
	theory	No	-567	-470	130
	theory	Yes	-582	-478	118

rigid experimental framework, the rigid theoretical framework (relaxed at constant volume with vdW-DF2 or vdW-optB88), and the flexible framework under vdW-DF2 or vdW-optB88 (also at constant volume). The binding energies in the 8-ring site and the 8-ring mid site, and the barrier height from the former to the latter, calculated using the vdW-DF2 and vdW-optB88 functionals for the three framework cases, are presented in Table 8.3. Binding energies are typically larger in magnitude for the vdW-optB88 method than for the vdW-DF2. Also, the rigid theoretically relaxed frameworks bind CO_2 more strongly than the experimental frameworks for both functionals. The effect of flexibility on the binding of CO_2 can be seen by comparing the binding energies for rigid and flexible structures, both initially relaxed with vdW-DF2 or vdW-optB88. We see that the binding energies are enhanced through flexibility by between 8 and 20 meV for the two sites with the two methods.

The energy barriers, calculated with climbing-NEB, are presented on the rightmost column of Table 8.3. Also, the energy vs. reaction coordinate (representing CO_2 position) results are presented in Figure 8.3. The paths plotted in this figure are splines fit to the energies of the two end points at the 8-ring site and 8-ring mid site, the energies of the four intermediate images, and the forces at each point. With both vdW-DF type methods, the barrier is lower for the rigid relaxed structure than for the experimental structure. Furthermore, as illustrated in the plots, the binding energy of the 8-ring mid site becomes higher relative to the barrier and the 8-ring site. Flexibility has the effect of lowering the barrier in the vdW-DF2 formalism by 33 meV, but only 12 meV with vdW-optB88. The reason for this is that while the energy of the highest energy image does, in fact, decrease for both methods with flexibility, so does the energy of the 8-ring site. In vdW-optB88 the strengthening of the binding in this site partially cancels the decreasing in energy of the highest energy image.

According to transition state theory (TST)[67], the reaction rate is proportional to the Boltzmann factor of the energy barrier between two states. Reaction rate is given explicitly, for the transport from a local minimum over a saddle point, by

$$k = \frac{1}{2\pi} \frac{\prod_{i=0}^{N} \lambda_i^{(0)}}{\prod_{i=0}^{N-1} \lambda_i^{(b)}} \exp(-\beta E_b) \tag{8.2}$$

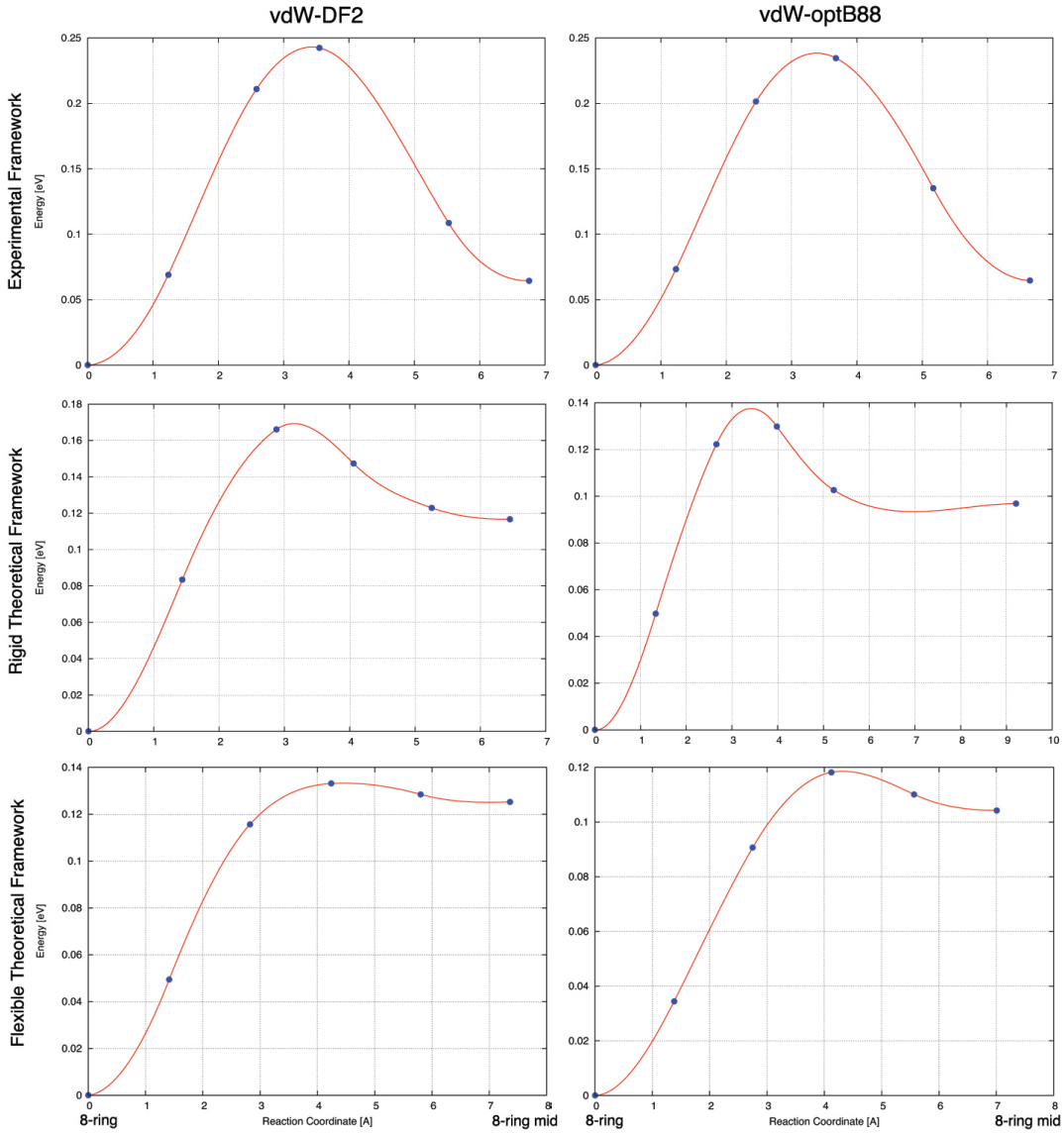

Figure 8.3: The climbing-NEB results are plotted for two different vdW-corrected functionals and three different framework systems, as described in the text.

where $\lambda_i^{(0)}$ and $\lambda_i^{(b)}$ are the real vibrational frequencies at the minimum and saddle point, respectively, β is the product of the Boltzmann constant and the temperature, and E_b is the barrier height. Therefore, the 33 meV difference in the barrier height predicted by vdW-DF2 corresponds to a difference in rate by a factor of $e^{.033/.0256} \approx 3.6$ at room temperature, assuming the vibrational frequencies are not affected. As mentioned above, vdW-optB88 predicts a smaller difference in the barrier.

These results are for only CO_2 transport through the double-8 ring channel in ZIF-97. Thus, if the rate was increased by a factor of 3.6 through this channel only, the

overall self-diffusivity for CO_2 in ZIF-97 might change by a factor of $\sim$2. That is, looking at Table 8.2, if we increase the value of the CO_2 jumps in the $< 001 >$ direction by a factor of 3.6 and keep the jumps in the $< 111 >$ direction constant, the overall jumps through either channel would increase by a factor of $\sim$2. Such a change in Table 8.1 would not cause this self-diffusivity to surpass another gas-ZIF combination. So, if the effect of flexibility calculated here is an upper bound for these systems, it is likely that flexibility does not change qualitative results, i.e., the order of the channels and gases according to transport, in this set of materials with these gases.

8.4 Conclusion

Using vdW-DF2 and vdW-optB88, we have identified and calculated the binding energies of three binding sites for CO_2 in the double 8-ring channel of ZIF-97, two of which were found to be degenerate. Next, the barrier for transport through this channel was calculated using the same density functionals with the climbing-NEB method. The results show that framework flexibility may account for a change of transport barrier of up to 33 meV. The barrier change is not as large as might likely be expected because although flexibility decreases the energy of the highest energy position on the reaction path, it also strengthens the binding in the local minimum. The same logic applies to the results for different vdW-corrected density functionals, i.e., the differences in the barriers calculated with the two methods is smaller than the differences in the individual binding energies. Thus the calculation of energy barriers is less sensitive to the choice of vdW-DF than individual interaction energies.

Part III

Summary, Conclusions, and Future Work

Chapter 9

Summary, Conclusions, and Future Work

9.1 Summary

In this dissertation we have discussed the background and derivation, as pieced together from the literature, of a theoretical framework for vdW-corrected ab-initio electronic structure calculations, the vdW-DF. We then applied this framework to the study of gas adsorption and transport in ZIFs, as well as the interlayer cohesion of graphite, the binding of a Kr dimer, and the adsorption of metal atoms and molecular hydrogen on graphene.

In Chapter 2, the DFT formalism, exchange-correlation functional, and PAW method were introduced. Because different vdW-DF type methods, described in Section 3.3.2, utilize different semi-local exchange functionals, a basic understanding of these functionals is important to understanding the behavior of the vdW-DF variants. Larger exchange enhancement factors correspond to more repulsive functionals because they reduce the energy of separated systems compared to those that are bound. PBE PAW potentials are used for the work presented in this dissertation, instead of potentials created with the vdW-DF, however previous results indicate that this scheme has a small effect on calculated binding energies[64].

vdW-DF type calculations on the binding of a noble gas dimer and graphite layers, as well as metal atoms and molecular hydrogen on graphene were discussed in Chapter 4. In the systems for which dispersion dominates the binding, i.e., the Kr dimer, graphite, and H_2 on graphene, the vdW-DF2 and vdW-B88 methods give binding energies and distances which are in good agreement with experiment. With both functionals, the binding energies for the Kr dimer and the cohesive energy for graphite are within 6 and 16 meV of experiment, respectively, and binding distances are calculated within an accuracy of 0.2 Å. Ionic contributions dominate the binding of Li and Al to graphene and as a result the binding distances are at least 1 Å shorter than the dispersion bound systems considered in this chapter. Therefore, the short ranged exchange part of the vdW-DF type methods is more important in these systems than in systems that are solely dispersion bound. Different exchange functionals are used in the vdW-DF2 and vdW-optB88 methods, PW86 and optB88, respectively. For Li and Al on graphene, the vdW-optB88 binding energies

are consistent with the values expected from the addition of a dispersion attraction to the binding energy calculated with PBE (which already captures the larger ionic contribution). However, the vdW-DF2 predicts binding energies which are smaller in magnitude compared to PBE. From the results we obtain with these example systems, in addition to results from the literature[128, 102, 180, 179, 107, 108], we expect the non-bonded (i.e. no ionic or colvalent contribution) interactions important to gas adsorption and transport in the remainder of the work presented to be well represented by both vdW-DF2 and vdW-optB88.

In Chapters 5 and 7, we examined CO_2 and CH_4 binding in a set of **rho** topology ZIF materials that only differ in the functionalization of the imidazolate linker. For these systems, three symmetry distinct binding sites are present. Depending on the binding site and gas molecule, dispersion or a combination of dispersion, electrostatic interactions, and hydrogen bonding, are important. Because the relevant interactions vary with respect to binding site, the effect of the functional group is also different in the three sites. The binding site in the channel that runs through a ring of six zinc atoms is dominated by dispersion interactions. In this site the attraction for CO_2 and CH_4 is found to be relatively independent of the ZIF chemical functionalization. In the site inside a double ring of 8 zinc atoms, electrostatic interactions make a significant contribution to CO_2 binding. Specifically, the CO_2 adsorption is enhanced in ZIFs with two different functional groups attached to each imidazole ring, which changes the ZIF electric field symmetry. The functional group dependent electrostatic interaction also increases the selectivity for CO_2 over CH_4 in these ZIFs because CH_4 lacks electrostatic multipole moments lower than the octupole. Thus, the CH_4 adsorption is not also increased. The last site is located on the surface of the pore found in these **rho** topology ZIFS. In this site steric constraints to the entrance, that differ depending on the size of the functional group, can cause selective adsorption of the linear CO_2 molecule over the tetrahedral CH_4 molecule. Therefore, it is demonstrated with ab-initio vdW-corrected DFT that ZIF functionalization can enhance CO_2 uptake and selectivity over CH_4 through two distinct mechanisms: electrostatics and geometry.

The effect of framework topology on the binding of CO_2 is investigated in Chapter 6. Maps of the binding energy versus position are calculated with classical force fields for the free space in two pairs of ZIFs. These maps are used to rationalize the adsorption performance for different topologies at low and high pressure. Within each pair of materials the chemical functionalization is identical, but the topology differs. The smaller ZIF pores and channels of the **sod** structure are calculated to bind CO_2 more strongly than the larger pores and channels of the **rho** topology ZIFs. However, of these two topologies, the surface area is higher in the **rho** case. Subsequently, the uptake at low pressure is higher in the **sod** topology since the occupation of each site is higher than the occupation of the sites in the **rho** topology material. At high pressure the uptake is higher in **rho** topolgy ZIFs because there is more surface area for adsorption. Also in this chapter, the same analysis of binding energy landscape is applied to pressure dependent CH_4 adsorption, for the **rho** ZIFs considered in Chapters 5 and 7. The 6-ring binding site is calculated to bind CH_4 more strongly than the 8-ring site or the surface of the pore. Thus, adsorption at low pressure occurs primarily in the 6-ring site and uptake at high pressure is more evenly spread between the binding sites and pore surface.

Calculations of the barrier for the transport of CO_2 through the double 8-ring

channel of ZIF-97 are presented in Chapter 8. It is found that this barrier is highly dependent on the framework coordinates. The experimentally determined structure has a barrier that is higher than the barrier of the theoretically relaxed structure, determined by vdW-DF2 (vdW-optB88), by 77 (105) meV. In those calculations the framework was held rigid. Adding flexibility to the theoretically relaxed structure reduces the barrier by a further 33 meV for vdW-DF2 and 12 meV for vdW-optB88.

9.2 Conclusions

The uptake of CO_2 and CH_4 in ZIFs was found to depend on several properties of these materials. For both gas molecules, polarizable functional groups increase the dispersion attraction, however, this interaction is greatly influenced by the geometry of the binding site. That is, the dispersion contribution to the binding energy is highest in binding sites that feature as many framework atoms as possible at a distance of $\sim$3 Å from the gas molecule binding position. Therefore, small pores and channels in ZIFs are likely to be important binding sites. Materials with structures that support many such binding sites will have high adsorptions at low pressures. However, these geometries are associated with less total surface area, which hampers high pressure uptake. For the optimization of adsorption at high pressure, surface area is of paramount importance and larger pores and channels, capable of multiple occupancy, are preferred.

For CO_2, electrostatic interactions were found to strongly enhance the binding energy. The energy associated with induced polarizations (electrostatic induction), can contribute -110 meV to the energy of the bound system. In addition, the energy of interaction between the unpolarized ZIF and CO_2 charge distributions can vary by more than 180 meV in a single binding site with respect to changes in the functionalization of the imidazolate linker. Like the dispersion energy, these interactions also depend on binding site geometry. Asymmetric functionalizations of the imidazole ring that protrude into ZIF pores and channels enhance binding the most when the CO_2 molecule can line up its negatively (positively) charged atoms near positively (negatively) charged framework atoms. Thus, strong electrostatic gas-framework interactions are a combined effect of framework topology, symmetry, and functionallization.

The adsorption selectivity of CO_2 over CH_4 can be engineered by replicating the properties observed to enhance electrostatic interactions since these interactions will not increase CH_4 uptake. Furthermore, the linear CO_2 molecule will fit into some binding sites that CH_4 will not. Thus, carefully designed steric constraints will also increase CO_2/CH_4 adsorption selectivity. In addition, steric constraints introduced through ZIF functionalization can also affect diffusion selectivity.

Of several flavors of the van der Waals density functional, the vdW-DF2 and vdW-optB88 are among the most reliable methods for binding energies and distances in non-bonded systems. These methods are both based on the original vdW-DF, which includes the non-local correlation energy as a double integral over electron densities. The differences between these two methods are two-fold. The dispersion energy due to non-local electron correlation is larger in the vdW-optB88 method and the exchange functional is less repulsive. Thus, the binding energies calculated with this functional are typically

larger than those calculated with vdW-DF2. However, this discrepancy is relatively small for systems that are primarily bound by the London dispersion force. In these systems, the cohesive energies compare well with experiment, which is impressive considering that these forces are relatively weak.

In systems with mixed binding, i.e., exhibiting strong covalent or ionic contributions, the short-range behavior of vdW-DF methods becomes more important. Previous research has shown that the vdW-DF2 predicts binding energies that are too weak in these systems. Therefore, in mixed binding situations vdW-DF2 results should be thoroughly benchmarked with experiment, before proceeding with derivative calculations. It would seem there is a difficulty in choosing (in a rigorous way) the best exchange functional to pair with the non-local correlation energy, which has somewhat of a GGA character at short-range. The fitting of the optB88 exchange functional in the vdW-optB88 method to CCSD(T) results appears to have solved this problem in an empirical fashion while the vdW-DF2 has no fit parameters.

9.3 Future Work

Open questions remain for both the gas-ZIF system and the vdW-DF method. ZIF-93 was shown to have high diffusion selectivity as well as high adsorption selectivity for CO_2 over CH_4. Therefore, the CO_2/CH_4 membrane selectivity of this material should be competitive with the best from industry, making ZIF-93 potentially very attractive for natural gas upgrading applications. In this ZIF the self-diffusion is higher for CO_2 than CH_4 which is unique among the five **rho** topology ZIFs considered. It could be worthwhile to examine the origins of this behavior using first principles methods.

Dispersion contributions to the cohesive energy are important to many materials, such as graphite and polymer crystals. The open ZIF structure, although primarily covalently bound, may be influenced by van der Waals interactions and further study with vdW-DF methods could be fruitful. Structural properties may be interesting in their own right, e.g., MOFs have been shown to exhibit negative thermal expansion[235, 142]. In addition, gas separation properties may be enhanced through pressure induced structural phase changes, as they are in ZIF-7.

The vdW-DF method is still relatively young and improvements are likely possible. The vdW-optB88 version produces more accurate results across a range of systems than several other versions due to its fit exchange functional. It appears worthwhile to try to more rigorously derive an appropriate exchange functional for a new vdW-DF method utilizing similar design considerations as successful GGAs.

Bibliography

[1] Carlo Adamo and Vincenzo Barone. Toward reliable density functional methods without adjustable parameters: The pbe0 model. *The Journal of chemical physics*, 110:6158, 1999.

[2] Sonia Aguado, Gerard Bergeret, Marc Pera Titus, Virginie Moizan, Carlos Nieto-Draghi, Nicolas Bats, and David Farrusseng. Guest-induced gate-opening of a zeolite imidazolate framework. *New J. Chem.*, 35:546–550, 2011.

[3] Sonia Aguado, Jerome Canivet, and David Farrusseng. Facile shaping of an imidazolate-based mof on ceramic beads for adsorption and catalytic applications. *Chemical Communications*, 46(42):7999–8001, 2010.

[4] Sonia Aguado, Charles-Henri Nicolas, Virginie Moizan-Baslé, Carlos Nieto, Hedi Amrouche, Nicolas Bats, Nathalie Audebrand, and David Farrusseng. Facile synthesis of an ultramicroporous mof tubular membrane with selectivity towards co2. *New Journal of Chemistry*, 35(1):41–44, 2011.

[5] Hedi Amrouche, Sonia Aguado, Javier Pérez-Pellitero, Céline Chizallet, Flor Siperstein, David Farrusseng, Nicolas Bats, and Carlos Nieto-Draghi. Experimental and computational study of functionality impact on sodalite–zeolitic imidazolate frameworks for co2 separation. *The Journal of Physical Chemistry C*, 115(33):16425–16432, 2011.

[6] Tsuneya Ando. Excitons in carbon nanotubes. *Journal of the Physical Society of Japan*, 66(4):1066–1073, 1997.

[7] Bassem Assfour, Stefano Leoni, Sergei Yurchenko, and Gotthard Seifert. Hydrogen storage in zeolite imidazolate frameworks. a multiscale theoretical investigation. *International Journal of Hydrogen Energy*, 36(10):6005 – 6013, 2011.

[8] Erhan Atci and Seda Keskin. Understanding the potential of zeolite imidazolate framework membranes in gas separations using atomically detailed calculations. *The Journal of Physical Chemistry C*, 116(29):15525–15537, 2012.

[9] BM Axilrod and Ei Teller. Interaction of the van der waals type between three atoms. *The Journal of Chemical Physics*, 11(6):299–300, 1943.

[10] R. Babarao and J. Jiang. Upgrade of natural gas in rho zeolite-like metal–organic framework and effect of water: a computational study. *Energy Environ. Sci.*, 2(10):1088–1093, 2009.

[11] Richard FW Bader. *Atoms in molecules*. Wiley Online Library, 1990.

[12] Tae-Hyun Bae, Jong Suk Lee, Wulin Qiu, William J. Koros, Christopher W. Jones, and Sankar Nair. A high-performance gas-separation membrane containing submicrometer-sized metalorganic framework crystals. *Angewandte Chemie International Edition*, 49(51):9863–9866, 2010.

[13] Rahul Banerjee, Anh Phan, Bo Wang, Carolyn Knobler, Hiroyasu Furukawa, Michael O'Keeffe, and Omar M. Yaghi. High-throughput synthesis of zeolitic imidazolate frameworks and application to co2 capture. *Science*, 319(5865):939–943, 2008.

[14] Z. Bao, S. Alnemrat, L. Yu, I. Vasiliev, Q. Ren, X. Lu, and S. Deng. Kinetic separation of carbon dioxide and methane on a copper metal–organic framework. *Journal of Colloid and Interface Science*, 357(2):504–509, 2011.

[15] Z. Bao, L. Yu, Q. Ren, X. Lu, and S. Deng. Adsorption of co2 and ch4 on a magnesium-based metal organic framework. *Journal of colloid and interface science*, 353(2):549–556, 2011.

[16] Rodney J Bartlett. Many-body perturbation theory and coupled cluster theory for electron correlation in molecules. *Annual Review of Physical Chemistry*, 32(1):359–401, 1981.

[17] Anna Battisti, Simone Taioli, and Giovanni Garberoglio. Zeolitic imidazolate frameworks for separation of binary mixtures of co2, ch4, n2 and h2: A computer simulation investigation. *Microporous and Mesoporous Materials*, 143(1):46 – 53, 2011.

[18] A. Becke. Density-functional exchange-energy approximation with correct asymptotic behavior. *Physical Review A*, 38(6):3098–3100, 1988.

[19] Gavi E Begtrup, Keith G Ray, Brian M Kessler, Thomas D Yuzvinsky, Henry Garcia, and Alex Zettl. Probing nanoscale solids at thermal extremes. *Physical review letters*, 99(15):155901, 2007.

[20] Kristian Berland and Per Hyldgaard. An analysis of van der waals density functional components: Binding and corrugation of benzene and c60 on boron nitride and graphene. *arXiv preprint arXiv:1303.0389*, 2013.

[21] Daniel Berthelot. Sur le mélange des gaz. *Comptes Rendus*, 126:1703–1706, 1898.

[22] P. Blöchl. Projector augmented-wave method. *Physical Review B*, 50(24):17953–17979, 1994.

[23] Peter E Blöchl. Generalized separable potentials for electronic-structure calculations. *Physical Review B*, 41(8):5414, 1990.

[24] Aaron Bostwick, Taisuke Ohta, Thomas Seyller, Karsten Horn, and Eli Rotenberg. Quasiparticle dynamics in graphene. *Nature Physics*, 3(1):36–40, 2006.

[25] Helge Bux, Christian Chmelik, Jasper M. van Baten, Rajamani Krishna, and Jürgen Caro. Novel mof-membrane for molecular sieving predicted by ir-diffusion studies and molecular modeling. *Advanced Materials*, 22(42):4741–4743, 2010.

[26] Carlos Campañá, Bastien Mussard, and Tom K. Woo. Electrostatic potential derived atomic charges for periodic systems using a modified error functional. *Journal of Chemical Theory and Computation*, 5(10):2866–2878, 2009.

[27] H. Casimir and D. Polder. The influence of retardation on the london-van der waals forces". *Physical Review*, 73(4):360–372, 1948.

[28] AH Castro Neto and Francisco Guinea. Impurity-induced spin-orbit coupling in graphene. *Physical review letters*, 103(2):026804, 2009.

[29] S. Cavenati, A. Carlos, and A.E. Rodrigues. Upgrade of methane from landfill gas by pressure swing adsorption. *Energy & fuels*, 19(6):2545–2555, 2005.

[30] A. Celzard and V. Fierro. Preparing a suitable material designed for methane storage: a comprehensive report. *Energy & fuels*, 19(2):573–583, 2005.

[31] Kevin T Chan, JB Neaton, and Marvin L Cohen. First-principles study of metal adatom adsorption on graphene. *Physical Review B*, 77(23):235430, 2008.

[32] JT Chayes, L Chayes, and Mary Beth Ruskai. Density functional approach to quantum lattice systems. *Journal of statistical physics*, 38(3-4):497–518, 1985.

[33] J-H Chen, C Jang, S Adam, MS Fuhrer, ED Williams, and M Ishigami. Charged-impurity scattering in graphene. *Nature Physics*, 4(5):377–381, 2008.

[34] L. Chen, C.A. Morrison, and T. Duren. Improving predictions of gas adsorption in metal-organic frameworks with coordinatively unsaturated metal sites: Model potentials, ab initio parameterization, and gcmc simulations. *The Journal of Physical Chemistry C*, 2012.

[35] Christian Chmelik, Dieter Freude, Helge Bux, and Jürgen Haase. Ethene/ethane mixture diffusion in the mof sieve zif-8 studied by mas pfg nmr diffusometry. *Microporous and Mesoporous Materials*, 147(1):135 – 141, 2012.

[36] Jiří Čížek. On the correlation problem in atomic and molecular systems. calculation of wavefunction components in ursell-type expansion using quantum-field theoretical methods. *The Journal of Chemical Physics*, 45:4256, 1966.

[37] F Coester. Bound states of a many-particle system. *Nuclear Physics*, 7:421–424, 1958.

[38] Fritz Coester and Hermann Kümmel. Short-range correlations in nuclear wave functions. *Nuclear Physics*, 17:477–485, 1960.

[39] Philip G Collins and A Zettl. Unique characteristics of cold cathode carbon-nanotube-matrix field emitters. *Physical Review B*, 55(15):9391, 1997.

[40] Robert F Curl and Richard E Smalley. Probing c60. *Science*, 242(4881):1017–1022, 1988.

[41] Leszek Czepirski and Jacek Jagieo. Virial-type thermal equation of gassolid adsorption. *Chemical Engineering Science*, 44(4):797 – 801, 1989.

[42] William IF David, Richard M Ibberson, Judy C Matthewman, Kosmas Prassides, T John S Dennis, Jonathan P Hare, Harold W Kroto, Roger Taylor, and David RM Walton. Crystal structure and bonding of ordered c60. *Nature*, 353(6340):147–149, 1991.

[43] Mark E Davis and Raul F Lobo. Zeolite and molecular sieve synthesis. *Chemistry of Materials*, 4(4):756–768, 1992.

[44] F. Debatin, J. Möllmer, S.S. Mondal, K. Behrens, A. Möller, R. Staudt, A. Thomas, and H.J. Holdt. Mixed gas adsorption of carbon dioxide and methane on a series of isoreticular microporous metal–organic frameworks based on 2-substituted imidazolate-4-amide-5-imidates. *Journal of Materials Chemistry*, 22(20):10221–10227, 2012.

[45] P.D.C. Dietzel, V. Besikiotis, and R. Blom. Application of metal–organic frameworks with coordinatively unsaturated metal sites in storage and separation of methane and carbon dioxide. *J. Mater. Chem.*, 19(39):7362–7370, 2009.

[46] M. Dion, H. Dydberg, E. Schröder, D. C. Langreth, and B. I. Lundqvist. Van der waals density functional for general geometries. *Physical Review Letters*, 92(24), 2004.

[47] John F Dobson, Angela White, and Angel Rubio. Asymptotics of the dispersion interaction: analytic benchmarks for van der waals energy functionals. *Physical review letters*, 96(7):73201, 2006.

[48] TW Ebbesen and PM Ajayan. Large-scale synthesis of carbon nanotubes. *Nature*, 358(6383):220–222, 1992.

[49] V Fock. Näherungsmethode zur lösung des quantenmechanischen mehrkörperproblems. *Zeitschrift für Physik*, 61(1-2):126–148, 1930.

[50] WMC Foulkes, L Mitas, RJ Needs, and G Rajagopal. Quantum monte carlo simulations of solids. *Reviews of Modern Physics*, 73(1):33, 2001.

[51] Hiroyasu Furukawa, Michael A Miller, and Omar M Yaghi. Independent verification of the saturation hydrogen uptake in mof-177 and establishment of a benchmark for hydrogen adsorption in metal–organic frameworks. *Journal of Materials Chemistry*, 17(30):3197–3204, 2007.

[52] Edder J Garca, John PS Mowat, Paul A Wright, Javier Prez-Pellitero, Christian Jallut, and Gerhard D Pirngruber. Role of structure and chemistry in controlling separations of co2/ch4 and co2/ch4/co mixtures over honeycomb mofs with coordinatively unsaturated metal sites. *The Journal of Physical Chemistry C*, 116(50):26636–26648, 2012.

[53] Andre K Geim and Konstantin S Novoselov. The rise of graphene. *Nature materials*, 6(3):183–191, 2007.

[54] Isabella Gierz, Christian Riedl, Ulrich Starke, Christian R Ast, and Klaus Kern. Atomic hole doping of graphene. *Nano letters*, 8(12):4603–4607, 2008.

[55] C Graham, J Pierrus, and RE Raab. Measurement of the electric quadrupole moments of co2, co and n2. *Molecular Physics*, 67(4):939–955, 1989.

[56] Gabriella Graziano, Jiří Klimeš, Felix Fernandez-Alonso, and Angelos Michaelides. Improved description of soft layered materials with van der waals density functional theory. *Journal of Physics: Condensed Matter*, 24(42):424216, 2012.

[57] Stefan Grimme. Accurate description of van der waals complexes by density functional theory including empirical corrections. *Journal of computational chemistry*, 25(12):1463–1473, 2004.

[58] Stefan Grimme. Semiempirical gga-type density functional constructed with a long-range dispersion correction. *Journal of computational chemistry*, 27(15):1787–1799, 2006.

[59] Stefan Grimme, Jens Antony, Stephan Ehrlich, and Helge Krieg. A consistent and accurate ab initio parametrization of density functional dispersion correction (dft-d) for the 94 elements h-pu. *The Journal of Chemical Physics*, 132:154104, 2010.

[60] Olle Gunnarsson and BI Lundqvist. Exchange and correlation in atoms, molecules, and solids by the spin-density-functional formalism. *Physical Review B*, 13(10):4274, 1976.

[61] Hai-chao Guo, Fan Shi, Zheng-fei Ma, and Xiao-qin Liu. Molecular simulation for adsorption and separation of ch4/h2 in zeolitic imidazolate frameworks. *The Journal of Physical Chemistry C*, 114(28):12158–12165, 2010.

[62] Canan Gcyener, Johan van den Bergh, Jorge Gascon, and Freek Kapteijn. Ethane/ethene separation turned on its head: Selective ethane adsorption on the metal- organic framework zif-7 through a gate-opening mechanism. *Journal of the American Chemical Society*, 132(50):17704–17706, 2010.

[63] Jürgen Hafner, Christopher Wolverton, and Gerbrand Ceder. Toward computational materials design: the impact of density functional theory on materials research. *MRS bulletin*, 31(09):659–668, 2006.

[64] Ikutaro Hamada and Susumu Yanagisawa. Pseudopotential approximation in van der waals density functional calculations. *Physical Review B*, 84(15):153104, 2011.

[65] DR Hamann, M Schlüter, and C Chiang. Norm-conserving pseudopotentials. *Physical Review Letters*, 43(20):1494–1497, 1979.

[66] Sang Soo Han, Seung-Hoon Choi, and William A. Goddard. Zeolitic imidazolate frameworks as h2 adsorbents: Ab initio based grand canonical monte carlo simulation. *The Journal of Physical Chemistry C*, 114(27):12039–12047, 2010.

[67] Peter Hänggi, Peter Talkner, and Michal Borkovec. Reaction-rate theory: fifty years after kramers. *Reviews of Modern Physics*, 62(2):251, 1990.

[68] Judith Harl. *The linear response function in density functional theory.* PhD thesis, uniwien, 2008.

[69] Jonathan G. Harris and Kwong H. Yung. Carbon dioxide's liquid-vapor coexistence curve and critical properties as predicted by a simple molecular model. *The Journal of Physical Chemistry*, 99(31):12021–12024, 1995.

[70] Hideki Hayashi, Adrien P. Cote, Hiroyasu Furukawa, Michael O'Keeffe, and Omar M. Yaghi. Zeolite a imidazolate frameworks. *Nat Mater*, 6(7):501–506, 07 2007.

[71] AF Hebard, MJ Rosseinky, RC Haddon, DW Murphy, SH Glarum, TTM Palstra, AP Ramirez, and AR Karton. Potassium-doped c60. *Nature*, 350:600–601, 1991.

[72] G. Henkelman, A. Arnaldsson, and H. Jónsson. A fast and robust algorithm for bader decomposition of charge density. *Computational Materials Science*, 36(3):354–360, 2006.

[73] Graeme Henkelman, Blas P Uberuaga, and Hannes Jónsson. A climbing image nudged elastic band method for finding saddle points and minimum energy paths. *The Journal of Chemical Physics*, 113:9901, 2000.

[74] D Henwood and J David Carey. Ab initio investigation of molecular hydrogen physisorption on graphene and carbon nanotubes. *Physical Review B*, 75(24):245413, 2007.

[75] Z.R. Herm, R. Krishna, and J.R. Long. Co2/ch4, ch4/h2 and co2/ch4/h2 separations at high pressures using mg2 (dobdc). *Microporous and Mesoporous Materials*, 151:481, 2012.

[76] Frank Herman, John P Van Dyke, and Irene B Ortenburger. Improved statistical exchange approximation for inhomogeneous many-electron systems. *Physical Review Letters*, 22(16):807–811, 1969.

[77] FL Hirschfeld. Theoretical chemistry accounts: Theory, computation and modeling. *Theor. Chim. Acta*, 44:129, 1977.

[78] Pierre Hohenberg and Walter Kohn. Inhomogeneous electron gas. *Physical Review*, 136(3B):B864, 1964.

[79] Xin-Juan Hou and Huiquan Li. Unraveling the high uptake and selectivity of co2 in the zeolitic imidazolate frameworks zif-68 and zif-69. *The Journal of Physical Chemistry C*, 114(32):13501–13508, 2010.

[80] Yao A Houndonougbo, Christopher Signer, Ning He, William Morris, Hiroyasu Furukawa, Keith G Ray, David L Olmsted, Mark D Asta, Brian Bostian Laird, and Omar M Yaghi. A combined experimental-computational investigation of methane adsorption and selectivity in a series of isoreticular zeolitic imidazolate frameworks. *The Journal of Physical Chemistry C*.

[81] H. Huang, W. Zhang, D. Liu, and C. Zhong. Understanding the effect of trace amount of water on co2 capture in natural gas upgrading in metal–organic frameworks: A molecular simulation study. *Industrial & Engineering Chemistry Research*, 2012.

[82] Hongliang Huang, Wenjuan Zhang, Dahuan Liu, Bei Liu, Guangjin Chen, and Chongli Zhong. Effect of temperature on gas adsorption and separation in zif-8: A combined experimental and molecular simulation study. *Chemical Engineering Science*, 66(23):6297 – 6305, 2011.

[83] Hongliang Huang, Wenjuan Zhang, Dahuan Liu, and Chongli Zhong. Understanding the effect of trace amount of water on co2 capture in natural gas upgrading in metalorganic frameworks: A molecular simulation study. *Industrial and Engineering Chemistry Research*, 51(30):10031–10038, 2012.

[84] Xiao-Chun Huang, Yan-Yong Lin, Jie-Peng Zhang, and Xiao-Ming Chen. Ligand-directed strategy for zeolite-type metal–organic frameworks: Zinc (ii) imidazolates with unusual zeolitic topologies. *Angewandte Chemie*, 118(10):1587–1589, 2006.

[85] Xiao-Chun Huang, Yan-Yong Lin, Jie-Peng Zhang, and Xiao-Ming Chen. Ligand-directed strategy for zeolite-type metal–organic frameworks: Zinc(ii) imidazolates with unusual zeolitic topologies. *Angewandte Chemie International Edition*, 45(10):1557–1559, 2006.

[86] Mark S Hybertsen and Steven G Louie. Electron correlation in semiconductors and insulators: Band gaps and quasiparticle energies. *Physical Review B*, 34(8):5390, 1986.

[87] Sumio Iijima. Carbon nanotubes: past, present, and future. *Physica B: Condensed Matter*, 323(1):1–5, 2002.

[88] Sumio Iijima et al. Helical microtubules of graphitic carbon. *nature*, 354(6348):56–58, 1991.

[89] Sumio Iijima and Toshinari Ichihashi. Single-shell carbon nanotubes of 1-nm diameter. 1993.

[90] Niclas Jacobson, Bengt Tegner, Elsebeth Schröder, Per Hyldgaard, and Bengt I Lundqvist. Hydrogen dynamics in magnesium and graphite. *Computational materials science*, 24(1):273–277, 2002.

[91] Jacek Jagiello, Teresa J Bandosz, Karol Putyera, and James A Schwarz. Adsorption near ambient temperatures of methane, carbon tetrafluoride, and sulfur hexafluoride on commercial activated carbons. *Journal of Chemical and Engineering Data*, 40(6):1288–1292, 1995.

[92] Stuart L James. Metal-organic frameworks. *Chemical Society Reviews*, 32(5):276–288, 2003.

[93] C. Janiak. Functional organic analogues of zeolites based on metal–organic coordination frameworks. *Angewandte Chemie International Edition in English*, 36(13-14):1431–1434, 2003.

[94] BL Jhanwar and William J Meath. Dipole oscillator strength distributions, sums, and dispersion energy coefficients for co and co2. *Chemical Physics*, 67(2):185–199, 1982.

[95] WR Johnson, Dietmar Kolb, and K-N Huang. Electric-dipole, quadrupole, and magnetic-dipole susceptibilities and shielding factors for closed-shell ions of the he, ne, ar, ni (cu+), kr, pb, and xe isoelectronic sequences. *Atomic Data and Nuclear Data Tables*, 28(2):333–340, 1983.

[96] William L. Jorgensen and Julian. Tirado-Rives. The opls [optimized potentials for liquid simulations] potential functions for proteins, energy minimizations for crystals of cyclic peptides and crambin. *Journal of the American Chemical Society*, 110(6):1657–1666, 1988.

[97] George A Kaminski, Richard A Friesner, Julian Tirado-Rives, and William L Jorgensen. Evaluation and reparametrization of the opls-aa force field for proteins via comparison with accurate quantum chemical calculations on peptides. *The Journal of Physical Chemistry B*, 105(28):6474–6487, 2001.

[98] S.S. Kaye, A. Dailly, O.M. Yaghi, and R. Jeffrey. Impact of preparation and handling on the hydrogen storage properties of zn4o (1, 4-benzenedicarboxylate) 3 (mof-5). *Journal of the American Chemical Society*, 129(46):14176–14177, 2007.

[99] S. Keskin and D.S. Sholl. Screening metal-organic framework materials for membrane-based methane/carbon dioxide separations. *The Journal of Physical Chemistry C*, 111(38):14055–14059, 2007.

[100] Seda Keskin. Atomistic simulations for adsorption, diffusion, and separation of gas mixtures in zeolite imidazolate frameworks. *The Journal of Physical Chemistry C*, 115(3):800–807, 2010.

[101] Seda Keskin, Jinchen Liu, Rees B Rankin, J Karl Johnson, and David S Sholl. Progress, opportunities, and challenges for applying atomically detailed modeling to

molecular adsorption and transport in metal- organic framework materials. *Industrial & Engineering Chemistry Research*, 48(5):2355–2371, 2008.

[102] Jiří Klimeš, David R Bowler, and Angelos Michaelides. Chemical accuracy for the van der waals density functional. *Journal of Physics: Condensed Matter*, 22(2):022201, 2010.

[103] Jiří Klimeš, David R. Bowler, and Angelos Michaelides. Van der waals density functionals applied to solids. *Physical Review B*, 83(195131), 2011.

[104] Jorge Kohanoff. *Electronic structure calculations for solids and molecules: theory and computational methods*. Cambridge University Press, 2006.

[105] VV Kohn and LJ Sham. Self-consistent equations including exchange and correlation effects. *PHYSICAL REVIEW*, 140(4A):1–5, 1965.

[106] Lingzhu Kong, Yves J Chabal, and David C Langreth. First-principles approach to rotational-vibrational frequencies and infrared intensity for h_ {2} adsorbed in nanoporous materials. *Physical Review B*, 83(12):121402, 2011.

[107] Lingzhu Kong, Valentino R. Cooper, Nour Nijem, Kunhao Li, Jing Li, Yves J. Chabal, and David C. Langreth. Theoretical and experimental analysis of h_2 binding in a prototypical metal-organic framework material". *Physical Review B*, 79(8), 2009.

[108] Lingzhu Kong, Guillermo Román-Pérez, José M. Soler, and David C. Langreth. Energetics and dynamics of h_2 adsorbed in a nanoporous material at low temperature. *Physical Review Letters*, 103(9), 2009.

[109] W Krätschmer, Lowell D Lamb, K Fostiropoulos, and Donald R Huffman. C60: a new form of carbon. *Nature*, 347(6291):354–358, 1990.

[110] G. Kresse and J. Furthmller. *Computational Materials Science*, 6(15), 1996.

[111] G. Kresse and J. Furthmuller. *Phys. Rev. B*, 54(11169), 1996.

[112] G. Kresse and J. Hafner. *Phys. Rev. B*, 47(558), 1993.

[113] G. Kresse and J. Hafner. *Phys. Rev. B*, 49(14251), 1994.

[114] G. Kresse and D. Joubert. *Phys. Rev. B*, 50(17953), 1999.

[115] R Krishna and JM Van Baten. Segregation effects in adsorption of co2-containing mixtures and their consequences for separation selectivities in cage-type zeolites. *Separation and Purification Technology*, 61(3):414–423, 2008.

[116] Rajamani Krishna and Jasper M van Baten. In silico screening of zeolite membranes for co2 capture. *Journal of Membrane Science*, 360(1):323–333, 2010.

[117] Rajamani Krishna and Jasper M van Baten. A comparison of the co2 capture characteristics of zeolites and metal–organic frameworks. *Separation and Purification Technology*, 87:120–126, 2012.

[118] Rep Kubo. The fluctuation-dissipation theorem. *Reports on Progress in Physics*, 29(1):255, 1966.

[119] M. KUMAR RANA, H. SEUNG KOH, J. HWANG, and D.J. SIEGEL. Comparing van der waals density functionals for co2 adsorption in metal organic frameworks. *Journal of physical chemistry. C*, 116(32):16957–16968, 2012.

[120] H Kümmel. Compound pair states in imperfect fermi gases. *Nuclear Physics*, 22(2):177–183, 1961.

[121] P. W. Langhoff and M. Karplus. Padé approximants for two and three body dipole dispersion interactions. *Journal of Chemical Physics*, 53(1), 1970.

[122] David C Langreth, Max Dion, Henrik Rydberg, Elsebeth Schröder, Per Hyldgaard, and Bengt I Lundqvist. Van der waals density functional theory with applications. *International journal of quantum chemistry*, 101(5):599–610, 2004.

[123] David C Langreth, Max Dion, Henrik Rydberg, Elsebeth Schröder, Per Hyldgaard, and Bengt I Lundqvist. Van der waals density functional theory with applications. *International journal of quantum chemistry*, 101(5):599–610, 2005.

[124] David C Langreth and John P Perdew. The exchange-correlation energy of a metallic surface. *Solid State Communications*, 17(11):1425–1429, 1975.

[125] David C Langreth and John P Perdew. Exchange-correlation energy of a metallic surface: Wave-vector analysis. *Physical Review B*, 15(6):2884, 1977.

[126] David C Langreth and SH Vosko. Response functions and nonlocal approximations. *Advances in quantum chemistry*, 21:175–199, 1990.

[127] DC Langreth, Bengt I Lundqvist, Svetla D Chakarova-Käck, VR Cooper, Max Dion, Per Hyldgaard, A Kelkkanen, Jesper Kleis, Lingzhu Kong, Shen Li, et al. A density functional for sparse matter. *Journal of Physics: Condensed Matter*, 21(8):084203, 2009.

[128] Kyuho Lee, Éamonn D Murray, Lingzhu Kong, Bengt I Lundqvist, and David C Langreth. Higher-accuracy van der waals density functional. *Physical Review B*, 82(8):081101, 2010.

[129] B. Li, S. Wei, and L. Chen. Molecular simulation of co2, n2 and ch4 adsorption and separation in zif-78 and zif-79. *Molecular Simulation*, 37(13):1131–1142, 2011.

[130] Bo Li, Shihao Wei, and Liang Chen. Molecular simulation of co2, n2 and ch4 adsorption and separation in zif-78 and zif-79. *Molecular Simulation*, 37(13):1131–1142, 2011.

[131] Hailian Li, Mohamed Eddaoudi, Michael O'Keeffe, and Omar M Yaghi. Design and synthesis of an exceptionally stable and highly porous metal-organic framework. *Nature*, 402(6759):276–279, 1999.

[132] J.R. Li, R.J. Kuppler, and H.C. Zhou. Selective gas adsorption and separation in metal–organic frameworks. *Chemical Society Reviews*, 38(5):1477–1504, 2009.

[133] Q. Li and T. Thonhauser. A theoretical study of the hydrogen-storage potential of (h2)4ch4 in metal organic framework materials and carbon nanotubes. *Journal of Physics: Condensed Matter*, 24:424204, 2012.

[134] Yanshuo Li, Fangyi Liang, Helge Bux, Weishen Yang, and Jürgen Caro. Zeolitic imidazolate framework zif-7 based molecular sieve membrane for hydrogen separation. *Journal of Membrane Science*, 354(1-2):48 – 54, 2010.

[135] DR Lide. Crc handbook of chemistry and physics, 2008.

[136] X. Lin, N. Champness, and M. Schröder. Hydrogen, methane and carbon dioxide adsorption in metal-organic framework materials. *Functional Metal-Organic Frameworks: Gas Storage, Separation and Catalysis*, pages 35–76, 2010.

[137] Bei Liu and Berend Smit. Molecular simulation studies of separation of co2/n2, co2/ch4, and ch4/n2 by zifs. *The Journal of Physical Chemistry C*, 114(18):8515–8522, 2010.

[138] Dahuan Liu, Chengcheng Zheng, Qingyuan Yang, and Chongli Zhong. Understanding the adsorption and diffusion of carbon dioxide in zeolitic imidazolate frameworks: A molecular simulation study. *The Journal of Physical Chemistry C*, 113(12):5004–5009, 2009.

[139] Jinchen Liu, Seda Keskin, David S. Sholl, and J. Karl Johnson. Molecular simulations and theoretical predictions for adsorption and diffusion of ch4/h2 and co2/ch4 mixtures in zifs. *The Journal of Physical Chemistry C*, 115(25):12560–12566, 2011.

[140] Wei Liu, Javier Carrasco, Biswajit Santra, Angelos Michaelides, Matthias Scheffler, and Alexandre Tkatchenko. Benzene adsorbed on metals: Concerted effect of covalency and van der waals bonding. *Physical Review B*, 86(24):245405, 2012.

[141] Yunyang Liu, Enping Hu, Easir A. Khan, and Zhiping Lai. Synthesis and characterization of zif-69 membranes and separation for co2/co mixture. *Journal of Membrane Science*, 353(12):36 – 40, 2010.

[142] Nina Lock, Yue Wu, Mogens Christensen, Lisa J Cameron, Vanessa K Peterson, Adam J Bridgeman, Cameron J Kepert, and Bo B Iversen. Elucidating negative thermal expansion in mof-5. *The Journal of Physical Chemistry C*, 114(39):16181–16186, 2010.

[143] Fritz London. Zur theorie und systematik der molekularkräfte. *Zeitschrift für Physik A Hadrons and Nuclei*, 63(3):245–279, 1930.

[144] HA Lorentz. Über die anwendung des satzes vom virial in der kinetischen theorie der gase. *Annalen der physik*, 248(1):127–136, 1881.

[145] BI Lundqvist. Characteristic structure in core electron spectra of metals due to the electron-plasmon coupling. *Zeitschrift für Physik B Condensed Matter*, 9(3):236–248, 1969.

[146] Otfried Madelung. *Introduction to solid-state theory*, volume 2. Springer, 1995.

[147] Richard M Martin. *Electronic structure: basic theory and practical methods*. Cambridge university press, 2004.

[148] J Maultzsch, R Pomraenke, S Reich, E Chang, D Prezzi, A Ruini, E Molinari, MS Strano, C Thomsen, and C Lienau. Exciton binding energies in carbon nanotubes from two-photon photoluminescence. *Physical Review B*, 72(24):241402, 2005.

[149] C. Mavroyannis and M.J. Stephen. Dispersion forces. *Molecular Physics*, 5(6):629–638, 1962.

[150] Jesse G McDaniel and JR Schmidt. Robust, transferable, and physically motivated force fields for gas adsorption in functionalized zeolitic imidazolate frameworks. *The Journal of Physical Chemistry C*, 116(26):14031–14039, 2012.

[151] Jesse G McDaniel, Kuang Yu, and JR Schmidt. Ab initio, physically motivated force fields for co2 adsorption in zeolitic imidazolate frameworks. *The Journal of Physical Chemistry C*, 116(2):1892–1903, 2012.

[152] M. Methfessel. High-precision sampling for brillouin-zone integration in metals. *Phys. Rev. B; Physical Review B*, 40(6):3616–3621, 1989.

[153] JW Mintmire, BI Dunlap, and CT White. Are fullerene tubules metallic? *Physical Review Letters*, 68(5):631–634, 1992.

[154] Chr Møller and Milton S Plesset. Note on an approximation treatment for many-electron systems. *Physical Review*, 46(7):618, 1934.

[155] William Morris, Ning He, Keith G Ray, Peter Klonowski, Hiroyasu Furukawa, Isaak N Daniels, Yao A Houndonougbo, Mark Asta, Omar M Yaghi, and Brian B Laird. A combined experimental-computational study on the effect of topology on carbon dioxide adsorption in zeolitic imidazolate frameworks. *The Journal of Physical Chemistry C*, 116(45):24084–24090, 2012.

[156] William Morris, Belinda Leung, Hiroyasu Furukawa, Omar K. Yaghi, Ning He, Hideki Hayashi, Yao Houndonougbo, Mark Asta, Brian B. Laird, and Omar M. Yaghi. A combined experimental-computational investigation of carbon dioxide capture in a series of isoreticular zeolitic imidazolate frameworks. *Journal of the American Chemical Society*, 132(32):11006–11008, 2010.

[157] B. Mu and K.S. Walton. Adsorption equilibrium of methane and carbon dioxide on porous metal-organic framework zn-btb. *Adsorption*, 17(5):777–782, 2011.

[158] W. Mu, D. Liu, Q. Yang, and C. Zhong. Computational study of the effect of organic linkers on natural gas upgrading in metal–organic frameworks. *Microporous and Mesoporous Materials*, 130(1):76–82, 2010.

[159] N. Nijem, P. Thissen, Y. Yao, R.C. Longo, K. Roodenko, H. Wu, Y. Zhao, K. Cho, J. Li, D.C. Langreth, et al. Understanding the preferential adsorption of co2 over n2 in a flexible metal–organic framework. *Journal of the American Chemical Society*, 133(32):12849–12857, 2011.

[160] N. Nijem, H. Wu, P. Canepa, A.M. Marti, K.J. Balkus, Jr, T. Thonhauser, J. Li, and Y.J. Chabal. Tuning the gate opening pressure of metal organic frameworks (mofs) for the selective separation of hydrocarbons. *Journal of the American Chemical Society*, 2012.

[161] KS Novoselov, Ak K Geim, SV Morozov, D Jiang, MI Katsnelson IV Grigorieva, SV Dubonos, and AA Firsov. Two-dimensional gas of massless dirac fermions in graphene. *nature*, 438(7065):197–200, 2005.

[162] JF Ogilvie and Frank YH Wang. Potential-energy functions of diatomic molecules of the noble gases i. like nuclear species. *Journal of molecular structure*, 273:277–290, 1992.

[163] Taisuke Ohta, Aaron Bostwick, Thomas Seyller, Karsten Horn, and Eli Rotenberg. Controlling the electronic structure of bilayer graphene. *Science*, 313(5789):951–954, 2006.

[164] David Olmsted, Keith G. Ray, Yao Houndonougbo, Brain B. Laird, and Mark Asta. Unpublished simulations of gas diffusion in zifs. 2013.

[165] J Paldus, J Čížek, and I Shavitt. Correlation problems in atomic and molecular systems. iv. extended coupled-pair many-electron theory and its application to the bh_ {3} molecule. *Physical Review A*, 5(1):50, 1972.

[166] Kyo Sung Park, Zheng Ni, Adrien P. Côté, Jae Yong Choi, Rudan Huang, Fernando J. Uribe-Romo, Hee K. Chae, Michael O'Keeffe, and Omar M. Yaghi. Exceptional chemical and thermal stability of zeolitic imidazolate frameworks. *Proceedings of the National Academy of Sciences*, 103(27):10186–10191, 2006.

[167] Kyo Sung Park, Zheng Ni, Adrien P Côté, Jae Yong Choi, Rudan Huang, Fernando J Uribe-Romo, Hee K Chae, Michael OKeeffe, and Omar M Yaghi. Exceptional chemical and thermal stability of zeolitic imidazolate frameworks. *Proceedings of the National Academy of Sciences*, 103(27):10186–10191, 2006.

[168] John Perdew and Wang Yue. Accurate and simple density functional for the electronic exchange energy: Generalized gradient approximation. *Physical Review B*, 33(12):8800–8802, 1986.

[169] John P Perdew and Kieron Burke. Comparison shopping for a gradient-corrected density functional. *International journal of quantum chemistry*, 57(3):309–319, 1996.

[170] John P. Perdew, Kieron Burke, and Matthias Ernzerhof. Generalized gradient approximation made simple. *Physical Review Letters*, 77(18):3865–3868, 1996.

[171] Vasili Perebeinos, J Tersoff, and Phaedon Avouris. Scaling of excitons in carbon nanotubes. *Physical review letters*, 92(25):257402, 2004.

[172] Javier Pérez-Pellitero, Hedi Amrouche, Florâ...R. Siperstein, Gerhard Pirngruber, Carlos Nieto-Draghi, Gérald Chaplais, Angélique Simon-Masseron, Delphine Bazer-Bachi, David Peralta, and Nicolas Bats. Adsorption of co2, ch4, and n2 on zeolitic imidazolate frameworks: Experiments and simulations. *Chemistry – A European Journal*, 16(5):1560–1571, 2010.

[173] A. Phan, C.J. Doonan, F.J. Uribe-Romo, C.B. Knobler, M. Okeeffe, and O.M. Yaghi. Synthesis, structure, and carbon dioxide capture properties of zeolitic imidazolate frameworks. *Acc. Chem. Res*, 43(1):58–67, 2010.

[174] Anh Phan, Christian J. Doonan, Fernando J. Uribe-Romo, Carolyn B. Knobler, Michael O'Keeffe, and Omar M. Yaghi. Synthesis, structure, and carbon dioxide capture properties of zeolitic imidazolate frameworks. *Accounts of Chemical Research*, 43(1):58–67, 2010.

[175] K Pi, KM McCreary, W Bao, Wei Han, YF Chiang, Yan Li, S-W Tsai, CN Lau, and RK Kawakami. Electronic doping and scattering by transition metals on graphene. *Physical Review B*, 80(7):075406, 2009.

[176] A. Pianwanit, C. Kritayakornupong, A. Vongachariya, N. Selphusit, T. Ploymeerusmee, T. Remsungnen, D. Nuntasri, S. Fritzsche, and S. Hannongbua. The optimal binding sites of ch4 and co2 molecules on the metal-organic framework mof-5: Oniom calculations. *Chemical Physics*, 349(1):77–82, 2008.

[177] S. Plimpton. *Fast Parallel Algorithms for Short-Range Molecular Dynamics, J Comp Phys, 117, 1-19 (1995) http://lammps.sandia.gov.*

[178] S. J. Plimpton, R. Pollock, and M. Stevens. In *Particle-Mesh Ewald and rRESPA for Parallel Molecular Dynamics Simulations in Proc of the Eighth SIAM Conference on Parallel Processing for Scientific Computing, Minneapolis, MN*, March 1997.

[179] R. Poloni, B. Smit, and J.B. Neaton. Co2 capture by metal–organic frameworks with van der waals density functionals. *The Journal of Physical Chemistry A*, 116(20):4957–4964, 2012.

[180] R. Poloni, B. Smit, and J.B. Neaton. Ligand-assisted enhancement of co2 capture in metal–organic frameworks. *Journal of the American Chemical Society*, 134(15):6714–6719, 2012.

[181] George D Purvis III and Rodney J Bartlett. A full coupled-cluster singles and doubles model: The inclusion of disconnected triples. *The Journal of Chemical Physics*, 76:1910, 1982.

[182] CJ Radke and JM Prausnitz. Thermodynamics of multi-solute adsorption from dilute liquid solutions. *AIChE Journal*, 18(4):761–768, 1972.

[183] Rees B. Rankin, Jinchen Liu, Anant D. Kulkarni, and J. Karl Johnson. Adsorption and diffusion of light gases in zif-68 and zif-70: A simulation study. *The Journal of Physical Chemistry C*, 113(39):16906–16914, 2009.

[184] Anthony K Rappe, Carla J Casewit, KS Colwell, WA Goddard Iii, and WM Skiff. Uff, a full periodic table force field for molecular mechanics and molecular dynamics simulations. *Journal of the American Chemical Society*, 114(25):10024–10035, 1992.

[185] Keith G. Ray, David Olmsted, Ning He, Yao Houndonougbo, Brian B. Laird, and Mark Asta. van der waals density functional study of co_2 binding in zeolitic imidazolate frameworks. *Phys. Rev. B*, 85:085410, Feb 2012.

[186] Keith G. Ray, David Olmsted, Yao Houndonougbo, Brain B. Laird, and Mark Asta. Origins of ch4/co2 adsorption selectivity in zeolitic imidazolate frameworks: A van der waals density functional study. *Submitted to J. Phys. Chem. C*, 2013.

[187] T.E. Reich, S. Behera, K.T. Jackson, P. Jena, and H.M. El-Kaderi. Highly selective co2/ch4 gas uptake by a halogen-decorated borazine-linked polymer. *J. Mater. Chem.*, 2012.

[188] Guillermo Román-Pérez and José M. Soler. Efficient implementation of a van der waals density functional: Application to double-wall carbon nanotubes. *Physical Review Letters*, 103(096102), 2009.

[189] N.L. Rosi, J. Eckert, M. Eddaoudi, D.T. Vodak, J. Kim, M. O'Keeffe, and O.M. Yaghi. Hydrogen storage in microporous metal-organic frameworks. *Science*, 300(5622):1127–1129, 2003.

[190] J.L.C. Rowsell and O.M. Yaghi. Metal–organic frameworks: a new class of porous materials. *Microporous and Mesoporous Materials*, 73(1):3–14, 2004.

[191] J.L.C. Rowsell and O.M. Yaghi. Effects of functionalization, catenation, and variation of the metal oxide and organic linking units on the low-pressure hydrogen adsorption properties of metal-organic frameworks. *Journal of the American Chemical Society*, 128(4):1304–1315, 2006.

[192] Victor G Ruiz, Wei Liu, Egbert Zojer, Matthias Scheffler, and Alexandre Tkatchenko. Density-functional theory with screened van der waals interactions for the modeling of hybrid inorganic-organic systems. *Physical Review Letters*, 108(14):146103, 2012.

[193] Erich Runge and Eberhard KU Gross. Density-functional theory for time-dependent systems. *Physical Review Letters*, 52(12):997–1000, 1984.

[194] Henrik Rydberg, Max Dion, Niclas Jacobson, Elsebeth Schröder, Per Hyldgaard, SI Simak, David C Langreth, and Bengt I Lundqvist. Van der waals density functional for layered structures. *Physical review letters*, 91(12):126402, 2003.

[195] Henrik Rydberg, Bengt I Lundqvist, David C Langreth, and Maxime Dion. Tractable nonlocal correlation density functionals for flat surfaces and slabs. *Physical Review B*, 62(11):6997, 2000.

[196] T. Sagara, J. Klassen, J. Ortony, and E. Ganz. Binding energies of hydrogen molecules to isoreticular metal-organic framework materials. *The Journal of chemical physics*, 123:014701, 2005.

[197] E. Sanville, S.D. Kenny, R. Smith, and G. Henkelman. Improved grid-based algorithm for bader charge allocation. *Journal of computational chemistry*, 28(5):899–908, 2007.

[198] Norbert Schuch and Frank Verstraete. Computational complexity of interacting electrons and fundamental limitations of density functional theory. *Nature Physics*, 5(10):732–735, 2009.

[199] P. Serra-Crespo, E.V. Ramos-Fernandez, J. Gascon, and F. Kapteijn. Synthesis and characterization of an amino functionalized mil-101 (al): Separation and catalytic properties. *Chemistry of Materials*, 23(10):2565–2572, 2011.

[200] Andrew Sirjoosingh, Saman Alavi, and Tom K. Woo. Grand-canonical monte carlo and molecular-dynamics simulations of carbon-dioxide and carbon-monoxide adsorption in zeolitic imidazolate framework materials. *The Journal of Physical Chemistry C*, 114(5):2171–2178, 2010.

[201] Randall Q Snurr, Alexis T Bell, and Doros N Theodorou. Prediction of adsorption of aromatic hydrocarbons in silicalite from grand canonical monte carlo simulations with biased insertions. *The Journal of Physical Chemistry*, 97(51):13742–13752, 1993.

[202] Catalin D. Spataru, Sohrab Ismail-Beigi, Lorin X. Benedict, and Steven G. Louie. Excitonic effects and optical spectra of single-walled carbon nanotubes. *Phys. Rev. Lett.*, 92:077402, Feb 2004.

[203] John M Stubbs, Jeffrey J Potoff, and J Ilja Siepmann. Transferable potentials for phase equilibria. 6. united-atom description for ethers, glycols, ketones, and aldehydes. *The Journal of Physical Chemistry B*, 108(45):17596–17605, 2004.

[204] Marco Tagliabue, Caterina Rizzo, Nicola B. Onorati, Enrico F. Gambarotta, Angela Carati, and Francesca Bazzano. Regenerability of zeolites as adsorbents for natural gas sweetening: A case-study. *Fuel*, 93(0):238 – 244, 2012.

[205] Tait Takatani, Edward G Hohenstein, Massimo Malagoli, Michael S Marshall, and C David Sherrill. Basis set consistent revision of the s22 test set of noncovalent interaction energies. *The Journal of chemical physics*, 132:144104, 2010.

[206] W. Tang, E. Sanville, and G. Henkelman. A grid-based bader analysis algorithm without lattice bias. *Journal of Physics: Condensed Matter*, 21(8):084204, 2009.

[207] Timo Thonhauser, Valentino R Cooper, Shen Li, Aaron Puzder, Per Hyldgaard, and David C Langreth. Van der waals density functional: Self-consistent potential and the nature of the van der waals bond. *Physical Review B*, 76(12):125112, 2007.

[208] A.W. Thornton, D. Dubbeldam, M.S. Liu, B.P. Ladewig, A. Hill, and M.R. Hill. Feasibility of zeolitic imidazolate framework membranes for clean energy applications. *Energy Environ. Sci.*, 2012.

[209] A. Tkatchenko and M. Scheffler. Accurate molecular van der waals interactions from ground-state electron density and free-atom reference data. *Physical review letters*, 102(7):73005, 2009.

[210] Alexandre Tkatchenko, Robert A DiStasio Jr, Roberto Car, and Matthias Scheffler. Accurate and efficient method for many-body van der waals interactions. *Physical Review Letters*, 108(23):236402, 2012.

[211] MMJ Treacy, TW Ebbesen, and JM Gibson. Exceptionally high young's modulus observed for individual carbon nanotubes. 1996.

[212] Johannes Diderik Van der Waals and Johannes Diderik van der Waals. *Over de Continuiteit van den Gas-en Vloeistoftoestand*. AW Sijthoff, 1873.

[213] David Vanderbilt. Soft self-consistent pseudopotentials in a generalized eigenvalue formalism. *Physical Review B*, 41(11):7892, 1990.

[214] Surendar R. Venna and Moises A. Carreon. Highly permeable zeolite imidazolate framework-8 membranes for co2/ch4 separation. *Journal of the American Chemical Society*, 132(1):76–78, 2010. PMID: 20014839.

[215] Gianfranco Vidali, G Ihm, Hye-Young Kim, and Milton W Cole. Potentials of physical adsorption. *Surface Science Reports*, 12(4):135–181, 1991.

[216] Jearl Walker. The flying circus of physics with answers. 1977.

[217] Bo Wang, Adrien P Côté, Hiroyasu Furukawa, Michael OKeeffe, and Omar M Yaghi. Colossal cages in zeolitic imidazolate frameworks as selective carbon dioxide reservoirs. *Nature*, 453(7192):207–211, 2008.

[218] Feng Wang, Gordana Dukovic, Louis E Brus, and Tony F Heinz. The optical resonances in carbon nanotubes arise from excitons. *Science*, 308(5723):838–841, 2005.

[219] T. Watanabe, S. Keskin, S. Nair, and D.S. Sholl. Computational identification of a metal organic framework for high selectivity membrane-based co2/ch4 separations: Cu (hfipbb)(h2hfipbb) 0.5. *Physical Chemistry Chemical Physics*, 11(48):11389–11394, 2009.

[220] Conan Weeks, Jun Hu, Jason Alicea, Marcel Franz, and Ruqian Wu. Engineering a robust quantum spin hall state in graphene via adatom deposition. *Physical Review X*, 1(2):021001, 2011.

[221] Hui Wu, Jason M Simmons, Gadipelli Srinivas, Wei Zhou, and Taner Yildirim. Adsorption sites and binding nature of co2 in prototypical metal- organic frameworks: A combined neutron diffraction and first-principles study. *The Journal of Physical Chemistry Letters*, 1(13):1946–1951, 2010.

[222] Hui Wu, Wei Zhou, and Taner Yildirim. Hydrogen storage in a prototypical zeolitic imidazolate framework-8. *Journal of the American Chemical Society*, 129(17):5314–5315, 2007.

[223] Hui Wu, Wei Zhou, and Taner Yildirim. Hydrogen storage in a prototypical zeolitic imidazolate framework-8. *Journal of the American Chemical Society*, 129(17):5314–5315, 2007. PMID: 17425313.

[224] Hui Wu, Wei Zhou, and Taner Yildirim. High-capacity methane storage in metal-organic frameworks m2 (dhtp): The important role of open metal sites. *Journal of the American Chemical Society*, 131(13):4995–5000, 2009.

[225] Hui Wu, Wei Zhou, and Taner Yildirim. Methane sorption in nanoporous metalâ'organic frameworks and first-order phase transition of confined methane. *The Journal of Physical Chemistry C*, 113(7):3029–3035, 2009.

[226] Q. Yang, A.D. Wiersum, P.L. Llewellyn, V. Guillerm, C. Serre, and G. Maurin. Functionalizing porous zirconium terephthalate uio-66 (zr) for natural gas upgrading: a computational exploration. *Chemical Communications*, 47(34):9603–9605, 2011.

[227] Q. Yang and C. Zhong. Electrostatic-field-induced enhancement of gas mixture separation in metal-organic frameworks: A computational study. *ChemPhysChem*, 7(7):1417–1421, 2006.

[228] Q. Yang and C. Zhong. Molecular simulation of carbon dioxide/methane/hydrogen mixture adsorption in metal-organic frameworks. *The Journal of Physical Chemistry B*, 110(36):17776–17783, 2006.

[229] Kuang Yu, Jesse G McDaniel, and JR Schmidt. Physically motivated, robust, ab initio force fields for co2 and n2. *The Journal of Physical Chemistry B*, 115(33):10054–10063, 2011.

[230] B. Yuan, D. Ma, X. Wang, Z. Li, Y. Li, H. Liu, and D. He. A microporous, moisture-stable, and amine-functionalized metal–organic framework for highly selective separation of co2 from ch4. *Chemical Communications*, 48(8):1135–1137, 2012.

[231] Renju Zacharia, Hendrik Ulbricht, and Tobias Hertel. Interlayer cohesive energy of graphite from thermal desorption of polyaromatic hydrocarbons. *Physical Review B*, 69(15):155406, 2004.

[232] Yingkai Zhang and Weitao Yang. Comment on "generalized gradient approximation made simple"". *Physical Review Letters*, 80(4):890–890, 1998.

[233] Yuanbo Zhang, Yan-Wen Tan, Horst L Stormer, and Philip Kim. Experimental observation of the quantum hall effect and berry's phase in graphene. *Nature*, 438(7065):201–204, 2005.

[234] Min Zhou, Qi Wang, Li Zhang, Ying-Chun Liu, and Yu Kang. Adsorption sites of hydrogen in zeolitic imidazolate frameworks. *The Journal of Physical Chemistry B*, 113(32):11049–11053, 2009. PMID: 19624113.

[235] W Zhou, H Wu, T Yildirim, JR Simpson, and AR Hight Walker. Origin of the exceptional negative thermal expansion in metal-organic framework-5 zn4o (1, 4-benzenedicarboxylate)3. *Physical Review B*, 78(5):054114, 2008.

[236] John M Ziman. *Principles of the Theory of Solids*. Cambridge University Press, 1979.